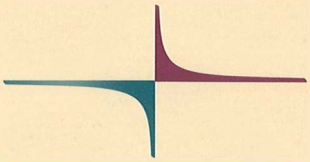

CSC Research Reports R03/96

Mathematical Modeling and Numerical Simulation of Czochralski Silicon Crystal Growth

Jari Järvinen

Center for Scientific Computing

Mathematical Modeling and Numerical Simulation of Czochralski Silicon Crystal Growth

Jari Järvinen

To be presented, with the permission of the Faculty of Mathematics and Natural Sciences of the University of Jyväskylä, for public criticism in Auditorium S 212 of the University, on July 6th, 1996, at 12 o'clock noon.

Verkkoversio julkaistu tekijän ja
CSC – Tieteen tietotekniikan keskus Oy:n luvalla

URN:ISBN:978-952-86-0378-8
ISBN 978-952-86-0378-8 (PDF)

Jyväskylän yliopisto, 2024

ISSN 0787–7498
ISBN 952–9821–27-1
Yliopistopaino 1996

Acknowledgements

At this occasion I would like to thank Professor Risto Nieminen from the Center for Scientific Computing for introducing me to this field and his continuous encouragement during our collaboration.

I am deeply indebted to my teacher, Docent Timo Tiihonen from the University of Jyväskylä, for his invaluable advice during my work.

I wish to thank Doctor Ivan Götz from the Technical University of Munich and Doctor Peter Hansbo from Chalmers Technical University for their careful reading of the manuscript and for their comments and criticism.

I am much obliged to Professor Karl-Heinz Hoffmann from the Technical University of Munich for pleasant collaboration and for opportunity to spend one year in his research group.

I would also like to express my thanks to Olli Anttila, Markku Tilli and Asko Vehanen from Okmetic Ltd. for their collaboration and for many invaluable discussions.

My thanks are due to all my former colleagues in the University of Jyväskylä, especially Kai Hiltunen and Jari Hämäläinen, and Wolfgang Seifert from the Technical University of Munich for various fruitful discussions. Furthermore, I would like to thank all my colleagues at the Center for Scientific Computing, particularly Matti Gröhn and Ville Savolainen for helping me in many occasions.

For the financial support I would like to acknowledge the Technology Development Center of Finland, the Foundation of Outokumpu and the Foundation of Leo and Regina Wainstein.

To my mother and father, and my parents-in-law, Marja-Liisa and Seppo, I am much obliged for their continuous support during my work.

Finally, I wish to express my most sincere feelings of gratitude to my wife, Inari, for her continuous understanding and irreplaceable support during my work. My last, but not the slightest thanks I would like to reserve to my little son, Juho, for waking me up early enough in the mornings and pushing me to work.

Espoo, June 1996 Jari Järvinen

Contents

1. Introduction

Pocket calculators, computers, traffic lights and modern cars are good examples where we can come across products of modern electronics industry in the present-day life. Basic products such as integrated circuits are often so well concealed into the hearts of devices that we do not realize them or we treat them as a matter of course. However, there is a good reason to say that integrated circuits are the brain and the heart of today's electronics and they have a tremendous influence on our daily customs.

Worldwide the electronics industry is the largest and fastest growing manufacturing industry. In 1993 the worldwide investments of the electronics industry were estimated to be in the range of $ 900 billion. The basis of the electronics industry is semiconductor processing whose investments alone were in the range of $ 60-70 billion, [Müller93].

The semiconductor industry can roughly be divided into two sections: a refining section which uses basic material, semiconductor wafers, to produce integrated circuits and a manufacturing section which produces semiconductor wafers, Figure 1.1.

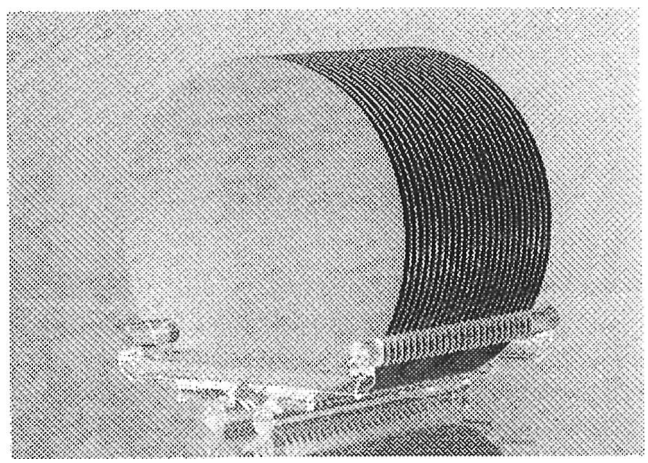

Figure 1.1 Semiconductor wafers

In the manufacturing section semiconductor wafers are produced from single crystals. Single crystals are grown from molten purified semiconductor materials and the result of crystal growth process has the form of a cylindrical crystal rod with

the diameter of a few inches. Solid crystals are afterwards cut to form thin semiconductor wafers. Nowadays the Czochralski method, the float-zone pulling method and the Bridgman method are the most frequently used techniques to grow single crystals. The materials of crystals are mainly silicon, gallium-arsenide and germanium.

The diameters of single silicon crystals produced industrially by the Czochralski method are typically in the range of 4-8 inches, Figure 1.2. The trend towards larger diameters is evident in the future, and some experiments have already been carried out with crystals whose diameters are even 12 inches. The growth of larger diameter crystals requires the up-scaling of existing equipment which together with products of new technology, e.g., the continuous Czochralski crystal growth (CCz) and the magnetic Czochralski crystal growth (MCz), set new challenges for scientists and engineers in the crystal growth field.

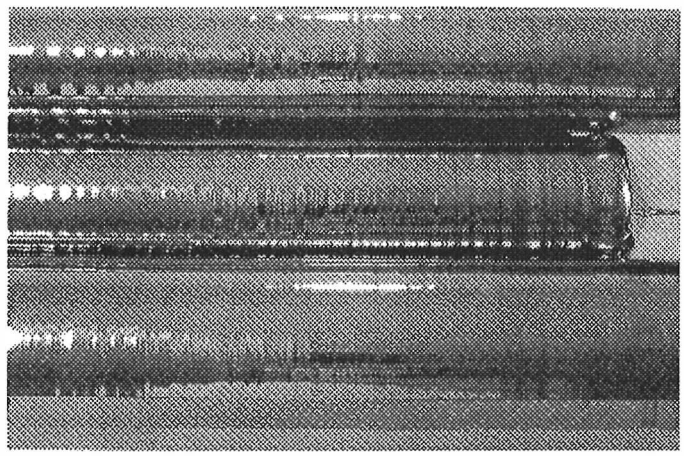

Figure 1.2 Silicon crystals

So far the development of the semiconductor technology has been mainly empirical. With rising industrial and economical importance and with new challenges in product development scientists are now providing knowledge required in this field. Several research projects, for instance in the field of applied mathematics, physics and chemistry, have already been carried out and the amount of research is undoubtedly going to grow in the future.

Our research is connected to mathematical modeling and numerical simulation of the Czochralski crystal growth, i.e., we restrict our research to concern the manufacturing section. Our special interests lie in the development of mathematical models and numerical simulation tools for the Czochralski silicon crystal growth.

The Czochralski crystal growth technique requires high temperature environment and fairly complicated growing furnaces (Chapter 2.1, Czochralski Crystal Growth Technique). Experimental measurements, such as the measurements of the temperature and velocity field of the melt, offer invaluable information from physical mechanisms. They are, however, very laborious to make and require possibly construction of complicated experimental systems ([Kinney93], [Watanabe93]) necessitating considerable economical investments.

At the same time modern supercomputers have evolved to the point where very large and complex numerical simulations can be carried out in a sufficiently short time frame. In this situation the development of mathematical models and numerical simulation tools can effectively support the Czochralski crystal growth process. The numerically solved mathematical models have the advantage of providing new insight into physical phenomena. They allow an easy way to study, for instance, new geometries of the Czochralski furnace or growth parameters.

In Chapter 2.2 we make a short survey of the field of mathematical modeling and numerical simulation of the Czochralski crystal growth and summarize the recent works made by some leading laboratories (Fundamental Research Laboratories by NEC/Université Catholique de Louvain, Massachusetts Institute of Technology and University of Erlangen-Nürnberg) in this field. The research made in these laboratories has been carried out in the conventional Czochralski system with small geometrical modifications. The main stress has been on the modeling of the entire Czochralski process in the axisymmetric geometry, [Kakimoto91], [Kinney93a], [Kinney93b] and [Müller93], even if steps towards three-dimensional melt flow simulations have been taken (see Chapter 2.2). Although in the references listed above the conventional Czochralski system is treated, there is, however, a difference between these works and ours arising from the different computational geometries. In these works the diameters of crystals and crucibles are in the range of 2.32-8.25 cm and 7.2-25.4 cm, respectively, while in this work we try to simulate crystal growth with the diameters 12.7 cm for crystals and 40.0 cm for crucibles. The diameters of industrially produced single silicon crystals are typically more than 10.2 cm (4 inches) grown from crucibles with diameters exceeding 35.6 cm (14 inches).

It is also noteworthy that the works discussed in [Kakimoto91], [Kinney93a], [Kinney93b] and [Müller93] are based on either steady-state or quasi steady-state assumptions for the equations of melt flow and temperature in the whole Czochralski geometry. The steady-state or the quasi steady-state assumptions for melt flow are however not valid, since in reality melt flow is strongly time dependent. We stress that the key for the successful numerical simulation of the whole Czochralski crystal growth is the correct description of melt flow which should be done with a time dependent analysis. We demonstrate the time dependent character of melt flow in numerous numerical examples in the course of this work.

The melt flow, the temperature distribution in the whole Czochralski process, and

the free boundary position between the crystal and the melt are the quantities which we are most interested in. These quantities are governed by the time dependent and coupled heat and Navier-Stokes equations with appropriate boundary conditions.

Due to complexity of the Czochralski crystal growth it is reasonable to divide the problem into subproblems from the point of view of mathematical modeling and numerical simulation. First, the modeling of the pure melt flow demands the coupling of the heat and Navier-Stokes equations. On the other hand, if we consider the crystal-melt system, we have to handle the coupled heat and Navier-Stokes equations in the varying geometry so that the free boundaries are considered as a part of the solution. The modeling of the whole Czochralski crystal growth itself requires in addition the presence of all other geometrical objects and the description of global heat transfer. A significant part of heat is transferred by radiation between various surfaces in the Czochralski configuration. This mechanism can be described by the diffuse-gray radiation, if we assume a diffuse and gray behavior from all surfaces, i.e., there are for instance no transparent or mirror surfaces. We analyze the mathematical modeling of the subproblems and the whole Czochralski crystal growth individually in Chapter 3. Numerical simulations of the mathematical models are carried out by the finite element method (FEM) in Chapters 4, 5 and 6.

The formulation of the diffuse-gray radiation presented in this work differs from previously published crystal growth articles on which radiative heat transfer is considered. Instead of treating a radiative surface as a finite union of simple surface elements ([Atherton87], [Rama85]) we introduce a non-local boundary condition on the radiating part of the surface (Chapter 3.3).

If we then take a closer look at the free boundary problem in the crystal-melt system, there are in fact three different kinds of free boundaries. Namely, the free boundaries between crystal and melt, crystal and gas and melt and gas. In this work only the crystal-melt interface is considered as a free boundary. The radius of the crystal is assumed to be constant and the shape of the melt-gas interface is based on the analytical representation of the shape of the meniscus presented by Hurle, [Hurle83].

In the mathematical modeling of the free boundary problem we shall consider enthalpy as a primary unknown instead of temperature. This leads to a use of the enthalpy method which offers a way to treat the free boundary problem in a two phase system ([Dalhuijsen86], [Elliot82], [White82]). It is, however, non-trivial to apply the method in such systems where more than two different materials appear. A standard definition of enthalpy leads to a case where enthalpy is discontinuous at the melt-silica crucible interface. In order to guarantee the continuity of enthalpy at this interface some modifications in the definition of enthalpy are required (see Chapter 3.3).

The enthalpy method is a typical fixed grid method. The use of this method offers

a significant benefit especially in the entire Czochralski geometry. The application of the diffuse-gray radiation demands the calculation of view factors which are dependent on the geometry. Since our finite element mesh remains unchanged, the view factors have to be calculated only once, at the beginning of simulations. Since we assume the axisymmetry of the geometry, the view factors have not to be computed in three dimensions as presented in [Kinney93a] and [Kinney93b] (see the references therein). The expressions of the view factors contain two area integrals which can be simplified into line integrals by using the axisymmetry assumption (Chapter 6.3).

As mentioned above, the finite element method is used to solve the described mathematical models since it has proved its capability to handle complex geometries and problems in many circumstances (for problems in fluid dynamics and structural mechanics see [Cecchi95], [Gunzburger93] and [Zienkiewicz89] and in crystal growth [Atherton87], [Cuvelier87], [Derby87], [Hilpert91], [Kakimoto91], [Kinney93] and [Sackinger89]). Since the melt flow in the connection with the Czochralski crystal growth is highly convection dominated, the streamline upwinding/Petrov-Galerkin finite element method is applied.

Basic tools of the finite element method (variational formulations and finite element discretizations) are presented in Chapter 4 for thermally coupled liquid flows. Furthermore, the linearization techniques for nonlinear and coupled problems are discussed. From the finite element methodology point of view this chapter acts as a preliminary one to the chapters later on. The other function of Chapter 4 is to compare the results from the numerical simulations to the examples found in the literature and to examine the silicon melt flow with various system parameters. The numerical simulations for the crystal-melt system and the entire Czochralski crystal growth are presented in Chapter 5 and Chapter 6.

The numerical results presented in this work have been carried out on Convex C3840 at the Center for Scientific Computing (CSC) in Finland. All numerical results have been visualized by a visualizing program called Funcs developed at CSC by Juha Ruokolainen.

2. Czochralski Crystal Growth

2.1 Czochralski Crystal Growth Technique

The Czochralski method, the float-zone pulling method and the Bridgman method are the most important techniques to grow single crystals. More than 90% of all semiconductor crystals are produced by the Czochralski method and the rest mainly by the float-zone pulling method. The Bridgman method is used only for the production of crystals with a small diameter.

The principle of the Czochralski method dates back to the work of J. Czochralski, who established it in 1917 to determine the crystallization velocity of metals. During the fifties, the first semiconductor crystals, first germanium and then silicon crystals, were grown by the Czochralski method, [Müller93]. Since then the method has attained new innovative variations, for instance the liquid encapsulated technique (LEC), the continuous Czochralski crystal growth (CCz) and the magnetic Czochralski crystal growth (MCz).

The principle of the pulling of the single silicon crystal from the silicon melt by the conventional Czochralski method is depicted in Figures 2.1-2.4, [Sackinger89], [Zulehner82]. The Czochralski configuration is shown semantically in a three dimensional case in Figure 2.1 while in Figures 2.2-2.4 the cross sections of the Czochralski configuration are presented. In Figure 2.2 the initial state of the pulling process is presented. In Figures 2.3 and 2.4 the process is in the advanced and final state, respectively.

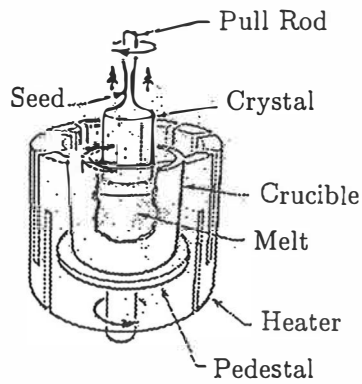

Figure 2.1 Three dimensional Czochralski crystal growth

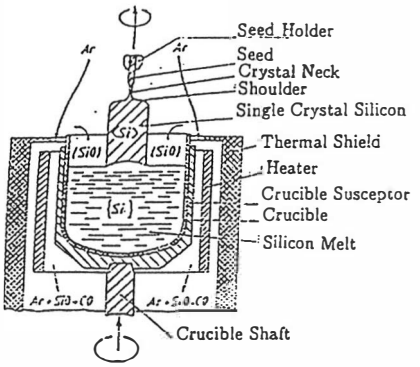

Figure 2.2 Initial state of pulling process

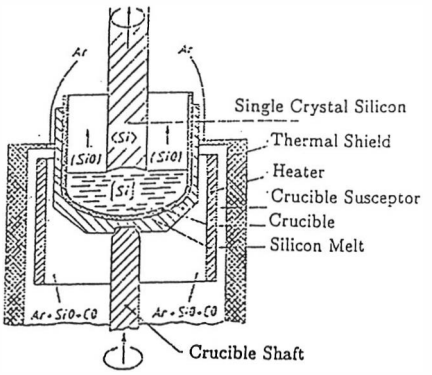

Figure 2.3 Advanced state of pulling process

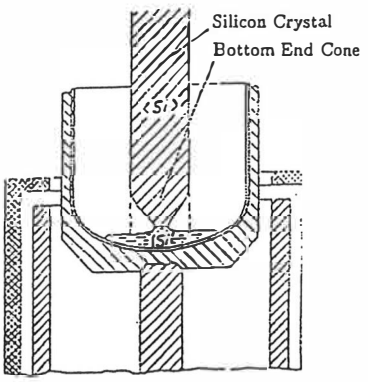

Figure 2.4 Final state of pulling process

The main components of the furnace are shown in Figure 2.2. A seed holder supports the crystal which consists of a seed, a crystal neck, a crystal shoulder and a single crystal silicon rod. The single crystal silicon rod is withdrawn vertically from the silicon melt which is inside of the silica (SiO_2) crucible. The surrounding parts of the silica crucible are a graphite susceptor, a crucible pedestal, a graphite resistance heater and thermal shields. The silica crucible is kept in the stabilizing susceptor rotating axially (counter to the crystal rotation) to provide axisymmetric heating conditions.

In the beginning of the process the seed crystal is dipped into the melt until it begins to melt itself. The melt should not, however, be so hot that the seed melts too much loosing its contact to the melt. The seed is then withdrawn from the silicon melt so that it begins to grow but there is no increase in its diameter.

It is very important for present-day applications that single silicon crystals are dislocation-free [Zulehner82]. For this reason the so called Dash technique is applied for the crystal pulling: The crystal diameter is gradually reduced to about 3-4 mm and the growth velocity is raised. With a suitable combination of these two factors the silicon crystal becomes dislocation-free after a few centimeters. After receiving the dislocation-free state the diameter of the crystal can be enlarged by reducing the pulling velocity and controlling the heating conditions (down cooling) until the diameter of the crystal reaches the desired value.

Shortly before the desired value of the diameter is reached the pulling velocity is raised to the specific value at which the silicon crystal grows with the required diameter. In general the pulling velocity is not kept constant but is reduced towards the bottom of the silicon crystal. This is mainly caused by increasing heat radiation from the crucible walls as the melt level sinks.

To avoid dislocations at the bottom of the silicon crystal the crystal diameter has to be reduced gradually to a small size. While the pulling velocity is increased the diameter of the silicon crystal decreases and an end-cone begins to develop, Figure 2.4. If the diameter is small enough and the main body of the grown crystal is long enough, the dislocation-free silicon crystal can be separated from the rest of the silicon melt.

During the Czochralski process the silica crucible is eroded by the hot silicon melt and oxygen dissolves to the melt. Oxygen is transported in the silicon melt by the convection processes. Most of oxygen evaporates through the melt-gas interface and therefore the inert gas (argon) has to flow continuously downwards through the pulling chamber to remove these byproducts. However, a certain amount of oxygen drifts in the silicon melt to the crystal growth interface and incorporates to the silicon crystal. Oxygen has both beneficial and harmful effects on the quality of the silicon crystal. A certain amount of oxygen is required in the crystal since oxygen hardens the silicon lattice giving silicon wafers the desired mechanical strength. On the other hand, if too much oxygen incorporates to the crystal, oxygen precipitates during the cooling and produces crystallographic defects, such

as dislocations and stacking faults, [Zulehner82].

2.2 Modeling and Numerical Simulating Aspects

The complexity of the Czochralski crystal growth process, as can be perceived from the previous chapter, poses a demanding task for the modeling. The governing physical mechanisms can, in principle, be described mathematically. A global model including both macroscopic and microscopic aspects is proposed in [Müller93]:

Macroscopic model:

- Heat transport by conduction and radiation within the Czochralski furnace and by conduction and convection within the crystal and the melt. Convection in the melt can be composed of the Grashof, Marangoni and forced convections. The Grashof (or natural) convection originates in temperature dependence of the density and Marangoni convection in temperature dependence of the surface tension. The forced convection is caused by the rotations of the crystal and crucible.
- Turbulence.
- Mass transport (oxygen, impurities) in the melt and gas.
- Free boundaries between crystal and melt, crystal and gas and melt and gas, respectively.
- Thermal stresses in the crystal.

Microscopic model:

- Dislocations.
- Precipitates.

Some of the research published in the literature concentrate on a certain part of the global model, for instance on heat transport by conduction and radiation within the whole Czochralski furnace [Atherton87] and [Rama85] or on three dimensional melt flow by neglecting the surrounding parts [Mihelčić84], [Yi94] and [Yi95]. There are, however, some works in which steps towards the global model have already been taken, [Müller93], [Kakimoto91], [Kinney93a] and [Kinney93b]. In the following we collect the basic results of these works and introduce shortly the methods used. Furthermore, we outline the basic differences between the present work and the works listed above.

Müller states two questions: whether convection in the melt is important for the growth and whether there are cases of interest in which the computation has to be carried out in three dimensions. He makes steady state numerical simulations in the whole Czochralski (LEC) configuration and compares the numerical results to the experimental data.

In order to solve the first question he constructs two models: a global conduction-radiation model with and without melt convection. In both models he uses the axisymmetry and quasi-steadiness assumptions. He solves the first model by using a commercial finite element program ABAQUS. Convection in the second model is taken into account by computing heat transfer in the melt separately with an other commercial code STAR-CD. He concludes that the conduction-radiation model can not predict the temperature distribution in the melt realistically. The model without convection is well suited for predicting the temperature field in the other parts of the Czochralski furnace. The model with convection predicts the temperature distribution in the melt fairly well when compared to the measured results.

The second question, i.e., whether there are cases of interest in which the computation has to be carried out in three dimensions, he approaches in the following way: He constructs a three dimensional, finite volume method based Navier-Stokes solver and combines it with the global conduction-radiation model by matching the temperatures on the boundaries of the melt. The numerical results indicate that the temperature distribution in the melt is in qualitative agreement with the experimental results. As long as the crucible rotation rate is low, two dimensional temperature distribution is very similar as in three dimensional case. With the high crucible rotation rates the flow pattern turns to three dimensional.

In [Kakimoto91] the authors have constructed an X-ray radiography system for visualizing the silicon melt flow in the Czochralski process. The diameters of crystals vary in the range of 2.32-4.4 cm. They use a relatively small crucible which diameter is 7.5 cm in minimizing the effects of flow instabilities. They make comparisons between measurements and numerical results in this geometry.

Their numerical study is based on the computation of the melt flow, heat conduction and heat transfer by radiation. The Czochralski furnace consists of macro-elements (such as melt, crystal, heater etc.) whose boundaries interact through radiation. The shape of the melt-gas interface is determined by the Laplace-Young equation in which the surface tension is included. The crystal-melt interface includes heat generation by solidification. The authors neglect gas convection and they assume that the pulling velocity of the crystal as well as the position of the triple point, i.e., the point where the free boundaries between melt and gas, melt and crystal and crystal and gas run across, are fixed.

Their numerical simulations are performed under assumption of the axisymmetric geometry and steady flow. They reach convergence without the crystal and crucible rotations with the real or nearly real Rayleigh and Reynolds numbers. However, it is not possible for them to obtain convergence for more than several percent of the real Rayleigh and Reynolds numbers for the case of the crystal and crucible rotations. In order to reach the numerical solution of the real flow, the authors use a technique based on the extrapolation of stream functions obtained from computations with reduced Reynolds numbers. According to Kakimoto et al they

have obtained almost identical flow fields compared to experimental results with this technique.

Kinney et al ([Kinney93a], [Kinney93b]) have developed an integrated hydrodynamic thermal-capillary model. They compare numerical results of the model to experimental measurements of the thermal field from growth of 83 mm diameter crystals and the melt-crystal interface shape of the 100 mm diameter crystals obtained in the conventional Czochralski silicon crystal growth. Their axisymmetric model includes steady state flow (laminar in [Kinney93a] and turbulent in [Kinney93b]) driven by the crystal and crucible rotations, natural convection and thermocapillarity. The temperature field is computed throughout all components of the Czochralski furnace and the components are assumed to exchange heat by the diffuse-gray radiation. The calculation of the diffuse-gray radiation is based on the Gebhart method. The shape of the melt-gas interface is determined from the balance of normal stresses at this boundary and the crystal-melt interface as the melting point isotherm. The thermal stresses in the crystal are computed after the temperature distribution in the crystal is known. Their numerical simulation tools are based on the finite element approximation to the field variables and the positions of the interfaces.

If the melt flow is assumed to be laminar, they find the solution for the combined driving forces only when the viscosity of the melt is set artificially high. The temperature distribution outside of the melt coincides with the experimental data. The shape of the crystal-melt interface is, however, quite far from the measured shape of the interface. If the melt flow is instead assumed to be turbulent, also the shape of the crystal-melt interface corresponds to the measured one. The viscosity of the melt differs only slightly from the viscosity of silicon. Although their results are very satisfactory, they emphasize that in large diameter Czochralski systems the melt flow is transient and three dimensional.

In this work we divide the entire Czochralski crystal growth process into subproblems from the mathematical modeling and numerical simulation point of view. We describe mathematically thermally coupled liquid flows first in simple two dimensional geometries and then extend our consideration to the silicon melt flow in the axisymmetric geometry. The models consist of the coupled heat and Navier-Stokes equations with Dirichlet boundary conditions on the liquid boundaries and Robin boundary condition for temperature at the liquid-gas interface (if present). The flow is either steady or transient and driven by the Grashof, Marangoni or forced convections. The models are solved numerically and computational results obtained in two dimensional geometries are compared to those found in the literature. We emphasize that in the study of the silicon melt flow we examine the physical phenomena only in the melt, i.e., the surrounding parts of the melt, such as the silica crucible, the graphite susceptor, the heater and the crystal are not taken into account.

After thermally coupled liquid flows we consider the axisymmetric crystal-melt

system in which the mathematical equations are now written for enthalpy and velocity. The enthalpy and Navier-Stokes equations are coupled and temperature is expressed as a function of enthalpy. The melt flow is driven by the Grashof, Marangoni and forced convections. The definition of the free boundary between the crystal and the melt is included to the definition of enthalpy.

We stress, however, that our final aim in this work is to present a mathematical model and numerical simulation tools for the entire Czochralski system in the axisymmetric geometry. The model consists of the time dependent Navier-Stokes and enthalpy equations for the melt flow and heat transfer in the whole Czochralski furnace. The flow is driven by the Grashof, Marangoni and forced convections. Inside of each domain heat is transferred by conduction and in the crystal and melt also by convection. Heat between various surfaces is transferred by radiation which is assumed to be diffuse and gray. The shape of the melt-gas interface is based on the analytical representation of the shape of the meniscus presented by Hurle, [Hurle83]. The diameter of the crystal and the pulling velocity of the crystal are assumed to be constant. The mathematical model of the entire Czochralski process is solved numerically by the finite element method.

In comparison of our research to the works of Müller, Kakimoto et al and Kinney et al it is noteworthy that the other works have been carried out by using either the steady-state or the quasi steady-state assumption. These are, in principle, acceptable assumptions since time scales in the Czochralski crystal growth are so different. Typical growing rates of crystals are 0.5-2 mm/minute while maximum velocities in the melt are of the order of centimeters/second and therefore there is no need to model crystal growth from the melt dynamically. All authors, however, stress that the key for the successful numerical simulation is the correct description of the melt flow which should be made with time dependent analysis.

The basic difference between the work of Müller and ours is that Müller uses mainly commercial program packages and we develop simulation tools ourselves. This is certainly a more time-consuming way to proceed than the use of program packages which contain tools for many applications. However, they do not always offer desired modeling capabilities which can be observed in the case of ABAQUS, [Müller93].

In the paper of Kakimoto et al the Czochralski furnace is constructed by several macro-elements. The macro-element boundaries interact through radiation. The concept of macro-elements usually refers to a case where a macro-element surface in a discrete case is a collection of adjacent element sides. Each element side has various physical quantities and on the macro-element surface effective physical parameters such as effective temperature and emissivity are applied. In our work heat is transferred in a discrete case by radiation between finite element surfaces, not between the macro-elements.

Kinney et al determine the shape of the melt-gas interface from the balance of normal stresses on this boundary and the crystal-melt interface as the melting

point isotherm. As the field variables, also positions of the free boundaries are treated as unknowns. The computation of the diffuse-gray radiation is based on the Gebhart method. In our work the shape of the melt-gas interface is based on the analytical representation of the shape of the meniscus presented by Hurle, [Hurle83]. This representation has been shown to compare quite well with the full iterative numerical solution of the Laplace-Young equation with the appropriate parameters of germanium. The free boundary between the crystal and the melt is solved by the enthalpy method. This method is a typical fixed grid method, i.e., our finite element mesh stays unchanged during simulations. View factors required in the modeling of radiation are computed by taking advantage of the axisymmetry of the Czochralski geometry. The discretization in the azimuthal direction is not necessary as made in [Kinney93a] and [Kinney93b] (see references therein).

3. Mathematical Models

In this chapter we shall first deal with the subproblems of the Czochralski crystal growth process, such as the thermally coupled melt flow and the phase change between the crystal and the melt, before the whole problem will be discussed. For each problem a mathematical model will be introduced. Later on in Chapters 4, 5 and 6 the mathematical models are solved numerically.

There are several reasons for dividing the whole problem into separate parts. First, the crystal growth process has several individual physical phenomena, e.g., thermally coupled melt flow, phase change and radiation, which require closer study. Secondly, the division of the whole problem into subproblems offers a natural way to put the whole mathematical model together logically piece by piece, and to apply numerical simulation tools for each sub-model separately. Finally, with the help of the sub-models it is more convenient to test the reliability of numerical methods by comparing results to those found in the literature.

In Chapter 3.1 we shall introduce mathematical models first to thermally coupled liquid flows in simple two dimensional geometries and then to axisymmetric melt flow in the Czochralski crystal growth context. The mathematical models for the crystal-melt system and the entire Czochralski crystal growth are presented in Chapters 3.2 and 3.3.

3.1 Thermally Coupled Liquid Flows

In Chapter 3.1.1 we shall present first a mathematical model for a two dimensional vessel filled with a liquid where steady state flow is driven by the Grashof and Marangoni convections. The second mathematical model in Chapter 3.1.2 concerns the time dependent Rayleigh-Bénard convection in a rectangular box. These models are presented in detail in [Argyris92] and [Cuvelier86b]. We solve the models numerically in Chapters 4.4.1 and 4.4.2 and compare the numerical results to those presented in these references. In this sense these models operate as verification tools for this work. The mathematical model in Chapter 3.1.3 describes the melt flow in axisymmetric geometry. The melt flow is caused by the Grashof and Marangoni convections and the rotation of the melt.

We begin with the derivation of the coupled three dimensional Navier-Stokes and heat equations and then pay attention to the mathematical models.

The Navier-Stokes and heat equations can be derived from the basic principles of the conservation of mass, momentum and energy, [Landau91]. We introduce first the Navier-Stokes equations and then the heat equation.

The mass conservation in the liquid is described by the equation

$$\frac{\partial \rho}{\partial t} + \nabla \cdot (\rho \vec{u}) = 0, \tag{3.1}$$

where t is time and ρ and $\vec{u}$ are the density and velocity of the liquid. If the liquid is assumed to be incompressible, the density is constant and the equation (3.1) reduces to

$$\nabla \cdot \vec{u} = 0. \tag{3.2}$$

The conservation of momentum is

$$\rho \frac{\partial \vec{u}}{\partial t} + \rho(\vec{u} \cdot \nabla)\vec{u} - \nabla \cdot \bar{\bar{\sigma}} = \rho \vec{f}, \tag{3.3}$$

where $\bar{\bar{\sigma}}$ is the stress tensor, $\nabla \cdot \bar{\bar{\sigma}} = (\nabla \cdot \vec{\sigma}_1, \nabla \cdot \vec{\sigma}_2, \nabla \cdot \vec{\sigma}_3)$ and $\vec{f}$ the body force which is assumed to consist of the gravitational force, i.e., $\vec{f} = \vec{g}$. If we assume that the liquid is Newtonian we come to an equation for the stress tensor

$$\bar{\bar{\sigma}} = -pI + 2\mu\bar{\bar{\varepsilon}} - \frac{2}{3}\mu\,(\nabla \cdot \vec{u})\,I, \tag{3.4}$$

where p is the static pressure, I the unit tensor, μ the dynamic viscosity of the liquid and $\bar{\bar{\varepsilon}}$ the strain rate tensor. The components of the linear strain rate tensor have the form

$$\varepsilon_{ij} = \frac{1}{2}\left(\frac{\partial u_i}{\partial x_j} + \frac{\partial u_j}{\partial x_i}\right), \tag{3.5}$$

$i, j = 1, \ldots, 3$. If we combine the equations (3.3)-(3.4) and use the continuity equation (3.2) and condition $\vec{f} = \vec{g}$, we arrive at the stress formulation of the Navier-Stokes equations

$$\begin{cases} \rho \dfrac{\partial \vec{u}}{\partial t} - \nabla \cdot (2\mu\bar{\bar{\varepsilon}}) + \rho(\vec{u} \cdot \nabla)\vec{u} + \nabla p = \rho \vec{g} \\ \nabla \cdot \vec{u} = 0. \end{cases} \tag{3.6}$$

In the following we assume that the Boussinesq approximation is valid in the liquid. This means that the density of the liquid is constant except in the body force term where the density depends linearly on temperature through the equation

$$\rho = \rho_0(1 - \beta(T - T_0)), \tag{3.7}$$

where T is the temperature, β the volume expansion coefficient and the subscript 0 refers to a reference state. The equation (3.7) causes a force $\rho_0 \vec{g}(1 - \beta(T - T_0))$ due

to temperature variations in the liquid. This phenomenon is called the Grashof convection or the natural convection. The Navier-Stokes equations in (3.6) can now be rewritten in the form

$$\left\{ \begin{array}{c} \rho_0 \dfrac{\partial \vec{u}}{\partial t} - \nabla \cdot (2\mu\bar{\bar{\varepsilon}}) + \rho_0(\vec{u}\cdot\nabla)\vec{u} + \nabla p = \rho_0\vec{g}(1-\beta(T-T_0)) \\ \nabla \cdot \vec{u} = 0. \end{array} \right. \tag{3.8}$$

The energy equation has the form

$$\rho \frac{De}{Dt} + \nabla \cdot \vec{q} - \bar{\bar{\sigma}} : \nabla\vec{u} = \rho h, \tag{3.9}$$

where e is the energy per unit mass, $\vec{q}$ the heat flux through the material surface, and h the heat source. We assume that the motion generates no heat, i.e., $\bar{\bar{\sigma}} : \nabla\vec{u} = -p\nabla\cdot\vec{u}$.

If we use the conservation of mass (3.1), assume the dependence of the energy and the density on temperature and pressure and apply the Fourier's law we arrive finally at the heat equation

$$\rho c_p \left(\frac{\partial T}{\partial t} + \vec{u}\cdot\nabla T \right) - \nabla\cdot(k\nabla T) = \rho h, \tag{3.10}$$

where c_p is the heat capacity at constant pressure and k the heat conductivity of the material.

Combining the equations (3.8) and (3.10) the coupled Navier-Stokes and heat equations read

$$\left\{ \begin{array}{c} \rho_0 \dfrac{\partial \vec{u}}{\partial t} - \nabla \cdot (2\mu\bar{\bar{\varepsilon}}) + \rho_0(\vec{u}\cdot\nabla)\vec{u} + \nabla p = \rho_0\vec{g}(1-\beta(T-T_0)) \\ \nabla \cdot \vec{u} = 0 \\ \rho_0 c_p \left(\dfrac{\partial T}{\partial t} + \vec{u}\cdot\nabla T \right) - \nabla\cdot(k\nabla T) = \rho_0 h. \end{array} \right. \tag{3.11}$$

3.1.1 Grashof and Marangoni Convections in 2D

In [Cuvelier86b] the authors study a two-dimensional steady non-isothermal flow problem in a vessel $\Omega = \{0 < x_1 < L,\ 0 < x_2 < L\}$, where the boundary $\partial\Omega$ is assumed to compose of mutually disjoint and open sets Γ_0, Γ_1, Γ_2 and Γ_3 in $\partial\Omega$ such that $\partial\Omega = \Gamma_0 \cup \Gamma_1 \cup \Gamma_2 \cup \Gamma_3$, Figure 3.1. The boundaries Γ_1, Γ_2 and Γ_3 are considered as fixed walls whereas Γ_0 is a fixed interface between the liquid and the surrounding gas through which there is no flow. The motion of the fluid is

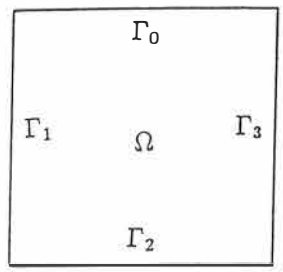

Figure 3.1 Problem presented in [Cuvelier86b]

caused by the Grashof and Marangoni convections. Temperature on Γ_1, Γ_2 and Γ_3 is fixed and heat flux on Γ_0 is assumed to be zero.

A mathematical model consisting of the steady-state and coupled Navier-Stokes and heat equations for the problem is: Find the velocity vector $\vec{u} = (u_1, u_2)$ and the pressure and temperature fields p and T such that

$$\text{(M1)} \qquad \begin{cases} -\nabla \cdot (2\mu\bar{\bar{\varepsilon}}) + \rho_0(\vec{u}\cdot\nabla)\vec{u} + \nabla p = -\rho_0\vec{g}\beta(T - T_0) \text{ in } \Omega \\ \nabla \cdot \vec{u} = 0 \text{ in } \Omega \\ \rho_0 c_p\,(\vec{u}\cdot\nabla T) - \nabla\cdot(k\nabla T) = 0 \text{ in } \Omega \\ \sigma_\tau = \dfrac{\partial\gamma}{\partial\tau},\ \vec{u}\cdot\vec{n} = 0,\ -k\dfrac{\partial T}{\partial n} = 0 \quad \text{on } \Gamma_0 \\ \vec{u} = 0,\ T = T_0 + \dfrac{1}{2} \quad \text{on } \Gamma_1 \\ \vec{u} = 0,\ T = T_0 + \dfrac{1}{2} - \dfrac{x_1}{L} \quad \text{on } \Gamma_2 \\ \vec{u} = 0,\ T = T_0 - \dfrac{1}{2} \quad \text{on } \Gamma_3. \end{cases}$$

It is assumed that there is no heat source in Ω and the material parameters are constant. Above γ is the surface tension coefficient, $\vec{\tau}$ the unit tangent vector and $\vec{n}$ the unit normal vector. The pressure gradient is in fact $\nabla p = \nabla(p - \rho_0 g_k x_k)$, $k = 1, 2$, where the term $\rho_0 g_k x_k$ is hydrostatic pressure and $p - \rho_0 g_k x_k$ the deviation from hydrostatic pressure.

The coefficient γ is a thermophysical property which depends on temperature. Temperature differences at the interface have an influence on the transport of momentum and heat near the interface. This phenomenon is called the Marangoni convection or the thermocapillary convection. The temperature dependence of the surface tension coefficient can be assumed to be linear, [Cuvelier86]:

$$\gamma = \gamma_0(1 - \vartheta(T - T_0)), \tag{3.12}$$

where ϑ is the temperature coefficient of the surface tension and the subscript 0 refers to a reference state. The boundary condition for the tangential stress then becomes

$$\sigma_\tau = -\vartheta\gamma_0 \frac{\partial T}{\partial \tau} \quad \text{on } \Gamma_0. \tag{3.13}$$

3.1.2 Rayleigh-Bénard Convection

In [Argyris92] the authors examine the transient Rayleigh-Bénard convection in a two dimensional rectangular box

$$\Omega = \{-L_1 < x_1 < L_1, 0 < x_2 < L_2\}$$

and consider the half of the box $\hat{\Omega} = \{0 < x_1 < L_1,\ 0 < x_2 < L_2\}$. The boundary $\partial\hat{\Omega}$ is composed of mutually disjoint and open sets Γ_0, Γ_1, Γ_2 and Γ_3 in $\partial\hat{\Omega}$ such that $\partial\hat{\Omega} = \Gamma_0 \cup \Gamma_1 \cup \Gamma_2 \cup \Gamma_3$, Figure 3.2.

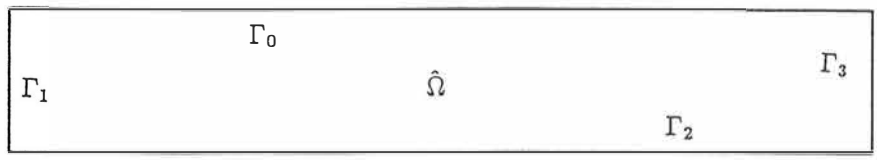

Figure 3.2 Geometry of Rayleigh-Benard convection

It is assumed that the lower and the upper plate of the box are held at a constant temperature. Temperature of the lower plate is set to be 0.5 degrees higher than temperature of the upper plate. Heat fluxes on the vertical side walls are assumed to be zero. The fluid is initially set at same temperature as the upper plate and it is assumed to be in a motionless state.

A mathematical model containing the transient and coupled Navier-Stokes and heat equations for the problem is formulated as follows: Find the velocity vector

$\vec{u} = (u_1, u_2)$ and the pressure and temperature fields p and T such that

$$
\text{(M2)} \quad \left\{ \begin{aligned}
\rho_0 \frac{\partial \vec{u}}{\partial t} - \nabla \cdot (2\mu\bar{\bar{\varepsilon}}) + \rho_0(\vec{u}\cdot\nabla)\vec{u} + \nabla p &= -\rho_0 \vec{g}\beta(T - T_0) \text{ in } \hat{\Omega} \times (0, t_0) \\
\nabla \cdot \vec{u} &= 0 \text{ in } \hat{\Omega} \times (0, t_0) \\
\rho_0 c_p \left(\frac{\partial T}{\partial t} + \vec{u}\cdot\nabla T \right) - \nabla \cdot (k\nabla T) &= 0 \text{ in } \hat{\Omega} \times (0, t_0) \\
\vec{u}(\vec{x}, 0) = 0, \quad T(\vec{x}, 0) &= T_0 \text{ in } \hat{\Omega} \\
\vec{u} = 0, \quad T &= T_0 \quad \text{on } \Gamma_0 \times (0, t_0) \\
u_1 = 0, \quad -k\frac{\partial T}{\partial n} &= 0 \quad \text{on } \Gamma_1 \times (0, t_0) \\
\vec{u} = 0, \quad T &= T_0 + 0.5 \quad \text{on } \Gamma_2 \times (0, t_0) \\
\vec{u} = 0, \quad -k\frac{\partial T}{\partial n} &= 0 \quad \text{on } \Gamma_3 \times (0, t_0),
\end{aligned} \right.
$$

where t_0 is a fixed number. As in the previous chapter it is assumed that the heat source h is zero and the material parameters are constant.

3.1.3 Axisymmetric Melt Flow

During the Czochralski silicon crystal growth process convection plays an important role in heat and mass transfer in the melt. The temperature distribution is strongly dependent on convection. On the other hand, the hot silicon melt erodes the silica crucible and oxygen dissolves to the melt. In the melt oxygen is transported by convection.

The trend towards large diameter single crystals is obvious in the future. In the conventional Czochralski crystal growth 12 inch single silicon crystals have already been grown. The lengths of such crystals are, however, quite modest and the portion of the crystal shoulder and the end-cone can be significant. In the continuous Czochralski crystal growth [Anselmo93] the polysilicon pellets ($\approx$ 1 mm diameter) are fed continuously into the melt. The total volume of the melt and consequently the lengths of grown crystals are therefore larger. The problem in this method is, however, the drifting of the pellets along the melt flow towards the crystal and the possible sticking of the pellets on the crystal.

For these reasons it is quite justified to build a mathematical model and numerical simulation tools for a pure melt flow and a crystal-melt system in order to understand and study the predominant physical phenomena. In the following, mathematical models for a melt flow and crystal-melt system (Chapter 3.2) are constructed.

Due to the symmetry of the Czochralski configuration the temperature distribution and the flow pattern in the melt can be modeled fairly well with the axisymmetric

heat equation and cylindrically symmetric Navier-Stokes equations, [Müller93]. With the high crucible rotation rates the velocity pattern in the melt is obviously three dimensional, [Müller93], and in some cases perhaps turbulent, [Kinney93a]. In this research we neglect three dimensional and turbulent effects.

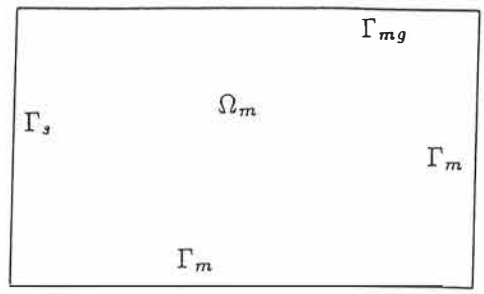

Figure 3.3 Melt flow geometry

The melt flow geometry is depicted in Figure 3.3. Our mathematical model consists of the time dependent and coupled Navier-Stokes and heat equations in the melt Ω_m. The melt flow is driven by the Grashof and Marangoni convections and the centrifugal force caused by the rotation of the melt. On the melt boundary Γ_m, the Dirichlet boundary conditions for temperature and the velocity components are applied. At the melt-gas interface we set the Robin boundary condition for temperature. The boundary conditions for normal and tangential stresses and normal velocities on Γ_{mg} are stated. Also on the symmetry axis Γ_s a special attention to the boundary conditions is required.

Our mathematical model in this case is the following: Find the velocity vector $\vec{u} = (u_r, u_z, u_\theta)$, the pressure p and the temperature T such that

(M3)

$$
\begin{cases}
\rho_m \dfrac{\partial u_r}{\partial t} - \dfrac{\partial \sigma_{zr}}{\partial z} - \dfrac{1}{r}\dfrac{\partial}{\partial r}(r\sigma_{rr}) + \dfrac{1}{r}\sigma_{\theta\theta} + \rho_m \left(u_r \dfrac{\partial u_r}{\partial r} + u_z \dfrac{\partial u_r}{\partial z} - \dfrac{u_\theta^2}{r} \right) = 0 \\
\rho_m \dfrac{\partial u_z}{\partial t} - \dfrac{\partial \sigma_{zz}}{\partial z} - \dfrac{1}{r}\dfrac{\partial}{\partial r}(r\sigma_{zr}) + \rho_m \left(u_r \dfrac{\partial u_z}{\partial r} + u_z \dfrac{\partial u_z}{\partial z} \right) = \\
= \rho_m g \beta (T - T_0) \\
\rho_m \dfrac{\partial u_\theta}{\partial t} - \dfrac{1}{r^2}\dfrac{\partial}{\partial r}(r^2\sigma_{r\theta}) - \dfrac{\partial \sigma_{\theta z}}{\partial z} + \rho_m \left(u_r \dfrac{\partial u_\theta}{\partial r} + u_z \dfrac{\partial u_\theta}{\partial z} + \dfrac{u_r u_\theta}{r} \right) = 0 \\
\dfrac{1}{r}\dfrac{\partial}{\partial r}(r u_r) + \dfrac{\partial u_z}{\partial z} = 0 \\
\rho_m c_{p_m} \left(\dfrac{\partial T}{\partial t} + u_r \dfrac{\partial T}{\partial r} + u_z \dfrac{\partial T}{\partial z} \right) - \dfrac{1}{r}\dfrac{\partial}{\partial r}\left(kr \dfrac{\partial T}{\partial r} \right) - \dfrac{\partial}{\partial z}\left(k \dfrac{\partial T}{\partial z} \right) = 0
\end{cases}
$$

in $\Omega_m \times (0, t_0)$ with

$$\begin{cases} \vec{u}(r,z,0) = \vec{u}^0(r,z), \;\; T(r,z,0) = T^0(r,z) \;\; \text{in } \Omega_m \\ u_r = 0, \;\; \dfrac{\partial u_z}{\partial r} = 0, \;\; u_\theta = 0, \;\; \dfrac{\partial T}{\partial r} = 0 \;\; \text{on } \Gamma_s \times (0,t_0) \\ u_r = 0, \;\; u_z = 0, \;\; u_\theta = \omega_m r, \;\; T = T_0 \;\; \text{on } \Gamma_m \times (0,t_0) \\ \vec{u}\cdot\vec{n} = 0, \;\; \sigma_n = \dfrac{\gamma_0}{R} - p_a, \;\; \sigma_\tau = -\vartheta\gamma_0 \dfrac{\partial T}{\partial \tau}, \;\; -k\dfrac{\partial T}{\partial n} = \alpha(T - T_{ext}) \\ \qquad\qquad \text{on } \Gamma_{mg} \times (0,t_0). \end{cases}$$

The components of the stress tensor are

$$\sigma_{zr} = \mu_m \left(\frac{\partial u_r}{\partial z} + \frac{\partial u_z}{\partial r} \right), \tag{3.14a}$$

$$\sigma_{rr} = -p + 2\mu_m \frac{\partial u_r}{\partial r}, \tag{3.14b}$$

$$\sigma_{\theta\theta} = -p + 2\mu_m \frac{u_r}{r}, \tag{3.14c}$$

$$\sigma_{r\theta} = \mu_m r \frac{\partial}{\partial r}\left(\frac{u_\theta}{r}\right), \tag{3.14d}$$

$$\sigma_{\theta z} = \mu_m \frac{\partial u_\theta}{\partial z}, \tag{3.14e}$$

$$\sigma_{zz} = -p + 2\mu_m \frac{\partial u_z}{\partial z}. \tag{3.14f}$$

For further details on the cylindrically symmetric Navier-Stokes equations and axisymmetric heat equation we refer to [Landau91]. In the mathematical model the heat source in the melt is assumed to be zero and the gravity $\vec{g}$ acts in the direction of the negative z-axis. The parameter ω_m is the rotation rate of the melt, R the radius curvature of Γ_{mg}, p_a the outside pressure, α the heat transfer coefficient and T_{ext} the external temperature to the melt. The mean curvature for a function $\Gamma_{mg} : r \mapsto \Gamma_{mg}(r)$, $r \in [0, r_0]$ is given by [Cuvelier87]

$$\frac{1}{R} = \frac{1}{r}\frac{\partial}{\partial r}\left(\frac{r\frac{\partial}{\partial r}\Gamma_{mg}}{\sqrt{1 + |\frac{\partial}{\partial r}\Gamma_{mg}|^2}} \right).$$

3.2 Crystal Growth from Melt

A crucial task in this section is to treat a two phase problem between the crystal and the melt, separated by a free boundary, Figure 3.4. In this work we assume that the radius of the crystal is constant. We do not analyze the mechanisms

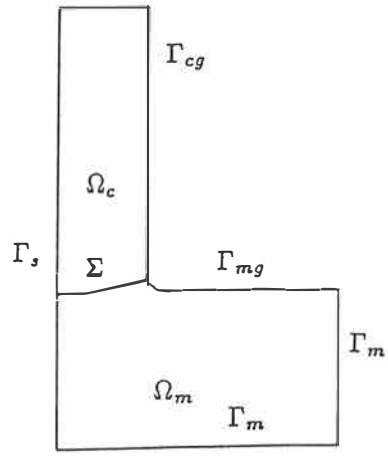

Figure 3.4 Problem statement: crystal and melt separated by free boundary

connected with the three-phase point. From these parts we refer to [Sackinger89] and [Seifert96].

We assume that the crystal-melt system can be modeled in the axisymmetric geometry. Let us recall the axisymmetric heat equation (no heat source) and write it in the crystal and melt as follows:

$$\frac{\partial}{\partial t}\left(\rho_i c_{p_i} T_i\right) + \vec{u}_i \cdot \nabla(\rho_i c_{p_i} T_i) - \frac{1}{r}\frac{\partial}{\partial r}\left(k_i r \frac{\partial T_i}{\partial r}\right) - \frac{\partial}{\partial z}\left(k_i \frac{\partial T_i}{\partial z}\right) = 0 \tag{3.15}$$

in $\Omega_i \times (0, t_0)$, $i = c, m$, where c corresponds the crystal and m the melt. ρ_i, c_{p_i} and k_i, $i = c, m$, are the density, heat capacity and heat conductivity in the crystal and melt, respectively, and they are assumed to be constant in both phases.

Beside the initial and boundary conditions imposed on the boundaries of Ω_i, $i = c, m$, the following conditions have to be fulfilled on the free boundary Σ:

$$T_m = T_c = T_f \quad \text{on } \Sigma \times (0, t_0), \tag{3.16a}$$

$$k_m \frac{\partial T_m}{\partial n_\Sigma} - k_c \frac{\partial T_c}{\partial n_\Sigma} = \rho_c L(\vec{v}_c - \vec{v}_\Sigma) \cdot \vec{n}_\Sigma \quad \text{on } \Sigma \times (0, t_0), \tag{3.16b}$$

where T_f is the melting temperature, L the latent heat, $\vec{v}_c$ and $\vec{v}_\Sigma$ the velocities of the crystal and interface, respectively, and n_Σ the unit normal vector on Σ directed to the crystal.

The numerical solution of the phase change problem (3.15) & (3.16a-b) is considered in more detail in Chapter 5. In this work the phase change problem is solved by the enthalpy method. Instead of formulating the problem with the help of the heat equation (3.15) and boundary conditions (3.16a-b), we introduce an equation for enthalpy and treat enthalpy as a primary unknown. Enthalpy is defined so that the phase change is included into the equation of enthalpy.

Let us assume for a moment that the melting temperature T_f in (3.16a) is equal to zero. If we define the enthalpy as ([White82])

$$H(T) = \begin{cases} \rho_c c_{p_c} T, & T < 0 \\ [0, \rho_c L], & T = 0 \\ \rho_m c_{p_m} T + \rho_c L, & T > 0 \end{cases} \tag{3.17}$$

and use the Kirchhoff transformation

$$K(T) = \int_0^T k(\xi)\ d\xi = \begin{cases} k_c T, & T < 0 \\ k_m T, & T > 0 \end{cases} \tag{3.18}$$

the heat equation (3.15) can be rewritten in the form

$$\frac{\partial}{\partial t} H(T) + \vec{u} \cdot \nabla H(T) - \frac{1}{r} \frac{\partial}{\partial r} \left(r \frac{\partial}{\partial r} K(T) \right) - \frac{\partial}{\partial z} \left(\frac{\partial}{\partial z} K(T) \right) = 0 \tag{3.19}$$

in $\Omega \times (0, t_0)$, where $\Omega = \Omega_m \cup \Omega_c$ is now the whole domain. The functions $H(T)$ and $K(T)$ are presented in Figure 3.5.

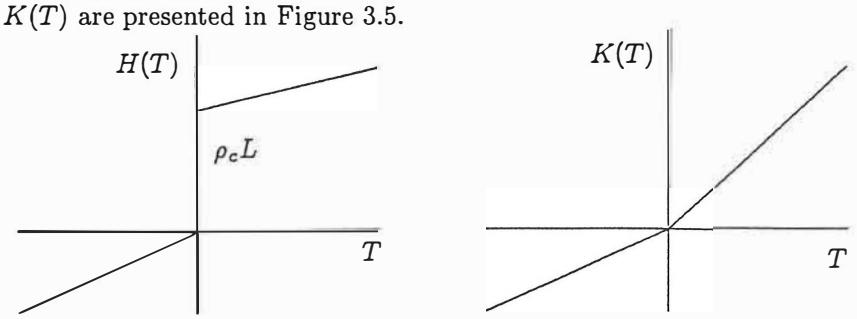

Figure 3.5 Functions H and K as a function of temperature

The equation (3.19) is, however, not meaningful since the enthalpy defined in (3.17) has a jump discontinuity as can be seen in Figure 3.5. This is not a real problem since the definition of enthalpy can be changed as proposed in [Dalhuijsen86], Figure 3.6. That is, temperature as a function of enthalpy is defined so that it is continuous also in the interval $[-\frac{\varepsilon}{2}, \frac{\varepsilon}{2}]$ around the melting temperature.

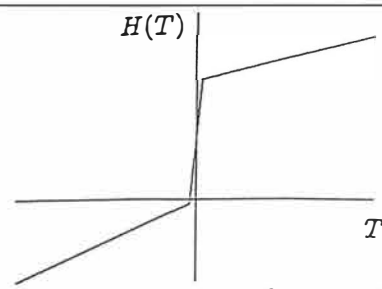

Figure 3.6 Continuous enthalpy as a function of temperature

Instead of defining enthalpy as a function of temperature we write temperature as a function of enthalpy (Figure 3.7)

$$T(H) = \begin{cases} \dfrac{1}{\rho_c c_{p_c}} H, & H < 0 \\ 0, & H \in [0, \rho_c L] \\ \dfrac{H - \rho_c L}{\rho_m c_{p_m}}, & H > \rho_c L. \end{cases} \tag{3.20}$$

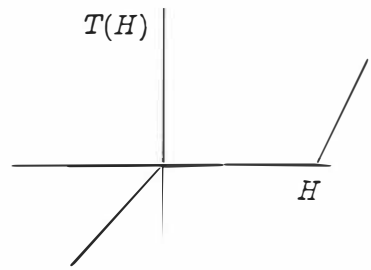

Figure 3.7 Temperature as a function of enthalpy

By using now the Kirchhoff transformation (3.18) and by introducing a function

$$\Phi(H) = \begin{cases} \dfrac{k_c}{\rho_c c_{p_c}} H, & H < 0 \\ 0, & H \in [0, \rho_c L] \\ \dfrac{k_m (H - \rho_c L)}{\rho_m c_{p_m}}, & H > \rho_c L \end{cases} \tag{3.21}$$

we arrive at the equation

$$\frac{\partial}{\partial t} H + \vec{u} \cdot \nabla H - \frac{1}{r} \frac{\partial}{\partial r} \left(r \frac{\partial}{\partial r} \Phi(H) \right) - \frac{\partial}{\partial z} \left(\frac{\partial}{\partial z} \Phi(H) \right) = 0 \tag{3.22}$$

in $\Omega \times (0, t_0)$.

If the melting temperature is not equal to zero, then the functions $H(T)$, $K(T)$, $T(H)$ and $\Phi(H)$ have the forms

$$H(T) = \begin{cases} \rho_c c_{p_c} T, & T < T_f \\ [\rho_c c_{p_c} T_f, \rho_c c_{p_c} T_f + \rho_c L], & T = T_f \\ \rho_m c_{p_m}(T - T_f) + \rho_c c_{p_c} T_f + \rho_c L, & T > T_f, \end{cases} \tag{3.23}$$

$$K(T) = \begin{cases} k_c T, & T < T_f \\ k_m T + (k_c - k_m) T_f, & T > T_f, \end{cases} \tag{3.24}$$

$$T(H) = \begin{cases} \dfrac{1}{\rho_c c_{p_c}} H, & H < \rho_c c_{p_c} T_f \\ T_f, & H \in [\rho_c c_{p_c} T_f, \rho_c c_{p_c} T_f + \rho_c L] \\ \dfrac{H - \rho_c L - \rho_c c_{p_c} T_f}{\rho_m c_{p_m}} + T_f, & H > \rho_c c_{p_c} T_f + \rho_c L \end{cases} \tag{3.25}$$

and

$$\Phi(H) = \begin{cases} \dfrac{k_c}{\rho_c c_{p_c}} H, & H < \rho_c c_{p_c} T_f \\ k_c T_f, & H \in [\rho_c c_{p_c} T_f, \\ & \rho_c c_{p_c} T_f + \rho_c L] \\ \dfrac{k_m(H - \rho_c L - \rho_c c_{p_c} T_f)}{\rho_m c_{p_m}} + k_m T_f + (k_c - k_m) T_f, & H > \\ & \rho_c c_{p_c} T_f + \rho_c L. \end{cases} \tag{3.26}$$

The definition of the function $\Phi(H)$ (or $H(T)$ or $T(H)$) indicates that there are in fact three different phases. Besides the solid and liquid phases there is a so called mushy region where the enthalpy belongs to the interval $[\rho_c c_{p_c} T_f, \rho_c c_{p_c} T_f + \rho_c L]$ and the latent heat is released.

We are still lacking the equations of the melt flow and the appropriate boundary conditions for enthalpy and velocity. The melt flow is governed by the cylindrically symmetric Navier-Stokes equations in Ω_m as in Chapter 3.1.3. On the symmetry axis we define the Dirichlet and homogeneous Neumann type boundary conditions for the function $\Phi(H)$ and velocity. On Γ_m the Dirichlet boundary conditions for the enthalpy and the velocity components are applied. At the melt-gas interface, which is also a free boundary, the conditions for normal and tangential stresses and normal velocities are stated. At the phase change interface we assume that mass balance is fulfilled and the Dirichlet boundary conditions containing the rotation

rate of the crystal are applied. On $\Gamma_{mg} \cup \Gamma_{cg}$ the Robin type boundary condition for $\Phi(H)$ is applied.

The mathematical model for the crystal-melt system now reads: Find the velocity vector $\vec{u} = (u_r, u_z, u_\theta)$, the pressure p and the enthalpy H such that

(M4)

$$\begin{cases} \rho_m \dfrac{\partial u_r}{\partial t} - \dfrac{\partial \sigma_{zr}}{\partial z} - \dfrac{1}{r}\dfrac{\partial}{\partial r}(r\sigma_{rr}) + \dfrac{1}{r}\sigma_{\theta\theta} + \rho_m \left(u_r \dfrac{\partial u_r}{\partial r} + u_z \dfrac{\partial u_r}{\partial z} - \dfrac{u_\theta^2}{r} \right) = 0 \\ \rho_m \dfrac{\partial u_z}{\partial t} - \dfrac{\partial \sigma_{zz}}{\partial z} - \dfrac{1}{r}\dfrac{\partial}{\partial r}(r\sigma_{zr}) + \rho_m \left(u_r \dfrac{\partial u_z}{\partial r} + u_z \dfrac{\partial u_z}{\partial z} \right) = \\ \qquad = \rho_m g \beta (T - T_0) \\ \rho_m \dfrac{\partial u_\theta}{\partial t} - \dfrac{1}{r^2}\dfrac{\partial}{\partial r}(r^2\sigma_{r\theta}) - \dfrac{\partial \sigma_{\theta z}}{\partial z} + \rho_m \left(u_r \dfrac{\partial u_\theta}{\partial r} + u_z \dfrac{\partial u_\theta}{\partial z} + \dfrac{u_r u_\theta}{r} \right) = 0 \\ \dfrac{1}{r}\dfrac{\partial}{\partial r}(r u_r) + \dfrac{\partial u_z}{\partial z} = 0 \end{cases}$$

in $\Omega_m \times (0, t_0)$, $\Omega_m = \{\Phi(H) > k_c T_f\}$,

$$\frac{\partial}{\partial t} H + \vec{u} \cdot \nabla H - \frac{1}{r}\frac{\partial}{\partial r}\left(r \frac{\partial}{\partial r}\Phi(H) \right) - \frac{\partial}{\partial z}\left(\frac{\partial}{\partial z}\Phi(H) \right) = 0 \quad \text{in } \Omega \times (0, t_0),$$

$\Omega = \Omega_m \cup \Omega_c$, with the initial and boundary conditions

$$\begin{cases} \vec{u}(r, z, 0) = \vec{u}^0(r, z) \quad \text{in } \Omega \\ H(r, z, 0) = H^0(r, z) \quad \text{in } \Omega \\ u_r = 0, \ \dfrac{\partial u_z}{\partial r} = 0, \ u_\theta = 0, \quad \text{on } (\Gamma_s \cap \Omega_m) \times (0, t_0) \\ \dfrac{\partial \Phi(H)}{\partial r} = 0 \quad \text{on } \Gamma_s \times (0, t_0) \\ u_r = 0, \ u_z = 0, \ u_\theta = \omega_m r, \ H = H_0 \quad \text{on } \Gamma_m \times (0, t_0) \\ \vec{u} \cdot \vec{n} = 0, \ \sigma_n = \dfrac{\gamma_0}{R} - p_a, \ \sigma_\tau = -\vartheta \gamma_0 \dfrac{\partial T(H)}{\partial \tau} \quad \text{on } \Gamma_{mg} \times (0, t_0) \\ -\dfrac{\partial \Phi(H)}{\partial n} = \alpha(T(H) - T_{ext}) \quad \text{on } \Gamma_{mg} \times (0, t_0) \\ u_r = 0, \ u_z = 0, \ u_\theta = \omega_c r \quad \text{on } \Sigma \times (0, t_0) \\ \rho_m \vec{u}_m \cdot \vec{n}_\Sigma - \rho_c \vec{u}_c \cdot \vec{n}_\Sigma = (\rho_m - \rho_c) \vec{u}_\Sigma \cdot \vec{n}_\Sigma \quad \text{on } \Sigma \times (0, t_0) \\ -\dfrac{\partial \Phi(H)}{\partial n} = \alpha(T(H) - T_{ext}) \quad \text{on } \Gamma_{cg} \times (0, t_0), \end{cases}$$

where the components of the stress tensor are as in the equations (3.14a-f). ω_c is the rotation rate of the crystal and $\vec{u}_\Sigma$ the velocity of the interface Σ.

The equations in the mathematical model are highly nonlinear. The Navier-Stokes equations have nonlinear convection terms and are coupled with temperature. The enthalpy equation contains the function $\Phi(H)$ and the coupling with velocity. Furthermore, the domains depend on the positions of the free boundaries.

3.3 Czochralski Crystal Growth

In this chapter a mathematical model for the entire Czochralski crystal growth is constructed in the axisymmetric geometry, Figure 3.8. The model includes equations for global heat transfer and melt flow in the crucible. Global heat transfer includes transient equations for enthalpy (including the definition of the phase change interface) and heat exchange between various surfaces inside of the Czochralski configuration by radiation. The external temperature of the Czochralski furnace and the temperature of the low temperature enclosure are assumed to be known. The melt flow is governed by the transient Navier-Stokes equations and the boundary conditions for the melt flow are of the same type as in Chapter 3.2.

In the previous chapter we introduced an equation for enthalpy in the crystal-melt system in order to treat the phase change problem. In the surrounding parts of the crystal and melt the heat equation is adequate to describe heat transfer. We discuss later on in this chapter, how global heat transfer induced by conduction and convection is modeled by using these equations together. An other important task in this chapter is to treat radiation which plays a crucial role in heat transfer mechanism.

We characterize the axisymmetric domains by using the following notations: Crystal - Ω_c, melt - Ω_m, silica crucible - Ω_s, graphite susceptor - Ω_g, graphite resistance heater - Ω_h, crucible pedestal Ω_a and thermal shields - Ω_t. Every domain is characterized by different thermophysical properties. In reality these properties, such as the densities, heat capacities and heat conductivities, are temperature dependent. In this work, however, we assume that they are constant in each material.

The following notations for the boundaries in the system are applied: The crystal-gas interface is denoted by Γ_{cg}, the melt-gas interface by Γ_{mg} and the other interfaces connected to the gas by Γ_i. The melt-silica crucible interface is denoted by Γ_m and the low temperature enclosure by Γ_e. Finally the outer interface is denoted by Γ_o. The cylindrical co-ordinate system (r, z, θ) is centered at the bottom of the crucible shaft. We emphasize that Γ_e is only a one dimensional object in which temperature is known.

Let us begin with the modeling of radiation. The following discussion is based on the references [Incropera85], [Sparrow78], [Tiihonen94] and [Tiihonen96]. We make the following assumptions: The argon gas within the enclosure is non-participating and an opaque, diffuse and gray behavior from the surfaces is expected.

Consider a set $\Gamma = \Gamma_{cg} \cup \Gamma_{mg} \cup \Gamma_i \cup \Gamma_e$. On Γ heat balance reads as

$$q + J - R = 0, \tag{3.27}$$

where q is heat flux caused by conduction to the surface, J irradiation and R the radiosity on the surface. The radiosity can be expressed as a sum of surface

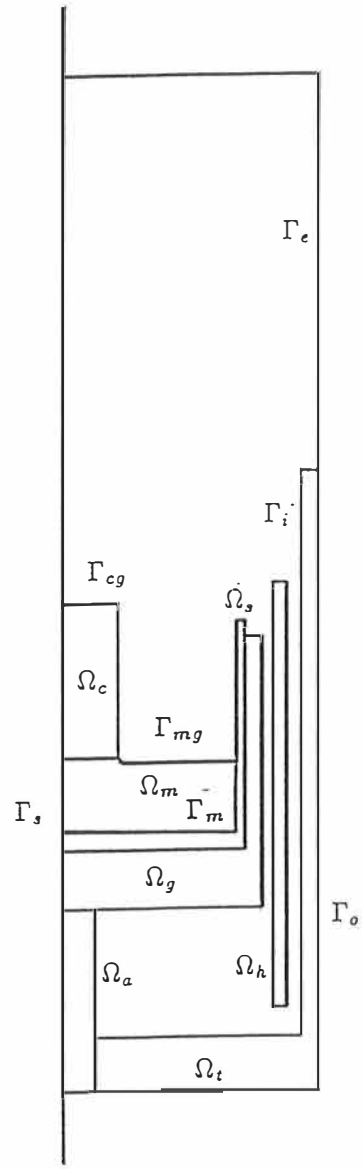

Figure 3.8 Axisymmetric Czochralski crystal growth geometry

emissive power and reflected irradiation, i.e.,

$$R = E + \rho J, \tag{3.28}$$

where ρ is the reflectivity. If the surface emissive power E is proportional to the corresponding value of a black body, and the Stefan-Boltzmann law and the assumption of the opaque, diffuse and gray surface are used, then

$$R = \sigma\epsilon T^4 + (1-\epsilon)J. \tag{3.29}$$

Here σ is the Stefan-Boltzmann constant and ϵ the emissivity of the surface.

Irradiation on Γ is proportional to radiation emitted by the different parts of Γ itself due to the equation

$$J(s) = \int_\Gamma \omega(s,z)\Xi(s,z)R(z)\ dz \tag{3.30}$$

for any $s \in \Gamma$. $\omega(s,z)$ is called a view factor and it has a form

$$\omega(s,z) = \frac{n_z \cdot (s-z) n_s \cdot (z-s)}{\pi |s-z|^4}, \tag{3.31}$$

where n_s and n_z are the surface normals directed to the vacuum. In (3.30) $\Xi(s,z)$ is a visibility factor and it has a value 1, if the points s and z see each others otherwise it has a value 0.

If we define an operator

$$K\lambda(s) = \int_\Gamma \omega(s,z)\Xi(s,z)\lambda(z)\ dz\ \ \forall s \in \Gamma,$$

we can write $J = KR$ and from (3.29) we get

$$R = \sigma\epsilon T^4 + (1-\epsilon)KR$$

or

$$R = (I - (1-\epsilon)K)^{-1}\sigma\epsilon T^4. \tag{3.32}$$

By substituting the definition of R in (3.32) into the equation of the heat balance (3.27) we arrive at

$$q = G(\sigma T^4), \tag{3.33}$$

where

$$G = (I-K)(I-(1-\epsilon)K)^{-1}\epsilon. \tag{3.34}$$

G can be also written in the form

$$G = (I - \epsilon K(I-(1-\epsilon)K)^{-1})\epsilon, \tag{3.35}$$

which is an infinite dimensional equivalent of so called Gebhart factors.

Let us then consider global heat transfer induced by conduction and convection containing the phase change between the crystal and melt. Outside of the crystal and melt, heat transfer is described by the heat equation

$$\rho_i c_{p_i} \frac{\partial T_i}{\partial t} - \frac{1}{r}\frac{\partial}{\partial r}\left(r\frac{\partial}{\partial r}k_i T_i\right) - \frac{\partial}{\partial z}\left(\frac{\partial}{\partial z}k_i T_i\right) = \rho_i h_i, \tag{3.36}$$

where the subscript i is associated with separate domains characterized by the material parameters ρ_i, c_{p_i} and k_i. The heat source h_i is nonzero only in the heater.

On the other hand, we have the enthalpy equation

$$\frac{\partial}{\partial t}H + \vec{u}\cdot\nabla H - \frac{1}{r}\frac{\partial}{\partial r}\left(r\frac{\partial}{\partial r}kT(H)\right) - \frac{\partial}{\partial z}\left(\frac{\partial}{\partial z}kT(H)\right) = 0 \tag{3.37}$$

in the crystal-melt system, where the functions H and $T(H)$ are as in (3.23) and (3.25). Thus in the whole system we have two separate equations (3.36) and (3.37) describing heat transfer with appropriate boundary conditions.

Remark 3.2 The enthalpy equation (3.37) offers a way to treat the phase change problem in the crystal-melt system. If we now make a standard definition $H = \rho_i c_{p_i} T_i$ in the heat equation (3.36) we get an equation of the type (3.37) for enthalpy in the whole domain. The equation is, however, not meaningful since enthalpy is discontinuous at the melt-silica crucible interface.

We proceed by modifying the definition of the enthalpy (equation (3.23)) so that it equals to temperature in the melt region. The definition can be rewritten in the form

$$H(T) = \begin{cases} \rho_c c_{p_c} T - \rho_c L + T_f(\rho_m c_{p_m} - \rho_c c_{p_c}), & T < T_f \\ [\rho_m c_{p_m} T_f - \rho_c L, \rho_m c_{p_m} T_f], & T = T_f \\ \rho_m c_{p_m} T, & T > T_f. \end{cases} \tag{3.38}$$

If we now define a function $\tilde{H} := H/\rho_m c_{p_m}$ we come to an expression (the density and heat capacity of the melt are constant)

$$\tilde{H}(T) = \begin{cases} \dfrac{\rho_c c_{p_c} T - \rho_c L + T_f(\rho_m c_{p_m} - \rho_c c_{p_c})}{\rho_m c_{p_m}}, & T < T_f \\ [T_f - \dfrac{\rho_c L}{\rho_m c_{p_m}}, T_f], & T = T_f \\ T, & T > T_f. \end{cases} \tag{3.39}$$

Temperature as a function of $\tilde{H}$ is correspondingly

$$(3.40)\quad T(\tilde{H}) = \begin{cases} \dfrac{\rho_m c_{p_m}\tilde{H} + \rho_c L - T_f(\rho_m c_{p_m} - \rho_c c_{p_c})}{\rho_c c_{p_c}}, & \tilde{H} < T_f - \dfrac{\rho_c L}{\rho_m c_{p_m}} \\ T_f, & \tilde{H} \in [T_f - \dfrac{\rho_c L}{\rho_m c_{p_m}}, T_f] \\ \tilde{H}, & \tilde{H} > T_f. \end{cases}$$

If we now divide the equation (3.36) by $\rho_i c_{p_i}$ and define $\tilde{H} = T$ we come to

$$(3.41)\qquad \frac{\partial}{\partial t}\tilde{H} + \vec{u}\cdot\nabla\tilde{H} - \frac{1}{r}\frac{\partial}{\partial r}\left(r\frac{\partial}{\partial r}\hat{k}T(\tilde{H})\right) - \frac{\partial}{\partial z}\left(\frac{\partial}{\partial z}\hat{k}T(\tilde{H})\right) = \hat{f}.$$

This equation has exactly the same form as in (3.37) and thus the enthalpy equation of the type (3.41) governs heat transfer in the whole system. The enthalpy $\tilde{H}$ in the crystal and melt is defined as in (3.39) and in the other parts as $\tilde{H} = T$. In the crystal and melt $\hat{f} = 0$ and $\hat{k} = k/\rho_m c_{p_m}$, where k depends on enthalpy. In the other parts $\hat{k} = k_i/\rho_i c_{p_i}$ and $\hat{f} = h_i/c_{p_i}$.

A mathematical model for the Czochralski crystal growth now reads: Find the velocity vector $\vec{u} = (u_r, u_z, u_\theta)$ and the pressure p in $\Omega_m \times (0, t_0)$ and the enthalpy $\tilde{H}$ in $\Omega \times (0, t_0)$, where $\Omega = \Omega_m \cup \Omega_c \cup \Omega_s \cup \Omega_g \cup \Omega_h \cup \Omega_a \cup \Omega_t$, such that (M5)

$$\begin{cases} \rho_m\dfrac{\partial u_r}{\partial t} - \dfrac{\partial \sigma_{zr}}{\partial z} - \dfrac{1}{r}\dfrac{\partial}{\partial r}(r\sigma_{rr}) + \dfrac{1}{r}\sigma_{\theta\theta} + \rho_m\left(u_r\dfrac{\partial u_r}{\partial r} + u_z\dfrac{\partial u_r}{\partial z} - \dfrac{u_\theta^2}{r}\right) = 0 \\ \rho_m\dfrac{\partial u_z}{\partial t} - \dfrac{\partial \sigma_{zz}}{\partial z} - \dfrac{1}{r}\dfrac{\partial}{\partial r}(r\sigma_{zr}) + \rho_m\left(u_r\dfrac{\partial u_z}{\partial r} + u_z\dfrac{\partial u_z}{\partial z}\right) = \\ \qquad = \rho_m g\beta(T - T_0) \\ \rho_m\dfrac{\partial u_\theta}{\partial t} - \dfrac{1}{r^2}\dfrac{\partial}{\partial r}(r^2\sigma_{r\theta}) - \dfrac{\partial \sigma_{\theta z}}{\partial z} + \rho_m\left(u_r\dfrac{\partial u_\theta}{\partial r} + u_z\dfrac{\partial u_\theta}{\partial z} + \dfrac{u_r u_\theta}{r}\right) = 0 \\ \dfrac{1}{r}\dfrac{\partial}{\partial r}(ru_r) + \dfrac{\partial u_z}{\partial z} = 0 \end{cases}$$

in $\Omega_m \times (0, t_0)$,

$$\frac{\partial}{\partial t}\tilde{H} + \vec{u}\cdot\nabla\tilde{H} - \frac{1}{r}\frac{\partial}{\partial r}\left(r\frac{\partial}{\partial r}\hat{k}T(\tilde{H})\right) - \frac{\partial}{\partial z}\left(\frac{\partial}{\partial z}\hat{k}T(\tilde{H})\right) = \hat{f}$$

in $\Omega \times (0, t_0)$ with the initial and boundary conditions

$$
\begin{cases}
\vec{u}(r,z,0) = \vec{u}^0(r,z) \quad \text{in } \Omega_m \cup \Omega_c \\
\tilde{H}(r,z,0) = \tilde{H}^0(r,z) \quad \text{in } \Omega \\
u_r = 0, \ \dfrac{\partial u_z}{\partial r} = 0, \ u_\theta = 0 \quad \text{on } (\Gamma_s \cap \Omega_m) \times (0,t_0) \\
\dfrac{\partial T(\tilde{H})}{\partial r} = 0 \quad \text{on } (\Gamma_s \cap \Omega) \times (0,t_0) \\
u_r = 0, \ u_z = 0, \ u_\theta = \omega_m r \quad \text{on } \Gamma_m \times (0,t_0) \\
\vec{u} \cdot \vec{n} = 0, \ \sigma_n = \dfrac{\gamma_0}{R} - p_a, \ \sigma_\tau = -\vartheta \gamma_0 \dfrac{\partial T(\tilde{H})}{\partial \tau} \quad \text{on } \Gamma_{mg} \times (0,t_0) \\
u_r = 0, \ u_z = 0, \ u_\theta = \omega_c r \quad \text{on } \Sigma \times (0,t_0), \\
\rho_m \vec{u}_m \cdot \vec{n}_\Sigma - \rho_c \vec{u}_c \cdot \vec{n}_\Sigma = (\rho_m - \rho_c) \vec{u}_\Sigma \cdot \vec{n}_\Sigma \quad \text{on } \Sigma \times (0,t_0) \\
-\hat{k} \dfrac{\partial T(\tilde{H})}{\partial n} = G(\hat{\sigma}(T(\tilde{H}))^4) \quad \text{on } (\Gamma_{mg} \cup \Gamma_{cg} \cup \Gamma_i) \times (0,t_0) \\
-\hat{k} \dfrac{\partial T(\tilde{H})}{\partial n} = \hat{\alpha}(T(\tilde{H}) - T_{ext}) \quad \text{on } \Gamma_o \times (0,t_0) \\
\tilde{H} = \tilde{H}_e \quad \text{on } \Gamma_e \times (0,t_0).
\end{cases}
$$

Remark 3.3 A division of the heat equation (3.36) by $\rho_i c_{p_i}$ leads to a scaling of the boundary conditions for $T(\tilde{H})$. We denote the scaled heat transfer coefficient and the Stefan-Boltzmann coefficient by $\hat{\alpha} = \alpha / \rho_i c_{p_i}$ and $\hat{\sigma} = \sigma / \rho_i c_{p_i}$, respectively, where ρ_i and c_{p_i} are characterized by each material.

4. Simulation of Thermally Coupled Liquid Flows

In this chapter we shall solve numerically the mathematical models (M1)-(M3) presented in the previous chapter by the finite element method. Variational formulations and Petrov-Galerkin finite element discretizations of the models are derived in Chapters 4.1 and 4.2. In Chapter 4.3 the treatment of nonlinearities in the mathematical models is discussed. Numerical simulations of the models (M1) and (M2) are carried out in simple two dimensional geometries while the model (M3) is simulated numerically in axisymmetric geometry. Numerical results based on the two dimensional computations are compared in Chapters 4.4.1 and 4.4.2 to the results presented in [Argyris92] and [Cuvelier86]. In Chapter 4.4.3 we show numerical results of the silicon melt flow in the axisymmetric crucible.

4.1 Variational Formulations

We shall consider in Chapter 4.1.1 a time dependent variant of the model (M1) and derive variational formulations for the Navier-Stokes and heat equations. The reason for this is that the time dependent variant covers with some exceptions both of the mathematical models (M1) and (M2). In Chapter 4.1.2 we focus on the model (M3) and derive variational formulations for the cylindrically symmetric Navier-Stokes equations and the axisymmetric heat equation.

The variational formulations of the Navier-Stokes and heat equations are based on the references [Cuvelier86b], [Girault86], [Křižek90], [Long-An86] and [Temam84]. In these references a number of results concerned with functional spaces associated with variational formulations of the Navier-Stokes and heat equations as well as results on existence and uniqueness are derived. For the choice of test function spaces we refer to the spaces introduced in the references above.

4.1.1 Time Dependent Variant of Model (M1)

Let us assume that the solution u_k of the transient momentum equation in the modified (M1) is smooth enough (at least two times continuously differentiable) in $\Omega \times (0, t_0)$ and the boundary $\partial\Omega$ is Lipschitzian ([Křižek90]). We define the Sobolev space $H^m(\Omega)$ by

$$H^m(\Omega) = \left\{ v \in L^2(\Omega) | D^i v \in L^2(\Omega) \text{ for all i such that } |i| \leq m \right\},$$

where $L^2(\Omega)$ is a space of square integrable functions, i a multi-index and $D^i v$ the ith generalized partial derivative of the function v.

The variational formulation for the momentum equation is obtained by multiplying the momentum equation by a test function $v_k \in H^1(\Omega)$, integrating over the domain $\Omega \subset \mathbb{R}^2$ and applying Green's theorem. Then we arrive at

$$\begin{aligned}(4.9)\qquad &\int_\Omega \rho_0 \frac{\partial u_k}{\partial t} v_k \, d\Omega + \int_\Omega 2\mu \vec{\varepsilon}_k \cdot \nabla v_k \, d\Omega + \int_\Omega \rho_0 (\vec{u} \cdot \nabla u_k) v_k \, d\Omega - \\ &- \int_\Omega p \frac{\partial v_k}{\partial x_k} \, d\Omega - \int_{\partial\Omega} [2\mu \vec{\varepsilon}_k \cdot \vec{n} - p n_k] \, v_k \, dS = - \int_\Omega \rho_0 g_k \beta (T - T_0) v_k \, d\Omega\end{aligned}$$

for all $v_k \in H^1(\Omega)$, $k = 1, 2$, where $\vec{\varepsilon}_k = (\varepsilon_{k1}, \varepsilon_{k2})$ and $\vec{n}$ is the outward unit normal vector.

The boundary $\partial\Omega$ consisted of mutually disjoint and open parts such that $\partial\Omega = \Gamma_0 \cup \Gamma_1 \cup \Gamma_2 \cup \Gamma_3$. By assuming that the test function $\vec{v} = (v_1, v_2)$ satisfies the conditions $\vec{v} \cdot \vec{n} = 0$ on Γ_0 and $\vec{v} = 0$ on $\Gamma_1 \cup \Gamma_2 \cup \Gamma_3$ and by applying the boundary conditions listed in (M1) we come to

$$\begin{aligned}(4.10)\qquad &\int_\Omega \rho_0 \frac{\partial u_k}{\partial t} v_k \, d\Omega + \int_\Omega 2\mu \vec{\varepsilon}_k \cdot \nabla v_k \, d\Omega + \int_\Omega \rho_0 (\vec{u} \cdot \nabla u_k) v_k \, d\Omega - \\ &- \int_\Omega p \frac{\partial v_k}{\partial x_k} \, d\Omega = - \int_\Omega \rho_0 g_k \beta (T - T_0) v_k \, d\Omega - \int_{\Gamma_0} \vartheta \gamma_0 \frac{\partial T}{\partial \tau} v_k \tau_k \, dS,\end{aligned}$$

where $\vec{\tau}$ is the unit tangent vector.

Besides the velocity components u_k, $k = 1, 2$, the pressure is also unknown in the variational formulation (4.10). In order to consider the pressure we can apply for instance integrated method, [Cuvelier86]. In this method the variational formulation is formed also for the continuity equation $\nabla \cdot \vec{u} = 0$. Another approach, which we use here, is a penalty function method, [Cuvelier86], [Temam84]. In this method the continuity equation is perturbed with a small parameter ε (called penalty parameter) times the pressure:

$$(4.11)\qquad \varepsilon p + \nabla \cdot \vec{u} = 0.$$

This means that we allow a slight numerical compressibility. Substituting now the pressure from the equation (4.11) into the variational formulation (4.10) we get finally the variational formulation for u_k, $k = 1, 2$,

$$\begin{aligned}(4.12)\qquad &\int_\Omega \rho_0 \frac{\partial u_k}{\partial t} v_k \, d\Omega + \int_\Omega 2\mu \vec{\varepsilon}_k \cdot \nabla v_k \, d\Omega + \int_\Omega \rho_0 (\vec{u} \cdot \nabla u_k) v_k \, d\Omega + \\ &+ \frac{1}{\varepsilon} \int_\Omega (\nabla \cdot \vec{u}) \frac{\partial v_k}{\partial x_k} \, d\Omega = - \int_\Omega \rho_0 g_k \beta (T - T_0) v_k \, d\Omega - \int_{\Gamma_0} \vartheta \gamma_0 \frac{\partial T}{\partial \tau} v_k \tau_k \, dS.\end{aligned}$$

If we neglect the integral containing the time derivative, we get a variational formulation which is exactly the same one derives for the momentum equations in

(M1). By assuming $\vec{v} = 0$ on Γ_0 the boundary integral disappears and we come to an appropriate variational formulation for (M2).

The pressure can solved after the velocity field is computed. From (4.11) it follows that

$$\int_\Omega p \, d\Omega = -\frac{1}{\varepsilon} \int_\Omega \nabla \cdot \vec{u} \, d\Omega.$$

The final form of the variational formulation for the time dependent and two dimensional heat equation, by taking into account the boundary conditions for the temperature in (M1) and by assuming for the test function $v = 0$ on $\Gamma_1 \cup \Gamma_2 \cup \Gamma_3$, is simply

$$\int_\Omega \rho_0 c_p \frac{\partial T}{\partial t} v \, d\Omega + \int_\Omega \rho_0 c_p (\vec{u} \cdot \nabla T) v \, d\Omega + \int_\Omega k \nabla T \cdot \nabla v \, d\Omega = 0. \tag{4.13}$$

Again, if we neglect the first integral containing the time derivative, we obtain an appropriate variational formulation for (M1). The variational formulation (4.13), as it stands, is valid for (M2).

4.1.2 Model (M3)

Next we shall derive variational formulations for the equations of the velocity components u_r, u_z and u_θ in (M3). Since the derivations are congruent with the variational formulation derived in the two dimensional case, we outline only the main points. We assume that the melt-gas interface is a straight line, i.e., it is not considered as a free boundary. Therefore we neglect the boundary condition $\sigma_n = \frac{\gamma_0}{R} - p_a$ on Γ_{mg}.

Let the test functions v_r, v_z and $v_\theta \in H_r^1(\Omega_m) = \{v \in L_r^2(\Omega_m) | \frac{\partial v}{\partial r}, \frac{\partial v}{\partial z} \in L_r^2(\Omega_m)\}$, where $L_r^2(\Omega_m)$ is the space of square integrable functions weighted by r in Ω_m. In the following we assume $\vec{v} \cdot \vec{n} = 0$ on Γ_{mg}. The multiplication of the momentum equation of u_r by the test function v_r, the observation of the weight r, the integration over the melt region Ω_m and Green's theorem produce

$$\begin{aligned} &\int_{\Omega_m} \rho_m \frac{\partial u_r}{\partial t} v_r r \, d\Omega_m + \int_{\Omega_m} \sigma_{zr} \frac{\partial v_r}{\partial z} r \, d\Omega_m + \int_{\Omega_m} \sigma_{rr} \frac{\partial v_r}{\partial r} r \, d\Omega_m + \\ &+ \int_{\Omega_m} \frac{1}{r} \sigma_{\theta\theta} v_r r \, d\Omega_m + \int_{\Omega_m} \rho_m (\vec{u} \cdot \nabla u_r) v_r r \, d\Omega_m - \int_{\Omega_m} \rho_m \frac{1}{r} u_\theta^2 v_r r \, d\Omega_m - \\ &- \int_{\Gamma_{mg}} (\sigma_{zr} n_z) v_r r \, dS - \int_{\Gamma_{mg}} (\sigma_{rr} n_r) v_r r \, dS = 0. \end{aligned} \tag{4.14}$$

Here we have assumed that the test function v_r satisfies the condition $v_r = 0$ on the wall Γ_m. If we use the penalty method for the pressure, i.e., we perturbe the

continuity equation as

$$p = -\frac{1}{\varepsilon}\left(\frac{\partial u_r}{\partial r} + \frac{u_r}{r} + \frac{\partial u_z}{\partial z}\right), \tag{4.15}$$

substitute the components of the stress tensor (equations (3.14a-f)) and the pressure from the equation (4.15) into the equation (4.14) and apply the boundary conditions we come to

(4.16)

$$\begin{aligned}
&\int_{\Omega_m} \rho_m \frac{\partial u_r}{\partial t} v_r r \, d\Omega_m + \int_{\Omega_m} 2\mu_m \frac{\partial u_r}{\partial r}\frac{\partial v_r}{\partial r} r \, d\Omega_m + \int_{\Omega_m} \mu_m \frac{\partial u_r}{\partial z}\frac{\partial v_r}{\partial z} r \, d\Omega_m + \\
&+ \int_{\Omega_m} \mu_m \frac{\partial u_z}{\partial r}\frac{\partial v_r}{\partial z} r \, d\Omega_m + \int_{\Omega_m} 2\mu_m \frac{u_r}{r^2} v_r r \, d\Omega_m + \\
&+ \int_{\Omega_m} \rho_m (\vec{u}\cdot\nabla u_r) v_r r \, d\Omega_m - \int_{\Omega_m} \rho_m \frac{1}{r} u_\theta^2 v_r r \, d\Omega_m + \\
&+ \frac{1}{\varepsilon}\int_{\Omega_m} \left(\frac{\partial u_r}{\partial r} + \frac{u_r}{r} + \frac{\partial u_z}{\partial z}\right)\frac{\partial v_r}{\partial r} r \, d\Omega_m + \frac{1}{\varepsilon}\int_{\Omega_m} \frac{1}{r}\left(\frac{\partial u_r}{\partial r} + \frac{u_r}{r} + \frac{\partial u_z}{\partial z}\right) v_r r \, d\Omega_m = \\
&= -\int_{\Gamma_{mg}} \vartheta\gamma_0 \frac{\partial T}{\partial \tau} v_r \tau_r r \, dS.
\end{aligned}$$

In the same manner we obtain variational formulations for the velocity components u_z and u_θ:

(4.17)

$$\begin{aligned}
&\int_{\Omega_m} \rho_m \frac{\partial u_z}{\partial t} v_z r \, d\Omega_m + \int_{\Omega_m} 2\mu_m \frac{\partial u_z}{\partial z}\frac{\partial v_z}{\partial z} r \, d\Omega_m + \int_{\Omega_m} \mu_m \frac{\partial u_z}{\partial r}\frac{\partial v_z}{\partial r} r \, d\Omega_m + \\
&+ \int_{\Omega_m} \mu_m \frac{\partial u_r}{\partial z}\frac{\partial v_z}{\partial r} r \, d\Omega_m + \int_{\Omega_m} \rho_m (\vec{u}\cdot\nabla u_z) v_z r \, d\Omega_m + \\
&+ \frac{1}{\varepsilon}\int_{\Omega_m} \left(\frac{\partial u_r}{\partial r} + \frac{u_r}{r} + \frac{\partial u_z}{\partial z}\right)\frac{\partial v_z}{\partial z} r \, d\Omega_m = \\
&= \int_{\Omega_m} \rho_m g\beta(T - T_0) v_z r \, d\Omega_m - \int_{\Gamma_{mg}} \vartheta\gamma_0 \frac{\partial T}{\partial \tau} v_z \tau_z r \, dS,
\end{aligned}$$

$$\begin{aligned}
&\int_{\Omega_m} \rho_m \frac{\partial u_\theta}{\partial t} v_\theta r \, d\Omega_m + \int_{\Omega_m} \mu_m \left(\frac{\partial u_\theta}{\partial r} - \frac{u_\theta}{r}\right)\left(\frac{\partial v_\theta}{\partial r} - \frac{v_\theta}{r}\right) r \, d\Omega_m + \\
&+ \int_{\Omega_m} \mu_m \frac{\partial u_\theta}{\partial z}\frac{\partial v_\theta}{\partial z} r \, d\Omega_m + \int_{\Omega_m} \rho_m (\vec{u}\cdot\nabla u_\theta) v_\theta r \, d\Omega_m + \\
&+ \int_{\Omega_m} \rho_m \frac{1}{r} u_r u_\theta v_\theta r \, d\Omega_m = 0.
\end{aligned} \tag{4.18}$$

The variational formulation for the time dependent heat equation in (M3), if we take into account the Robin boundary condition on Γ_{mg} and assume that for the

test function holds $v = 0$ in Γ_m, is

(4.19)
$$\int_\Omega \rho_m c_{pm} \frac{\partial T}{\partial t} vr \; d\Omega + \int_\Omega \rho_m c_{pm} (\vec{u} \cdot \nabla T) vr \; d\Omega + \int_\Omega k_m \left(\nabla T \cdot \nabla v\right) r \; d\Omega + \\ + \int_{\Gamma_{mg}} \alpha T vr \; dS = \int_{\Gamma_{mg}} \alpha T_{ext} vr \; dS.$$

4.2 Petrov-Galerkin Finite Element Approximation

In connection with the variational formulations one considers infinite dimensional test function spaces. The spaces have countable bases, i.e., any function can be expressed as an infinite linear combination of the test functions. In the finite element approximation one considers a finite dimensional subspace spanned by n basis functions $\varphi_1, \varphi_2, ..., \varphi_n$, where n is the dimension of the subspace. Now the test functions are chosen from the subspace and the velocity and the temperature are approximated as linear combinations of the basis functions:

(4.20a)
$$u_k = \sum_{j=1}^{n} u_{kj} \varphi_j,$$

(4.20b)
$$T = \sum_{j=1}^{n} T_j \varphi_j,$$

where $k = 1, 2, r, z, \theta$ and u_{kj} and $T_j \in \mathbb{R}$ are the values of the velocity and the temperature depending on time t.

If we substitute the linear combinations of the velocity and temperature to the variational formulations (4.12) and (4.13) (or (4.16)-(4.19)) and replace the test functions with the basis functions φ_i we come to the standard Galerkin method. It is well known, however, that for highly convective transport problems difficulties in numerical solutions are encountered with this method, [Argyris92], [Brooks82], [Johnson84]. In order to prevent spurious node-to-node oscillations severe mesh refinement is required. Another alternative is to apply stabilized methods, see [Franca92a], [Franca92b] and [Franca93].

Stabilized methods for the advective model were first introduced by Hughes and Brooks and referred to as the streamline upwinding/Petrov-Galerkin methods. After that Johnson and Nävert made a convergence analysis for this method. This analysis was an important first step to establish various extensions to other computational fluid dynamics applications. These methods are referred by Johnson and his co-workers as streamline diffusion methods. Since then stabilized methods have been developed for instance by Franca and Frey.

In this work we apply the streamline upwinding/Petrov-Galerkin technique proposed in [Brooks82]. The standard Galerkin basis functions are modified by adding

a streamline upwind perturbation acting only in the direction of flow. The modified basis functions have the form

$$\hat{\varphi}_i = \varphi_i + \tilde{k}\frac{1}{\|\vec{u}\|^2}\vec{u}\cdot\nabla\varphi_i,$$

where the coefficient $\tilde{k}$ is specified as a function of velocity, physical parameters and element dimensions. Compared to the standard Galerkin method the streamline upwinding/Petrov-Galerkin technique yields a considerable improvement of stability, [Brooks82], [Argyris92]. Although the idea of Brooks and Hughes is rather old and modifications to the definition of the parameter $\tilde{k}$ have been made ([Franca92a]), this technique has shown its ability to handle convection dominated problems.

All test functions appeared in the variational formulations presented in the previous chapter should in principle be replaced with the modified basis functions. However, according to [Brooks82] the Galerkin basis functions can be used in those terms, which originate from the diffusion, pressure and stress divergence parts, if the following holds: i) heat conductivity is isotropic, ii) temperature and velocity are interpolated by bilinear basis functions, iii) pressure is interpolated by piecewise constant functions, iv) elements are rectangular and v) flow is incompressible.

In this work we assume that the material parameters are constant (in this case the heat conductivity is naturally isotropic). We use bilinear basis functions for the velocity and the temperature. The pressure is piecewise constant in each element. (Actually we approximate the pressure with bilinear basis functions but use a reduced integration, i.e., the pressure terms are integrated by using 1-point Gaussian integration rule). Our finite element meshes are composed of quadrilateral elements. Thus the conditions i)-iv) are satisfied. The penalty function method satisfies the condition v) only approximately.

In two dimensional case the application of the streamline-upwinding/Petrov-Galerkin method produces an algebraic system for u_1, u_2 and T:

$$\begin{aligned} M^u\frac{\partial u_1}{\partial t} + A_{11}u_1 + A_{12}u_2 &= -F_1^u - G_1^u + D_1^u, \\ M^u\frac{\partial u_2}{\partial t} + A_{21}u_1 + A_{22}u_2 &= -F_2^u - G_2^u + D_2^u, \\ M^T\frac{\partial T}{\partial t} + AT &= D^T, \end{aligned} \tag{4.21}$$

where

$$\begin{aligned} A_{11} &= 2K_{11}^u + K_{22}^u + C^u + P_{11}, \\ A_{12} &= K_{12}^u + P_{12}, \\ A_{21} &= K_{21}^u + P_{21}, \\ A_{22} &= 2K_{22}^u + K_{11}^u + C^u + P_{22}, \\ A &= C^T + K^T. \end{aligned} \tag{4.22}$$

The sub-matrices and vectors for the velocity in (4.22) are

$$
\begin{aligned}
M^u(i,j) &= \int_\Omega \rho_0 \hat{\varphi}_i \varphi_j \, d\Omega, \\
K^u_{\alpha\beta}(i,j) &= \int_\Omega \mu \frac{\partial \varphi_i}{\partial x_\beta} \frac{\partial \varphi_j}{\partial x_\alpha} \, d\Omega, \\
C^u(i,j) &= \int_\Omega \rho_0 \hat{\varphi}_i \, (\vec{u} \cdot \nabla \varphi_j) \, d\Omega, \\
P_{\alpha\beta}(i,j) &= \frac{1}{\varepsilon} \int_\Omega \frac{\partial \varphi_i}{\partial x_\alpha} \frac{\partial \varphi_j}{\partial x_\beta} \, d\Omega, \\
F^u_k(i) &= \int_\Omega \rho_0 g_k \beta (T - T_0) \hat{\varphi}_i \, d\Omega, \\
G_k(i) &= \int_{\Gamma_0} \vartheta \gamma_0 \frac{\partial T}{\partial \tau} \varphi_i \tau_k \, dS,
\end{aligned}
\tag{4.23}
$$

$i, j = 1, ..., n$. For the temperature we have

$$
\begin{aligned}
M^T(i,j) &= \int_\Omega \rho_0 c_p \hat{\varphi}_i \varphi_j \omega \, d\Omega, \\
C^T(i,j) &= \int_\Omega \rho_0 c_p \hat{\varphi}_i \, (\vec{u} \cdot \nabla \varphi_j) \, \omega \, d\Omega, \\
K^T(i,j) &= \int_\Omega k \, (\nabla \varphi_i \cdot \nabla \varphi_j) \, \omega \, d\Omega,
\end{aligned}
\tag{4.24}
$$

$i, j = 1, ..., n$. The sub-matrices for the temperature include the weight ω which is equal to one in two dimensional case. The vectors D^u_1, D^u_2 and D^T consist of the Dirichlet data.

Substitution of the linear combination of the velocity (4.20a) to the variational formulations (4.16)-(4.18) and the linear combination of the temperature (4.20b) to the variational formulation (4.19) produce the following algebraic system for u_r, u_z, u_θ and T in axisymmetric geometry:

$$
\begin{aligned}
M^u \frac{\partial u_r}{\partial t} + A_{rr} u_r + A_{rz} u_z + A_{r\theta} u_\theta &= -G^u_r + D^u_r, \\
M^u \frac{\partial u_z}{\partial t} + A_{zr} u_r + A_{zz} u_z &= F^u - G^u_z + D^u_z, \\
M^u \frac{\partial u_\theta}{\partial t} + A_{\theta r} u_r + A_{\theta z} u_z + A_{\theta\theta} u_\theta &= D^u_\theta, \\
M^T \frac{\partial T}{\partial t} + AT &= F^T + D^T,
\end{aligned}
\tag{4.25}
$$

where

$$
\begin{aligned}
A_{rr} &= 2K^u_{rr} + K^u_{zz} + 2L + C^u + P_{rr} + Q_{rr},\\
A_{rz} &= K^u_{rz} + P_{rz} + Q_{rz},\\
A_{r\theta} &= -N_\theta,\\
A_{zr} &= K^u_{zr} + P_{zr} + Q_{zr},\\
A_{zz} &= 2K^u_{zz} + K^u_{rr} + C^u + P_{zz},\\
A_{\theta r} &= N_r,\\
A_{\theta z} &= 0,\\
A_{\theta\theta} &= K^u_{rr} + K^u_{zz} - (E + E^T) + L + C^u,\\
A &= C^T + K^T + B^T.
\end{aligned}
\tag{4.26}
$$

By taking into account the above discussion concerning the appearance of the modified and Galerkin basis functions the sub-matrices and vectors are

$$
\begin{aligned}
M^u(i,j) &= \int_{\Omega_m} \rho_m \hat{\varphi}_i \varphi_j r \, d\Omega,\\
K^u_{st}(i,j) &= \int_{\Omega_m} \mu_m \frac{\partial \varphi_i}{\partial t}\frac{\partial \varphi_j}{\partial s} r \, d\Omega,\\
C^u(i,j) &= \int_{\Omega_m} \rho_m \hat{\varphi}_i \left(\vec{u}\cdot\nabla\varphi_j\right) r \, d\Omega_m,\\
P_{st}(i,j) &= \frac{1}{\varepsilon}\int_{\Omega_m} \frac{\partial \varphi_i}{\partial s}\frac{\partial \varphi_j}{\partial t} r \, d\Omega,\\
L(i,j) &= \int_{\Omega_m} \mu_m \frac{1}{r^2}\varphi_i\varphi_j r \, d\Omega_m,\\
Q_{rr}(i,j) &= \frac{1}{\varepsilon}\int_{\Omega_m} \left[\frac{1}{r}\frac{\partial \varphi_i}{\partial r}\varphi_j + \frac{1}{r}\varphi_i\frac{\partial \varphi_j}{\partial r} + \frac{1}{r^2}\varphi_i\varphi_j\right] r \, d\Omega_m,\\
Q_{rz}(i,j) &= \frac{1}{\varepsilon}\int_{\Omega_m} \frac{1}{r}\varphi_i\frac{\partial \varphi_j}{\partial z} r \, d\Omega_m,\\
Q_{zr}(i,j) &= \frac{1}{\varepsilon}\int_{\Omega_m} \frac{1}{r}\varphi_j\frac{\partial \varphi_i}{\partial z} r \, d\Omega_m,
\end{aligned}
\tag{4.27}
$$

$$N_s(i,j) = \int_{\Omega_m} \rho_m \frac{1}{r} u_s \hat{\varphi}_i \varphi_j r \; d\Omega_m,$$

$$E(i,j) = \int_{\Omega_m} \mu_m \frac{1}{r} \varphi_j \frac{\partial \varphi_i}{\partial r} r \; d\Omega_m,$$

$$F^u(i) = \int_{\Omega_m} \rho g \beta (T - T_0) \hat{\varphi}_i r \; d\Omega_m,$$

$$G_s^u(i) = \int_{\Gamma_{mg}} \vartheta \gamma_0 \frac{\partial T}{\partial \tau} \varphi_i \tau_s r \; dS,$$

$$B^T(i,j) = \int_{\Gamma_{mg}} \alpha \varphi_i \varphi_j r \; dS,$$

$$F^T(i) = \int_{\Gamma_{mg}} \alpha T_{ext} \varphi_i r \; dS,$$

$i, j = 1, ..., n.$

The matrices M^T, C^T and K^T are as in (4.24) where the weight ω is now equal to r. In (4.25) the vectors D_r^u, D_z^u, D_θ^u and D^T contain the Dirichlet data.

Remark 4.1 The matrix E^T is not connected with the temperature, but it is a transpose of the matrix E.

Remark 4.2 The integrals appearing in (4.23), (4.24) and (4.27) are approximated by using a 2×2 Gaussian integration rule in a local isoparametric $[-1,1] \times [-1,1]$ element. As we mentioned above, the penalty terms are approximated by using a reduced integration, i.e., only one point Gaussian integration rule is applied.

Remark 4.3 In the discretization of the Navier-Stokes equations we use the bilinear velocity-constant pressure approximation. It is well known that this combination does not satisfy the Ladyzhenskaya-Babuška-Brezzi (LBB) condition, and spurious oscillations in the pressure field can occur (checkerboard pressure patterns). One can still obtain good velocity fields. In the connection with the numerical simulations of silicon melt flow and crystal growth from silicon melt we study, if the checkerboard pressure patterns really appear.

4.3 Linearization of Coupled Navier-Stokes and Heat Equations

The Navier-Stokes and heat equations which govern thermally coupled liquid flows are nonlinear on two levels. First, the velocity field depends on the temperature distribution and vice versa. Secondly, the Navier-Stokes equations are nonlinear throughout the convection term $(\vec{u} \cdot \nabla)\vec{u}$ and some additional terms in the equations of the velocity components u_r and u_θ in the cylindrically symmetric case.

The nonlinearity can be handled in two ways. Discretization of the nonlinear equa-

tions leads to a nonlinear algebraic system for the velocity and the temperature

$$\begin{cases} A(\vec{u})\vec{u} = F(T) \\ B(\vec{u})T = G, \end{cases} \tag{4.28}$$

which can be solved by using iterative methods. Another approach is to linearize the coupled and nonlinear equations. In this work we apply the uncoupling of the Navier-Stokes equations and the heat equation, i.e., we solve two separate discrete algebraic systems

$$\begin{cases} A(\vec{u})\vec{u} = F(T^*) \\ B(\vec{u}^*)T = G, \end{cases} \tag{4.29}$$

where the variables $\vec{u}^*$ and T^* are known.

The discretized and nonlinear algebraic system for the Navier-Stokes equations in (4.29) can be solved iteratively. The nonlinear terms can also be handled, for instance, by the method of characteristics, [Pironneau82], [Hilpert91] or by linearizing the nonlinear terms, [Cuvelier86b]. In this work the linearization technique is applied.

The linearization of the Navier-Stokes equations generates a sequence of linear matrix equations for the velocity

$$A(\vec{u}^{n-1})\vec{u}^n = F(T^*), \quad n = 1, 2, 3, ... \tag{4.30}$$

The matrix equation (4.30) is then iterated until convergence is attained.

The nonlinear term $(\vec{u}\cdot\nabla)\vec{u}$ can be linearized by using for instance a Picard iteration (also called successive substitution) or a Newton linearization, [Cuvelier86b]. The Picard iteration produces a first order linearization with respect to the rate of convergence, while with the Newton linearization we obtain a convergence rate of second order.

Let us assume that the solution of the equation (4.30) at a new iteration level can be described as a sum of the solution from the previous iteration level and a correction

$$\vec{u}^n = \vec{u}^{n-1} + \delta\vec{u}^{n-1}, \tag{4.31}$$

where the correction δ decreases when the number of the iteration level n increases. Three different variants of the Picard type linearization are obtained when we rewrite the convection term $(\vec{u}\cdot\nabla)\vec{u}$ with the help of the equation (4.31). Namely

$$(\vec{u}^n\cdot\nabla)\vec{u}^n = (\vec{u}^{n-1}\cdot\nabla)\vec{u}^{n-1} + \mathcal{O}(\delta), \tag{4.32a}$$

$$(\vec{u}^n\cdot\nabla)\vec{u}^n = (\vec{u}^n\cdot\nabla)\vec{u}^{n-1} + \mathcal{O}(\delta), \tag{4.32b}$$

$$(\vec{u}^n\cdot\nabla)\vec{u}^n = (\vec{u}^{n-1}\cdot\nabla)\vec{u}^n + \mathcal{O}(\delta). \tag{4.32c}$$

Numerical tests have shown that the convergence region of the schemes (4.32a) and (4.32b) are quite modest. The scheme (4.32c) is superior to the previous ones in the sense of the convergence region and the convergence rate.

Although the convergence region of the scheme (4.32c) is relatively large, the convergence rate is only linear. The Newton linearization, however,

$$(\vec{u}^n \cdot \nabla)\vec{u}^n = (\vec{u}^{n-1} \cdot \nabla)\vec{u}^n + (\vec{u}^n \cdot \nabla)\vec{u}^{n-1} - (\vec{u}^{n-1} \cdot \nabla)\vec{u}^{n-1} + \mathcal{O}(\delta^2) \tag{4.33}$$

yields a quadratic convergence rate, but requires a good initial guess. An adequate initial guess is usually obtained from the Picard iteration.

Above we have considered the linearization techniques for the nonlinear convection term $(\vec{u} \cdot \nabla)\vec{u}$. The linearization of the other nonlinear terms with the Picard iteration or the Newton linearization is analogous.

4.4 Numerical Examples

4.4.1 Grashof and Marangoni Convections in 2D

We solve numerically the mathematical model (M1) introduced in Chapter 3.1.1 and compare the numerical results to those presented in [Cuvelier86]. We use the results of the two dimensional finite element analysis derived in the previous chapters. In the steady state case we have a discrete problem for the velocity and the temperature

$$\begin{aligned} A_{11}u_1 + A_{12}u_2 &= -F_1^u - G_1^u + D_1^u, \\ A_{21}u_1 + A_{22}u_2 &= -F_2^u - G_2^u + D_2^u, \\ AT &= D^T, \end{aligned} \tag{4.34}$$

where the sub-matrices and vectors are introduced in (4.22)-(4.24).

In [Cuvelier86] the problem is solved by using the finite element method. Either coupled or uncoupled method for the velocity, pressure and temperature is applied. The nonlinearities are solved by the Newton-Raphson iteration. The domain ($L = 1$) is divided into regular triangles and triangulation corresponds to a space discretization of $\Delta x_1 = \Delta x_2 = 0.05$. The number of triangular elements is equal to 200. For velocity continuous piecewise extended quadratic basis functions together with piecewise linear non-continuous basis functions for the pressure has been chosen. Quadratic polynomial approximation is applied for the temperature.

We solve the problem by uncoupling the discretized Navier-Stokes and heat equations. The nonlinearity in the Navier-Stokes equations is solved by the Newton

linearization technique. We divide the domain into 20×20 quadrilateral elements, i.e., $\Delta x_1 = \Delta x_2 = 0.05$. We apply bilinear basis functions for the velocity and the temperature. Pressure is eliminated by the penalty method. The penalty method produces the sub-matrices $P_{\alpha\beta}$ in the matrix equations (4.21)- (4.23). These sub-matrices are integrated numerically by using the reduced integration. The linear matrix equations for the velocity and the temperature in (4.34) are solved by the Gaussian elimination. The Navier-Stokes iteration is terminated when the relative error $\|u^k - u^{k-1}\|/\|u^k\|$ is less than 10^{-5}. Here the superscripts k and $k-1$ refer to consecutive Navier-Stokes iterations. The iteration between the uncoupled Navier-Stokes and heat equations is terminated when the relative error $\|u^k - u^{k-1}\|/\|u^k\|$ is also less than 10^{-5}. Now the superscripts k and $k-1$ refer to consecutive uncoupling iteration steps.

In all numerical examples we use dimensionless parameters as in [Cuvelier86] and [Cuvelier86b]. The Reynolds, Grashof, Prandtl and Marangoni numbers are the following:

$$Re = \frac{LU\rho_0}{\mu},$$

$$Gr = \frac{\beta g \rho_0^2 L^3 \Delta T}{\mu^2},$$

$$Pr = \frac{c_p \mu}{k},$$

$$Ma = \frac{\vartheta \gamma_0 c_p \rho_0 L \Delta T}{\mu k},$$

where L and U are the characteristic length and velocity, respectively, and $\Delta T'$ describes the temperature difference between the boundaries Γ_1 and Γ_3. The Prandtl number is fixed to 0.73. The Reynolds number is assumed to be equal to unity and gravity is assumed to act in the direction of the negative x_2-axis.

Let us consider the Grashof convection first. In Figures 4.2a-4.4b the temperature isotherms and the velocity vectors for $Pr = 0.73$, $Ma = 0$ and the various Grashof numbers are presented.

The Grashof number represents the relative importance between buoyancy and viscous forces. Since gravity acts in the direction of the negative x_2-axis the buoyancy force appears in the equation of u_2, where we have $\ldots = \rho_0 g \beta (T - T_0)$. Temperature in the neighborhood of the left-hand vertical boundary is greater than T_0. For this reason the buoyancy force is positive and the flow direction in the near of this boundary is upwards. Correspondingly, the buoyancy force in the neighborhood of the right-hand vertical boundary is negative and the flow direction is downwards.

With the low Grashof number ($Gr = 2.0$) the temperature isotherms behave almost linearly between the temperatures $T_0 + \frac{1}{2}$ and $T_0 - \frac{1}{2}$. The maximum velocity is relatively slow. With higher Grashof numbers the temperature isotherms begin to curve due to a stronger flow field.

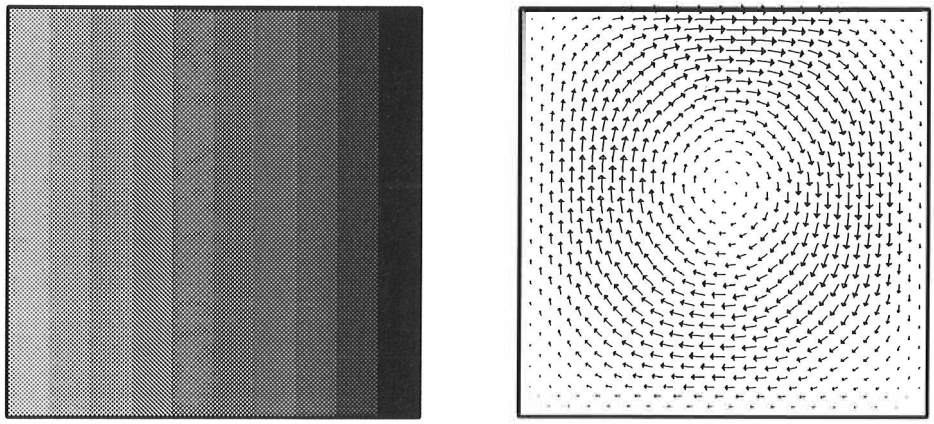

Figure 4.2 (a) Temperature isotherms and (b) velocity vectors for $Pr = 0.73$, $Ma = 0$ *and* $Gr = 2.0$

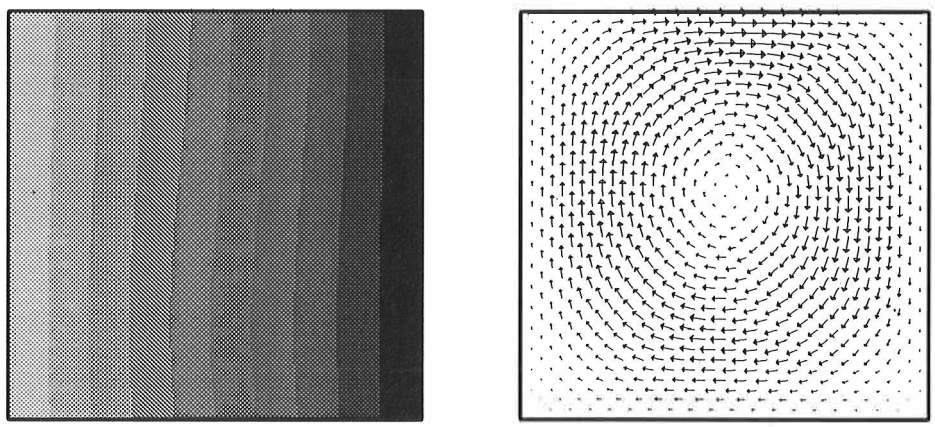

Figure 4.3 (a) Temperature isotherms and (b) velocity vectors for $Pr = 0.73$, $Ma = 0$ *and* $Gr = 2.0 \times 10^2$

The buoyancy force is a typical body force, i.e., it has an influence on liquid as a whole. On the other hand, the tangential stress boundary condition induces a surface flow. In this boundary condition the temperature coefficient of the sur-

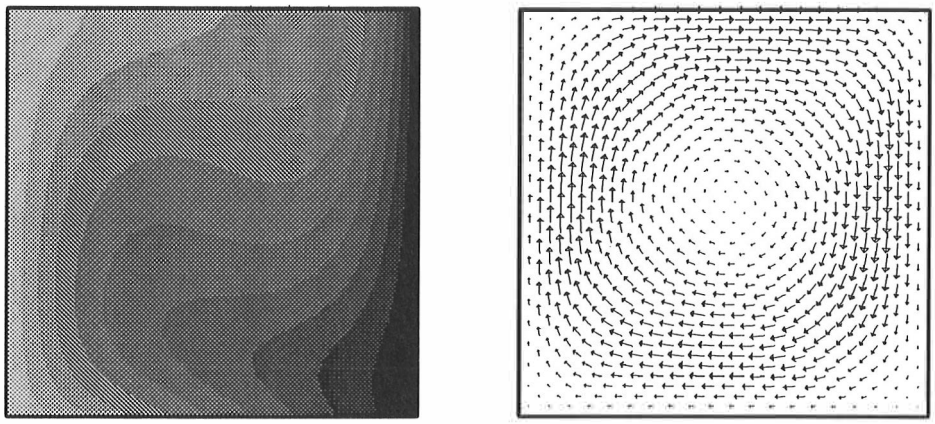

Figure 4.4 (a) Temperature isotherms and (b) velocity vectors for $Pr = 0.73$, $Ma = 0$ *and* $Gr = 2.0 \times 10^4$

face tension ϑ has the form $\vartheta = -(1/\gamma_0)(d\gamma/dT)|_{T_0}$, [Cuvelier86]. Tangential stress generates a flow from a region of the low surface tension to a region of the high surface tension, which normally means from hot to cold, [Cuvelier86]. This phenomenon with the different Marangoni numbers can be seen in Figures 4.5b and 4.6b, where the flow direction is from the left-hand vertical boundary to the right-hand vertical boundary.

For a low Marangoni number the thermal convection effects slightly to the temperature isotherms (Figure 4.5a). The high Marangoni number creates a strong temperature gradient near the right-hand vertical boundary.

In Table 4.1 the maximum velocity $|u|$ for the various Grashof and Marangoni numbers is given. The numerical results are in a good agreement compared to [Cuvelier86b] except in the case where the Marangoni number is equal to 400. In the reference [Cuvelier86b] the authors mention, however, that for high Marangoni numbers the magnitude of the velocity $\vec{u}$ can be estimated as $|u| \approx Ma^{\frac{2}{3}}$. In this sense our value of the maximum velocity for the case $Ma = 400$ seems to be closer to the evaluated value 54.288.

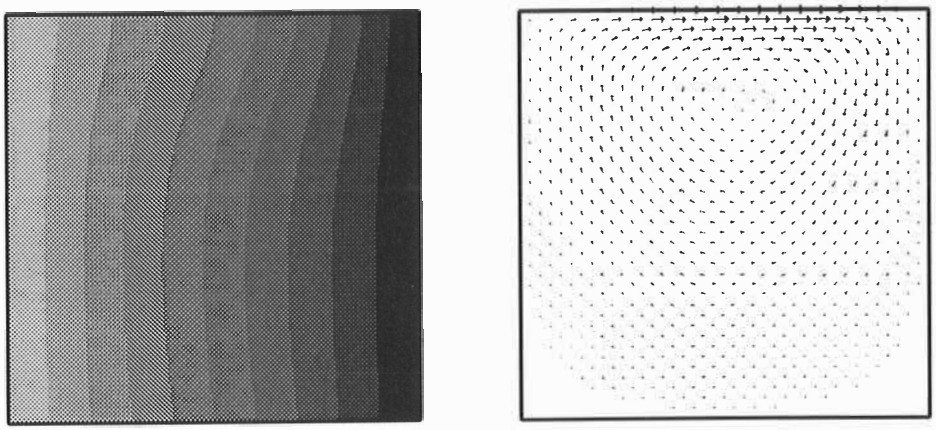

Figure 4.5 (a) Temperature isotherms and (b) velocity vectors for for $Pr = 0.73$, $Ma = 50$ *and* $Gr = 0.0$

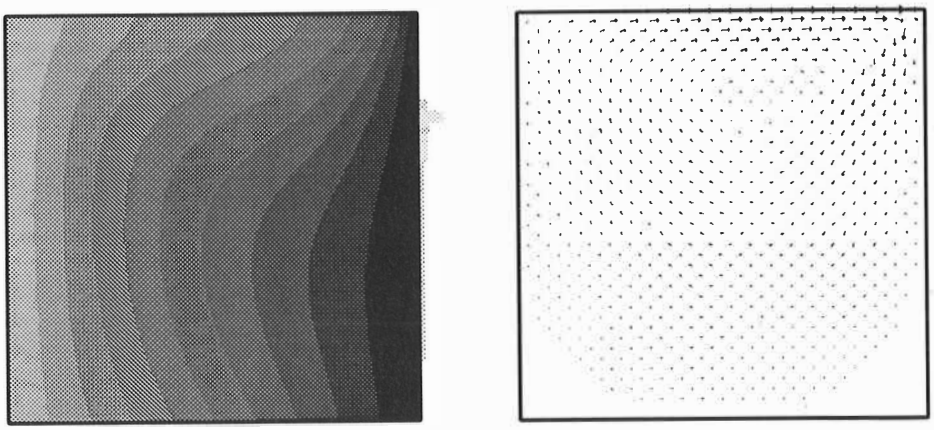

Figure 4.6 (a) Temperature isotherms and (b) velocity vectors for for $Pr = 0.73$, $Ma = 400$ *and* $Gr = 0.0$

Pr	Ma	Gr	$\|u\|_{[Cuvelier86b]}$	$\|u\|_{author}$
0.73	0.0	2.0	0.0125	0.01247
0.73	0.0	200.0	1.24	1.24233
0.73	0.0	20000.0	40.0	40.48588
0.73	50.0	0.0	9.12	9.07357
0.73	400.0	0.0	40.3	56.27472

Table 4.1 Numerical comparison between [Cuvelier86b] and the author

4.4.2 Rayleigh-Bénard Convection

In this section a Rayleigh-Bénard convection (mathematical model (M2) in Chapter 3.1.2) is studied numerically. The finite element discretization produces a nonlinear matrix equations for the velocity and the temperature:

$$
\begin{aligned}
M^u \frac{\partial u_1}{\partial t} + A_{11}u_1 + A_{12}u_2 &= D_1^u, \\
M^u \frac{\partial u_2}{\partial t} + A_{21}u_1 + A_{22}u_2 &= -F_2^u + D_2^u, \\
M^T \frac{\partial T}{\partial t} + AT &= D^T,
\end{aligned}
\tag{4.35}
$$

where the sub-matrices and the sub-vectors are presented in detail in Chapter 4.2. Only the buoyancy effect is taken into account. Gravity is assumed to act in the direction of the negative x_2-axis.

We simulate the water flow as in the reference [Argyris92]. The material parameters of water are shown in Table 4.2.

Quantity	Symbol	Value
Viscosity	μ	$9.93 \cdot 10^{-4}\ Pas$
Density	ρ	$998.2\ kg/m^3$
Heat capacity	c_p	$4182.5\ J/kgK$
Heat conductivity	k	$0.597\ W/mK$
Heat expansion coeff.	β	$2.1 \cdot 10^{-4}\ 1/K$
Gravity	g	$9.82\ m/s^2$

Table 4.2 Material data of water

In [Argyris92] the authors solve the problem by the Petrov-Galerkin finite element method. The penalty method is applied for the incompressible Navier-Stokes equations. The nonlinear matrix equation originated from the discretization of the Navier-Stokes equations is solved by the Newton method. The computation of the

velocity and the temperature is uncoupled. The implicit time discretization is used.

As before, we solve the coupled problem by uncoupling the Navier-Stokes and heat equations. The spatial discretization is made by the streamline upwinding/Petrov-Galerkin method as presented in Chapter 4.2 and the time derivative is discretized by the backward Euler method. The upwinding parameter is determined elementwise contrary to [Argyris92], where the authors fix the value of the upwinding parameter over the whole domain. The Newton linearization technique is applied for the nonlinear terms in the Navier-Stokes equations.

We divide the domain into 600 quadrilateral elements (40 elements in the x_1-direction and 15 elements in the x_2-direction). The space discretization differs from the one presented in [Argyris92], where they have less elements and their mesh is denser near the right vertical boundary. As in [Argyris92] we choose a constant time step to be equal to 2 seconds. Our calculation extends over 600 seconds and involves thus 300 time steps. The convection rolls begin to develop at $t = 210$ seconds and a steady state solution is reached at $t = 450$ seconds. The temperature isotherms and the velocity fields in the course of the process are presented at different time steps in Figures 4.8a-4.13b.

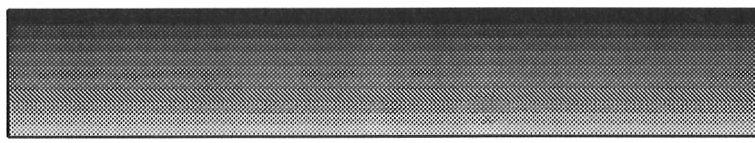

Figure 4.8a Temperature isotherms at $t = 200$

Figure 4.8b Velocity vectors at $t = 200$

The steady state solution is very similar as in the reference [Argyris92]. However, in our case the convection rolls begin to develop and the steady state solution is reached later than in [Argyris92]. In this reference the convection rolls began to develop at $t = 130$ and steady state was attained at $t = 190$. We solved the model problem also with a commercial fluid dynamics package called FIDAP. We used

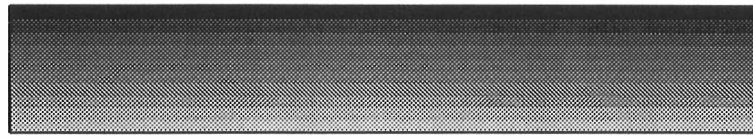

Figure 4.9a Temperature isotherms at $t = 250$

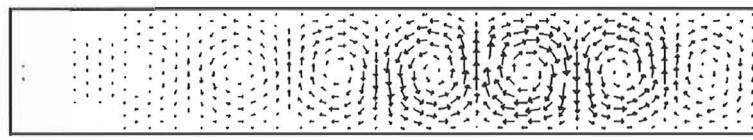

Figure 4.9b Velocity vectors at $t = 250$

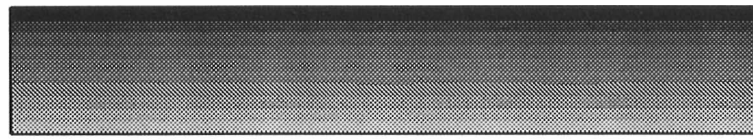

Figure 4.10a Temperature isotherms at $t = 300$

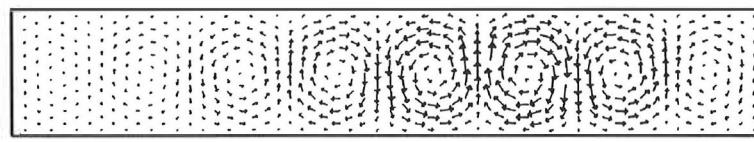

Figure 4.10b Velocity vectors at $t = 300$

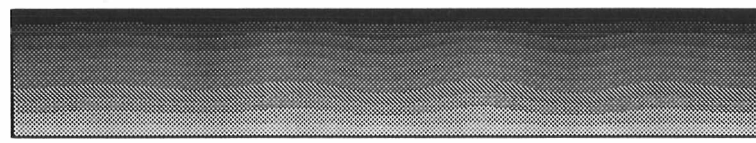

Figure 4.11a Temperature isotherms at $t = 350$

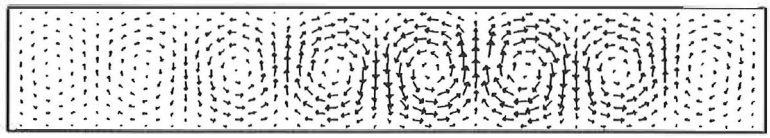

Figure 4.11b Velocity vectors at $t = 350$

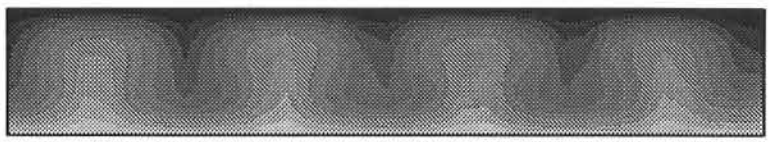

Figure 4.12a Temperature isotherms at $t = 400$

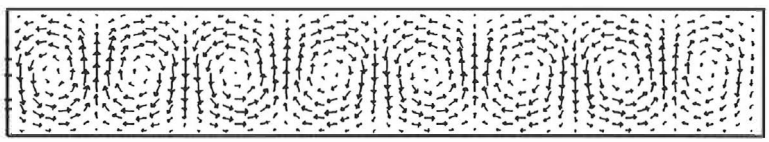

Figure 4.12b Velocity vectors at $t = 400$

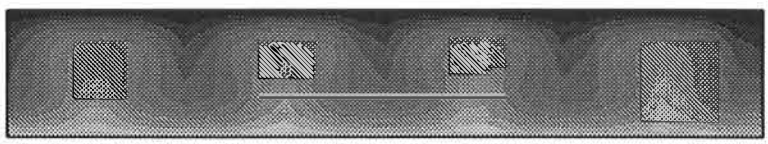

Figure 4.13a Temperature isotherms at $t = 450$

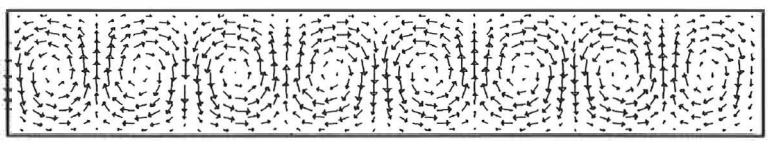

Figure 4.13b Velocity vectors at $t = 450$

the same parameters (material parameters, space and time discretizations) as in our own analysis. The steady state solution was again similar compared to the previous ones. The convection rolls began to develop approximately at the same time as in our analysis, namely at $t = 200$ seconds. The steady state was attained at $t = 450$ seconds.

4.4.3 Silicon Melt Flow

In this chapter we examine the effects of the Grashof, Marangoni and forced convections in the silicon melt. The mathematical model and the finite element discretization for the problem are introduced in Chapters 3.1.3 and 4.2. As was explained in Chapter 3.1.3, we restrict our consideration only to the melt, i.e., we neglect the effects of the surrounding parts. Furthermore, we assume axisymmetry of the melt. The dimensions of the melt correspond approximately to a 40 kg charge in the crucible, the diameter of which is 40 cm (16 inches). The height of the melt is then 12 cm.

The importance of numerical simulations of the melt flow is emphasized for instance in the cases where we have to clarify trajectories of pellets or a amount of oxygen which is transferred to the melt-crystal interface. Numerical simulations of the melt flow have proved, however, to be very difficult ([Kakimoto91], [Kinney93], [Müller93]) as a consequence of complicated nature of the flow field. The Grashof and Marangoni convections are induced by the temperature gradient in the melt and at the melt-gas interface. Furthermore, the centrifugal force caused by the rotating crucible increases complexity of the melt flow.

Using the penalty method, the streamline-upwinding/Petrov-Galerkin finite element discretization of the transient and coupled Navier-Stokes and heat equations produces the matrix equations (4.25) for the velocity components u_r, u_z and u_θ and the temperature T. As before, we uncouple the discretized equations. Bilinear basis functions for the velocity components and the temperature are used. The penalty terms are approximated by the reduced integration. The time derivatives in the Navier-Stokes and heat equations are discretized by the backward Euler method.

At each time step we have to solve both velocity and temperature fields in the whole domain. The Newton linearization technique applied for the nonlinear convection terms in the Navier-Stokes equations produces a linear matrix equation for velocity which is solved by the Gaussian elimination. The Navier-Stokes iteration is terminated when the relative error $\|u^k - u^{k-1}\|/\|u^k\|$ between consecutive Navier-Stokes iteration steps is less than 10^{-3}. As a distinction to the previous chapter, we apply the iterative solver also for the temperature. The temperature field is solved by the SOR method (successive over relaxation method) and the ending criteria of the SOR iteration is satisfied when the relative error $\|T^k - T^{k-1}\|/\|T^k\|$ is less than 10^{-3}. Inside of each time step we solve the velocity and the temperature

only once, i.e., we do not iterate the uncoupled problem.

We divide the domain into 60×36 quadrilateral elements. Throughout this chapter (except in the numerical computation of the initial guess for the Grashof convection, Figures 4.16a and 4.16b) we simulate the silicon melt flow and the material parameters of silicon are presented in Table 4.3.

Quantity	Symbol	Value
Density	ρ	2490.0 kg/m^3
Heat capacity	c_p	1000.0 J/kgK
Heat conductivity	k	64.0 W/mK
Viscosity	μ	$7.5 \cdot 10^{-4}$ kg/ms
Surface tension coeff.	γ_0	$0.72N/m$
Temperature coeff. of surface tension	ϑ	$1.4 \cdot 10^{-4}$ $1/K$
Heat expansion coeff.	β	$1.4 \cdot 10^{-4}$ $1/K$
Reference temperature	T_0	1685.0 K
Gravity	g	9.82 m/s^2

Table 4.3 Material data of silicon melt flow

In the following we study numerically the character of the Grashof and Marangoni convections and the effect of these convections together with the forced convection on the temperature field in the silicon melt.

As a reference we present (Figure 4.15) a steady temperature distribution in the melt when all convections are neglected, i.e., heat in the melt is transferred by conduction only. As a consequence of the description of the mathematical model (M3) the minimum temperature value in this case can be found at the melt-gas interface exactly on the symmetry axis where $T_{min} = 1685.73$ K. Let us mark this point with p.

We consider first the Grashof and Marangoni convections separately. Then we take into account the above convections simultaneously and finally we add the forced convection to the system.

It is well known that the numerical methods face problems in attaining convergence with high Reynolds numbers. These problems can partly be overcome by taking advantage of a good initial guess, using the method of reduced Reynolds number or relaxation. The method of reduced Reynolds number starts numerical computation with a reduced Reynolds number and then gradually, by taking advantage of results of preceding computation, increases the value of the Reynolds number towards the real one. The relaxation method sets a new value for the variable x as

$$x^n = \delta x^* + (1 - \delta) x^{n-1},$$

where $\delta \in [0, 1]$ is the relaxation parameter, x^{n-1} the value of the variable x in the previous iteration step and x^* the solution of the present iteration step. It is

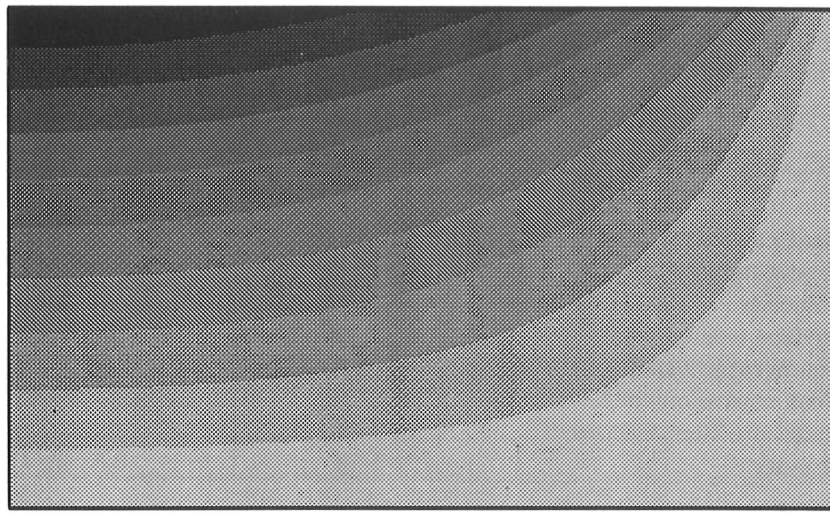

Figure 4.15 Temperature field induced by conduction

also well known that the Newton linearization technique, which is a second order method, requires a good initial guess to attain convergence. In order to achieve a proper initial guess we simulate the Grashof convection for a while (5 seconds with a 0.5 second time step) with a reduced Reynolds number, i.e., we multiply the real viscosity by 100. The velocity and temperature fields at $t = 5$ s are shown in Figures 4.16a and 4.16b, respectively.

The results presented in Figures 4.16a and 4.16b work as an initial guess when we simulate the silicon melt flow induced by the Grashof convection. The velocity and temperature fields at $t = 60$ s (time step 0.2 s) are shown in Figures 4.17a and 4.17b, respectively. These figures represent the steady-state solutions of the Grashof convection in the silicon melt. The Grashof convection forms a large main convection roll to the melt. Near the silica crucible wall the direction of the flow is up while on the symmetry axis the direction in down. The maximum velocity is $|\vec{u}| = 8.55$ cm/s and the temperature at the point p is $T(p) = 1702.40$. Thus the Grashof convection brings hot material from the silica crucible wall with it. On the other hand, colder material reaches the melt bottom in the neighborhood of the symmetry axis than in the case where only conduction was present.

We start the numerical simulation of the Marangoni convection with the results presented in Figure 4.15 as an initial guess, i.e., the temperature distribution is dominated by conduction and the velocity field is equal to zero. The steady state is reached after 60 seconds (time step 0.2 s) and the numerical results can be seen

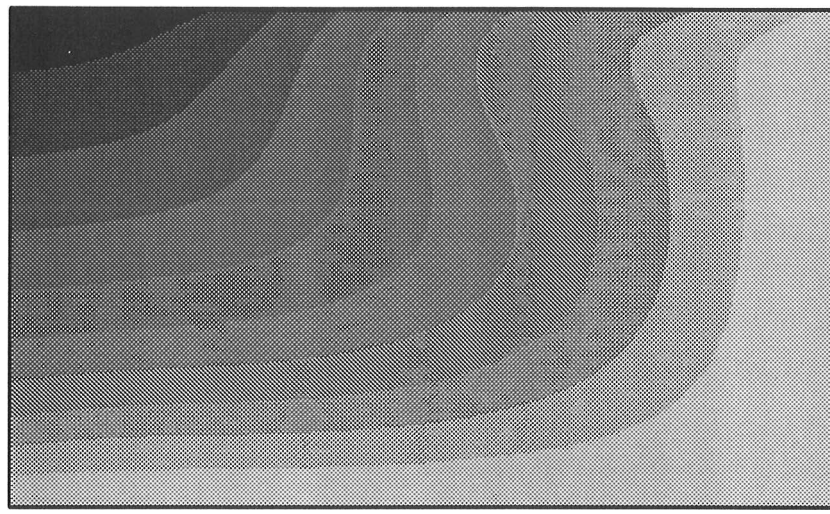

Figure 4.16a Temperature field induced by Grashof convection at $t = 5$, reduced Reynolds number

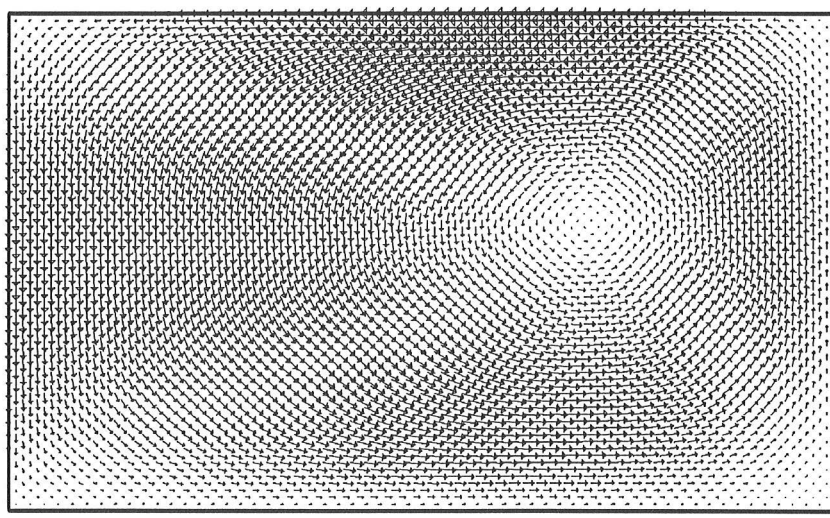

Figure 4.16b Velocity field induced by Grashof convection at $t = 5$, reduced Reynolds number

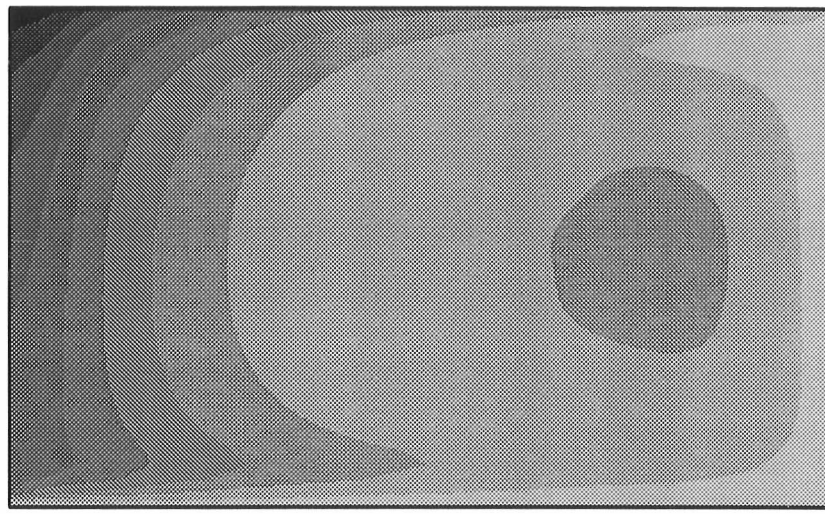

Figure 4.17a Temperature field induced by Grashof convection at $t = 60$

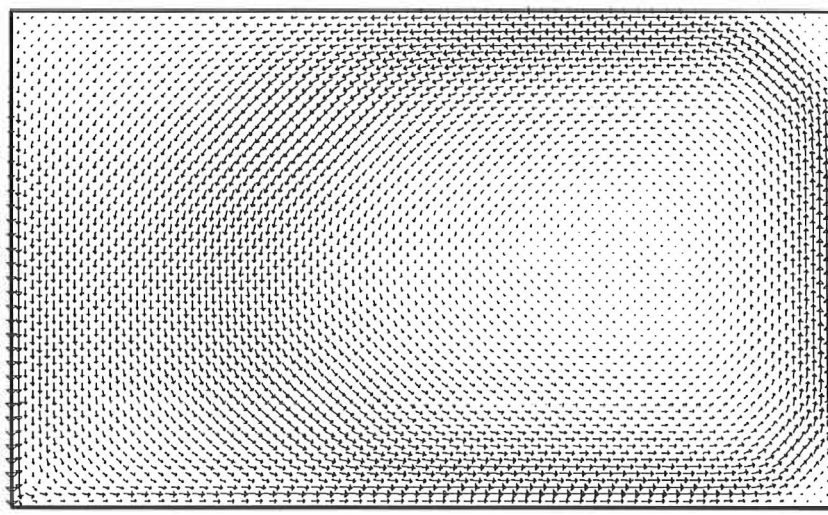

Figure 4.17b Velocity field induced by Grashof convection at $t = 60$

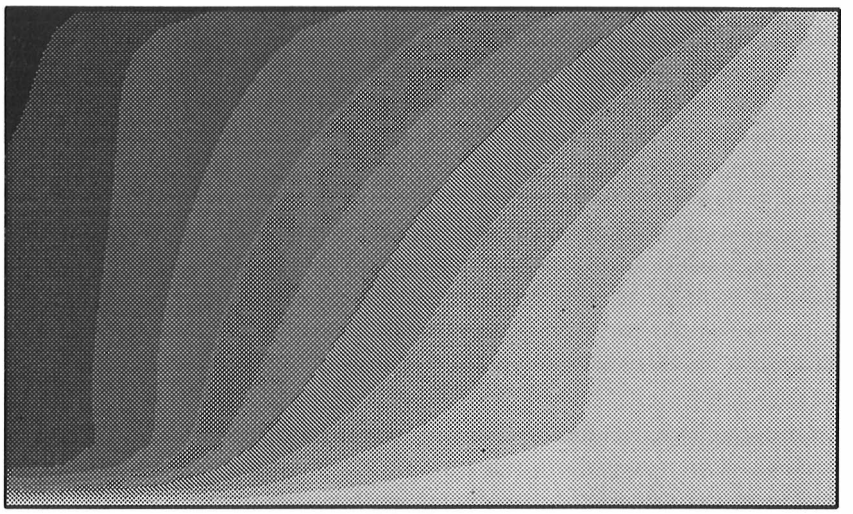

Figure 4.18a Temperature field induced by Marangoni convection at $t = 60$

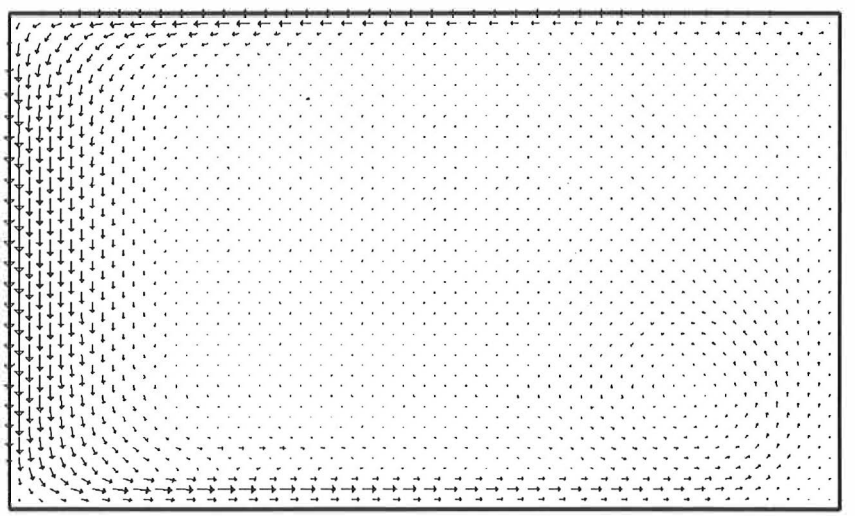

Figure 4.18b Velocity field induced by Marangoni convection at $t = 60$

in Figures 4.18a and 4.18b.

In Figure 4.18b one can easily see the surface flow due to the Marangoni convection at the melt-gas interface. The direction of the flow is from the silica crucible wall towards the symmetry axis, i.e., from hot to cold. The velocity field is also quite strong near the symmetry axis which explains the decrease of temperature there compared to the results presented in Figure 4.15. The maximum velocity is $|\vec{u}| = 3.53$ cm/s which is hardly half of the corresponding value of the Grashof convection. The temperature at the point p is $T(p) = 1690.61$. In the light of these numerical studies it seems that the effect of the Grashof convection on heat transfer mechanism is stronger than the effect of the Marangoni convection. Also we can conclude that the influence of the Grashof convection on the velocity field (maximum velocity) is more dramatic. Our own experience shows that with high Reynolds numbers it is more difficult to achieve convergence for the Grashof convection.

In the following we take into account all convection mechanisms. In order to study the behavior of the pressure in the silicon melt we present also the pressure fields in addition to the velocity and temperature fields.

We start with the numerical simulation of the Grashof and Marangoni convections. The initial guess for the velocity and temperature fields are as in Figures 4.17a and 4.17b, i.e., the steady state solution of the Grashof convection. From the initial state, the steady state solution is reached after ten seconds ($t = 70$ s, time step 0.2 s), Figures 4.19a, 4.19b and 4.19c. The maximum velocity $|u|$ in this case is 9.2 cm/s and the temperature at point p is $T(p) = 1703.97$. The velocity field differs only slightly from the one presented in Figure 4.17b. Only at the melt-gas interface where the Marangoni convection has an influence on the flow field one can noticc thc difference. The most remarkable difference between the temperature distributions in Figures 4.17a and 4.19a is the drifting of cold material from the melt-gas interface to the bottom of the melt near the symmetry axis.

To conclude this chapter we study numerically the effect of the centrifugal force, caused by the rotation of the melt, on the velocity field and temperature distribution induced by the Grashof and Marangoni convections. The initial guess of the numerical simulation is presented in Figures 4.19a and 4.19b. The rotation rate of the melt is assumed to be 5 and 15 rpm. The direction of the rotation is clockwise. The numerical results with the rotation rate 5 rpm are shown in Figures 4.20a-4.22c and with thc rotation ratc 15 rpm in Figures 4.23a-4.24c. The numerical results have been carried out with a time step of 0.2 s.

The rotation of the melt influences dramatically the velocity field and the temperature distribution in the melt. They are no longer steady as was the case in the numerical simulation of the Grashof and Marangoni convections. The main convection roll has disappeared, and there are several convection rolls whose number and positions vary in time.

If we simulate only the rotation of the melt, the velocity field reaches a state where

$u_r \approx 0$, $u_z \approx 0$ and $u_\theta \approx \omega_m r$. When the Grashof and Marangoni convections are also taken into account the structure of the angular velocity field is not any more so unambiguous. In the presence of the rotation the angular velocity field starts to develop from the crucible walls and during the simulations the effect of the rotation extends to the whole melt.

The over relaxation parameter by the SOR method was typically 1.0-1.4. The relaxation parameter in the Navier-Stokes iterations was 1.0, i.e., no under relaxation was needed. With the real Reynolds number the time step was 0.2 seconds and the Navier-Stokes and SOR iterations converged satisfactorily. The value 0.2 seconds was, however, quite critical. If the time step was lengthened, convergence during the Navier-Stokes iteration was lost. The use of under relaxation ($\delta \in [0.5 - 0.8]$) or increase of the coupled iterations inside of each time step did not improve the situation. The SOR iteration converged properly with longer time steps. Thus we conclude that the length of the time step is limited by the computation of the flow field.

In the finite element analysis we approximated the pressure by piecewise constant functions. From the pressure fields one can clearly see the elementwise behavior of the pressure. In these simulations the pressure fields seem to be quite satisfactory and the checkerboard pressure patterns do not appear. In the numerical simulations of the Grashof convection we proceeded so that we increased the Reynolds number step by step. The rotations of the crucible instead were taken into account very violently. We applied the rotation rates (5 and 15 rpm) instantly at $t = 70$ seconds and some problems in the pressure field were encountered (see for instance Figure 4.20c).

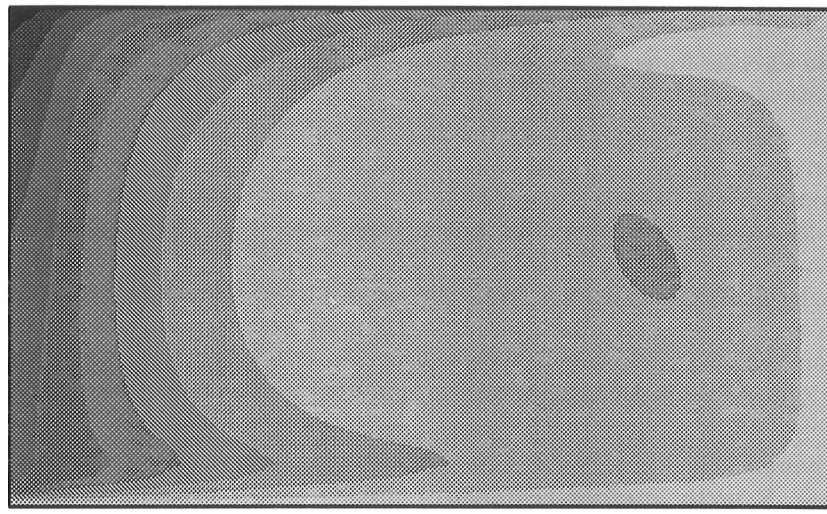

Figure 4.19a Temperature field induced by Grashof and Marangoni convections at $t = 70$

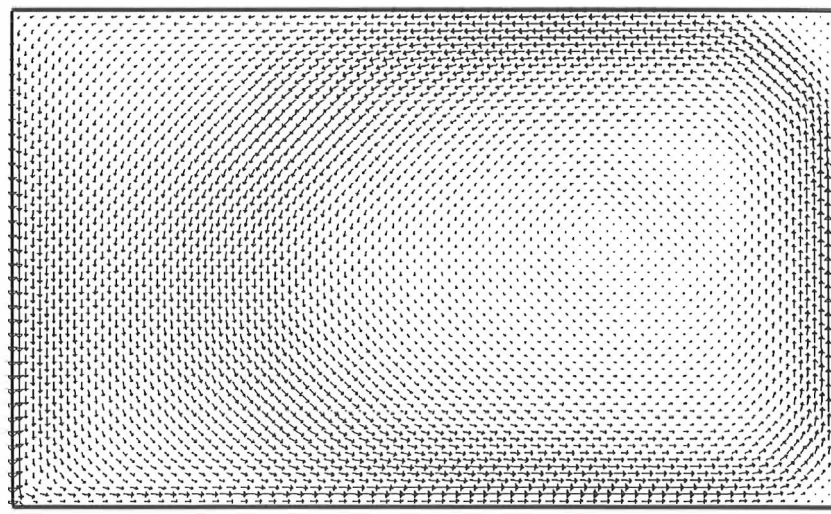

Figure 4.19b Velocity field induced by Grashof and Marangoni convections at $t = 70$

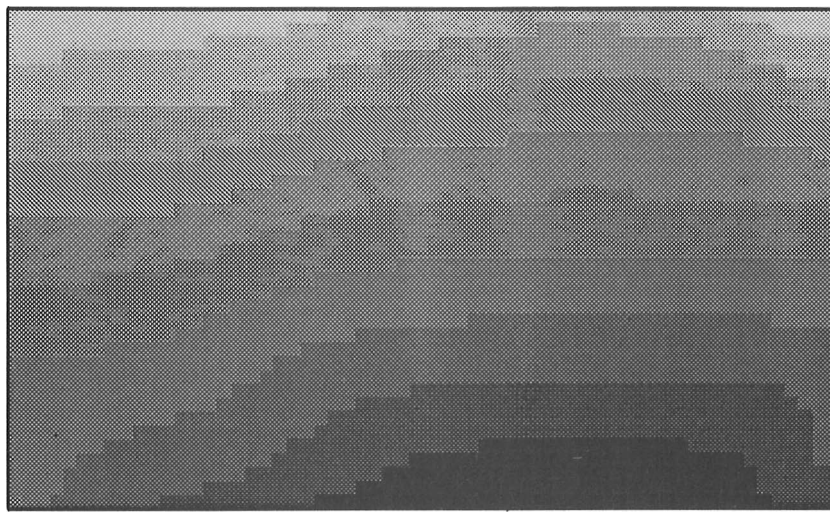

Figure 4.19c Pressure field induced by Grashof and Marangoni convections at $t = 70$

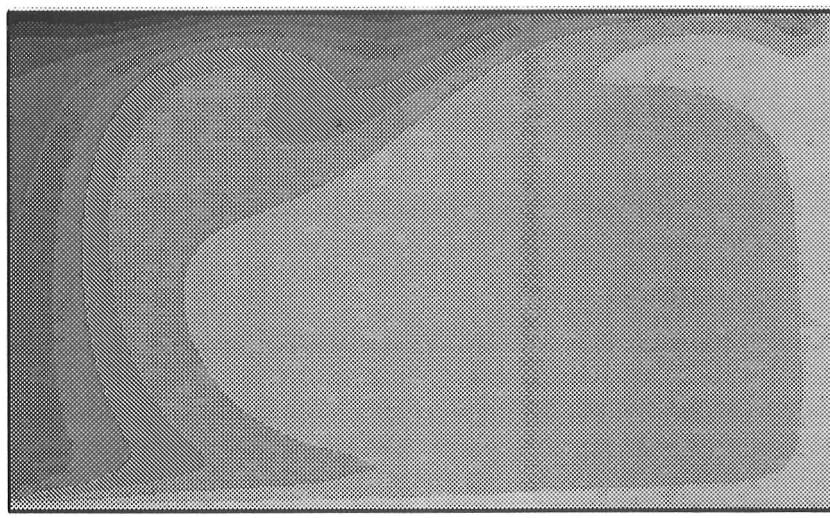

Figure 4.20a Temperature field induced by Grashof and Marangoni convections and rotation of melt 5 rpm at $t = 80$

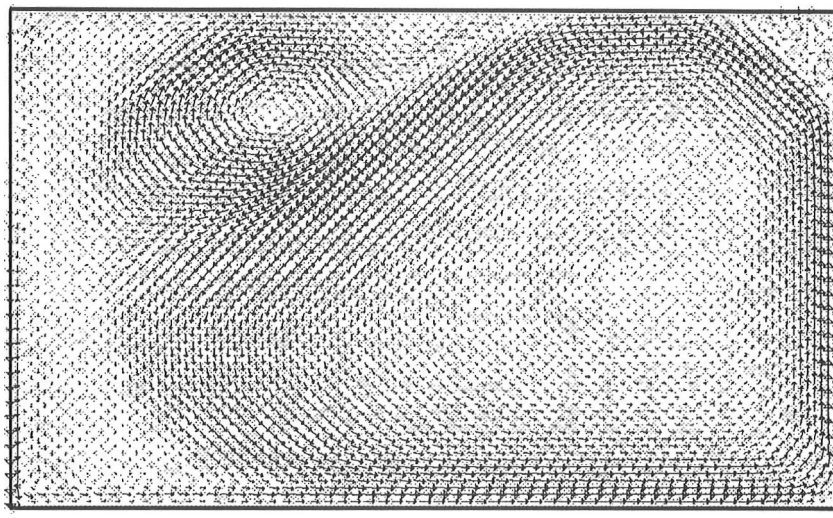

Figure 4.20b Velocity field induced by Grashof and Marangoni convections and rotation of melt 5 rpm at $t = 80$

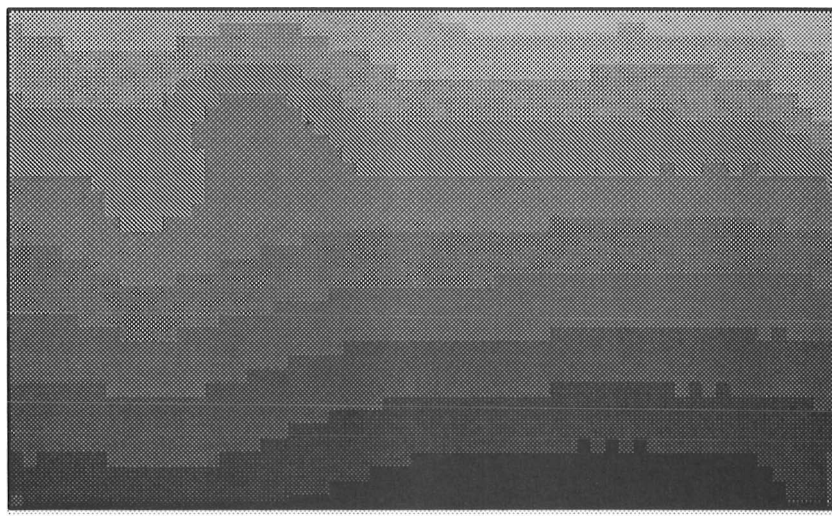

Figure 4.20c Pressure field induced by Grashof and Marangoni convections and rotation of melt 5 rpm at $t = 80$

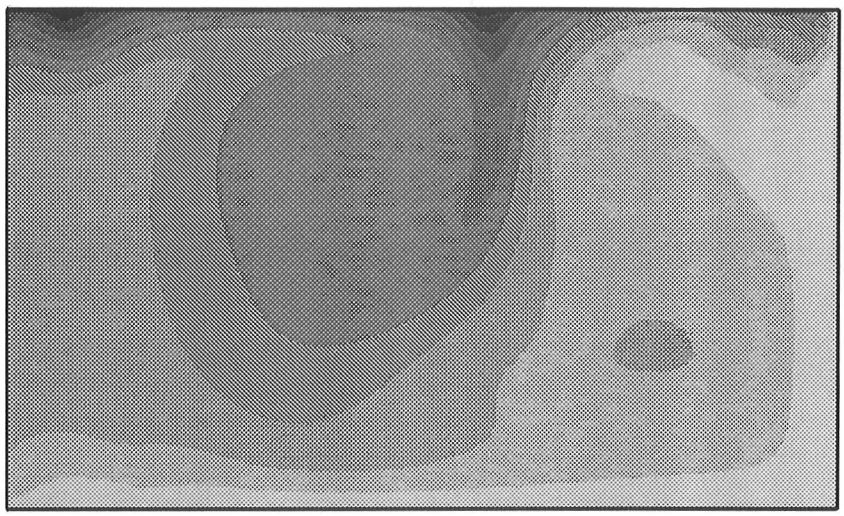

Figure 4.21a Temperature field induced by Grashof and Marangoni convections and rotation of melt 5 rpm at $t = 90$

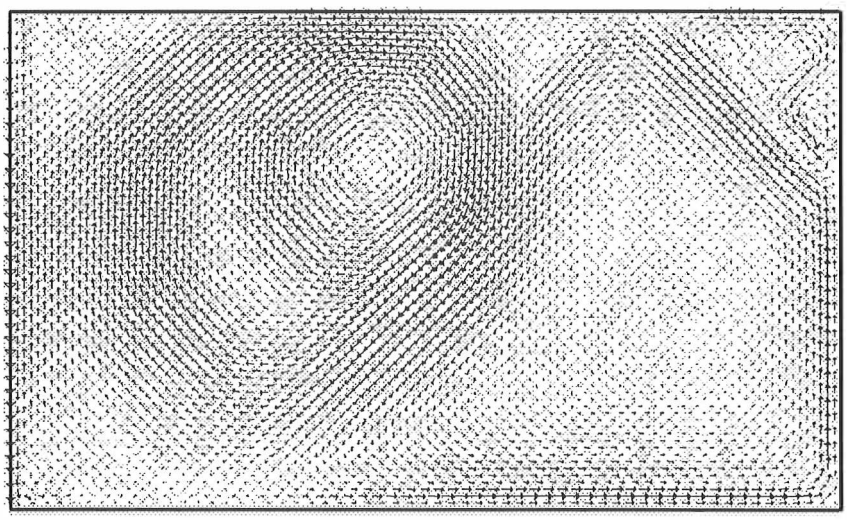

Figure 4.21b Velocity field induced by Grashof and Marangoni convections and rotation of melt 5 rpm at $t = 90$

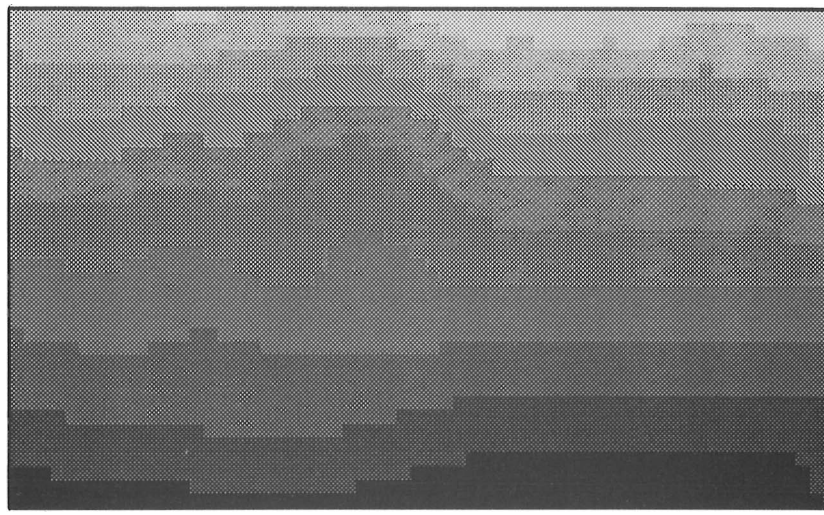

Figure 4.21c Pressure field induced by Grashof and Marangoni convections and rotation of melt 5 rpm at $t = 90$

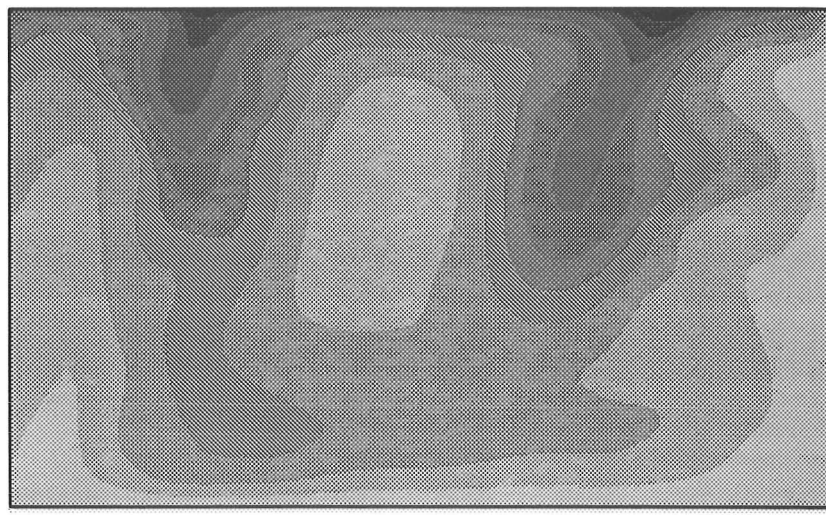

Figure 4.22a Temperature field induced by Grashof and Marangoni convections and rotation of melt 5 rpm at $t = 130$

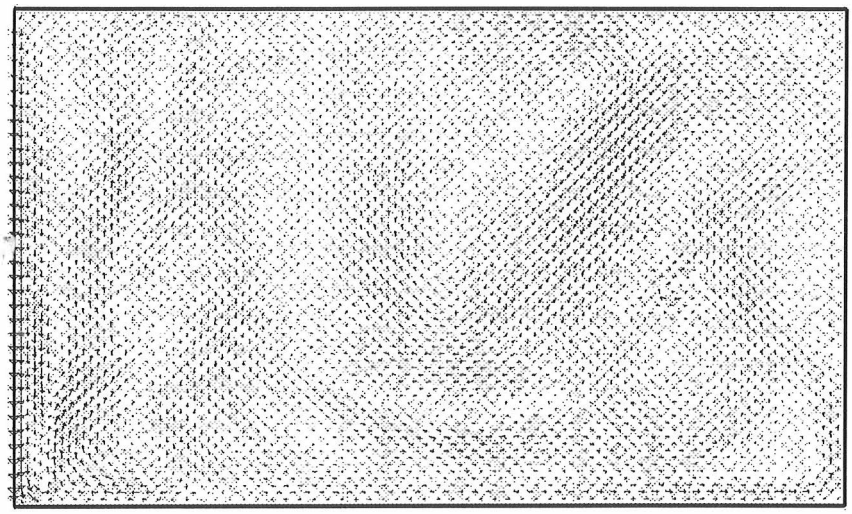

Figure 4.22b Velocity field induced by Grashof and Marangoni convections and rotation of melt 5 rpm at $t = 130$

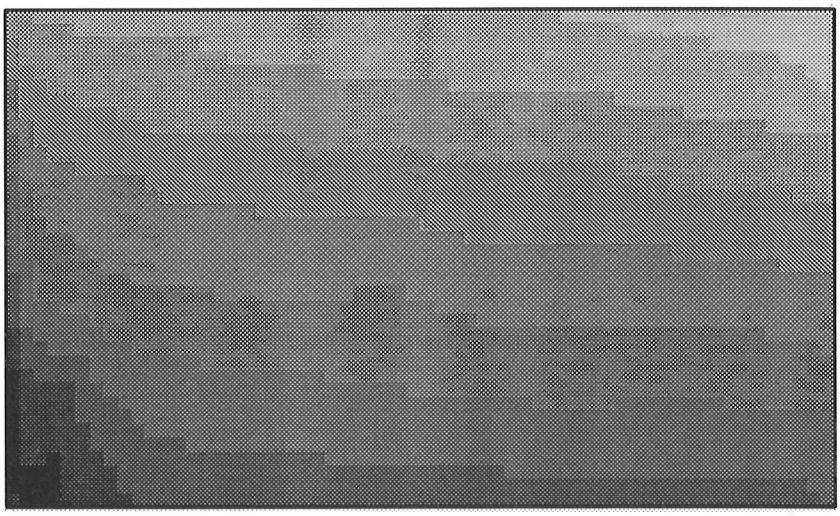

Figure 4.22c Pressure field induced by Grashof and Marangoni convections and rotation of melt 5 rpm at $t = 130$

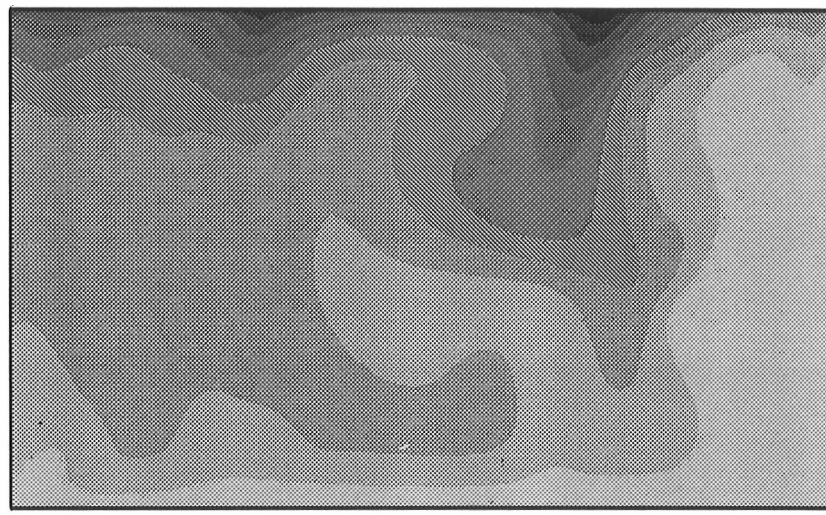

Figure 4.23a Temperature field induced by Grashof and Marangoni convections and rotation of melt 15 rpm at $t = 100$

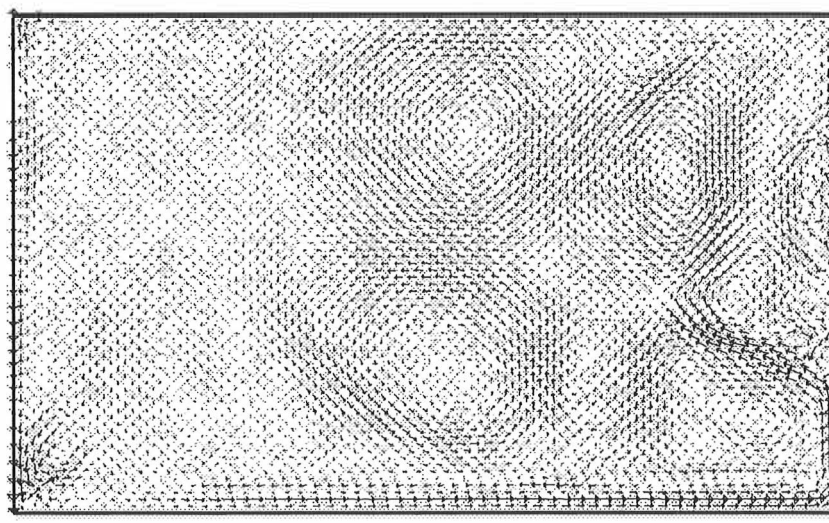

Figure 4.23b Velocity field induced by Grashof and Marangoni convections and rotation of melt 15 rpm at $t = 100$

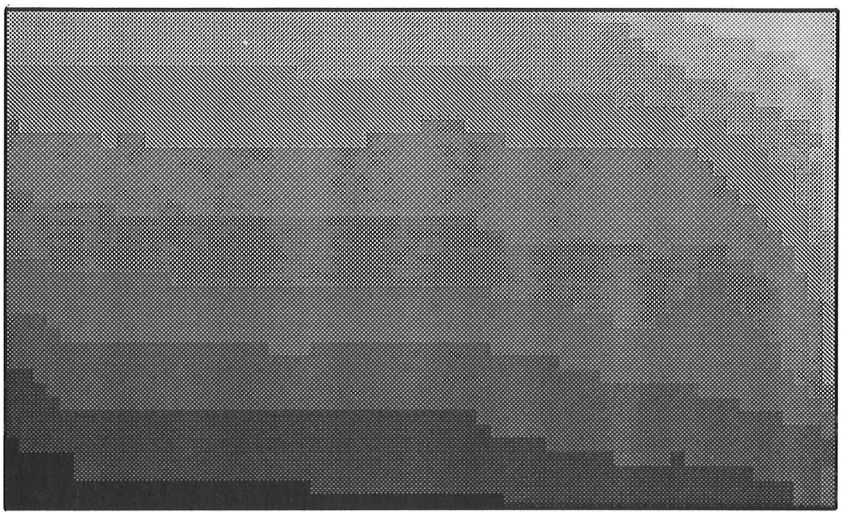

Figure 4.23c Pressure field induced by Grashof and Marangoni convections and rotation of melt 15 rpm at $t = 100$

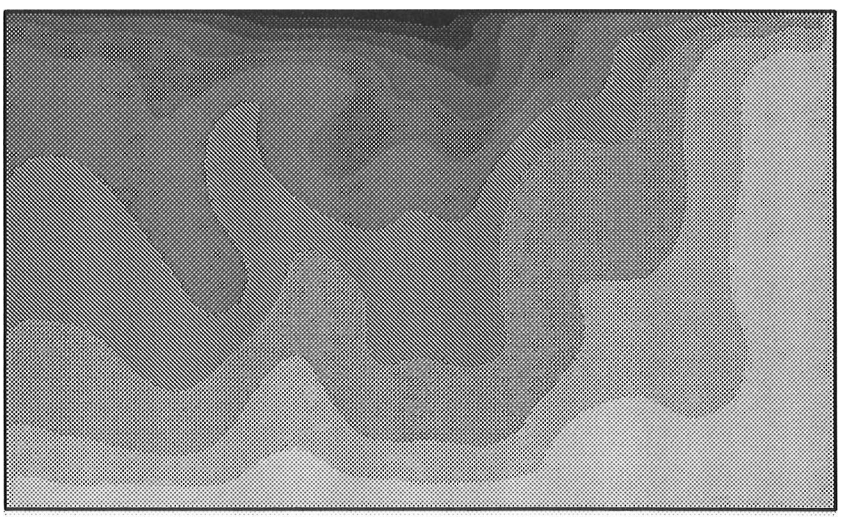

Figure 4.24a Temperature field induced by Grashof and Marangoni convections and rotation of melt 15 rpm at $t = 130$

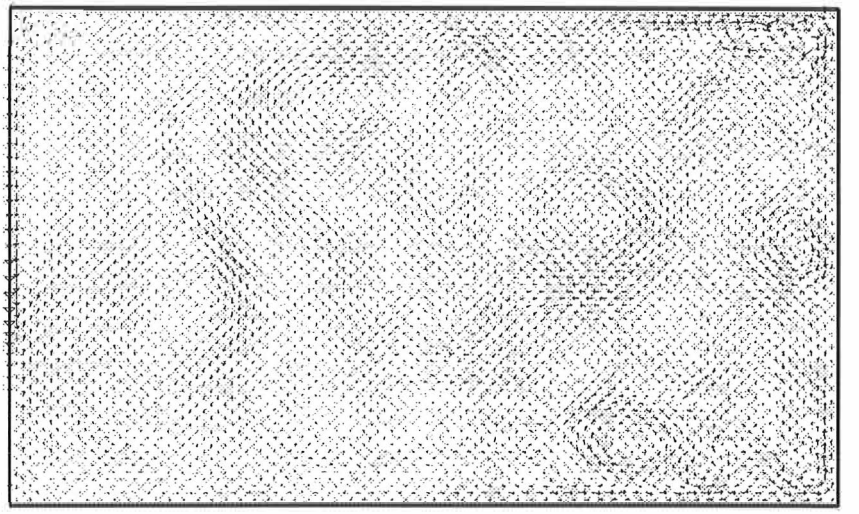

Figure 4.24b Velocity field induced by Grashof and Marangoni convections and rotation of melt 15 rpm at $t = 130$

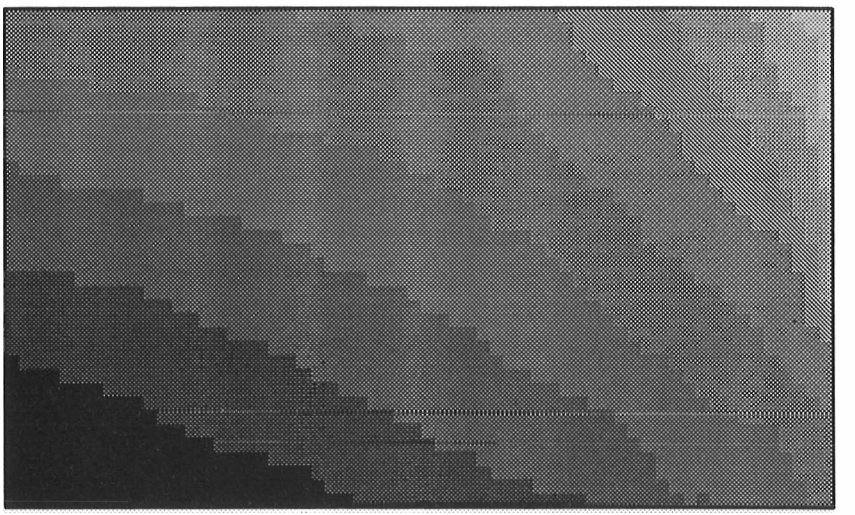

Figure 4.24c Pressure field induced by Grashof and Marangoni convections and rotation of melt 15 rpm at $t = 130$

5. Simulation of Crystal Growth from Melt

In Chapter 4.4.3 we confined ourselves to the numerical simulation of the silicon melt flow. Geometrically we considered only the melt, i.e., we neglected the surrounding parts. In this chapter we pay attention to the numerical simulation of the crystal-melt system. The numerical study of the melt flow plays an important role also in this chapter, since the presence of the crystal causes new physical phenomena in the melt.

Another crucial task in this chapter is the numerical treatment of a problem consisting of two phases, crystal and melt, separated by a free boundary. There are many ways to solve this free boundary problem. It can be formulated as a control problem [Männikkö94]. The finite element discretization of the equation $T-T_f = 0$ on the free boundary Σ leads to a case where positions of finite element nodes on the free boundary are considered as independent variables, [Derby87], [Sackinger89]. The shape of the free boundary can be fixed and temperature within that shape is calculated after disregarding one of the boundary conditions ((3.16a) or (3.16b)) on the free boundary. Next, a new free boundary shape is calculated, which satisfies as closely as possible the relaxed boundary condition, [Järvinen92]. As we presented it in Chapter 3.2, one can also determine an equation for enthalpy, which contains the definition of the free boundary, [Dalhuijsen86], [Voller87], [White82].

The methods used in [Derby87], [Sackinger89] and [Järvinen92] are typical front tracking methods in which discrete phase change front is tracked continuously. The enthalpy method is a fixed grid method, where the position of the free boundary is not tracked continuously but derived afterwards. The enthalpy method and the method used in [Derby87] and [Sackinger89] lead to a nonlinear matrix equation which has to be solved iteratively. The method used in [Järvinen92] generates a sequence of linear matrix equations.

As we have already mentioned, we use the enthalpy method in this work. Typically this method has been used in numerical simulations of casting problems ([Laitinen89]) since it offers a way to consider mushy regions. As a fixed grid method it has many advantages: It is easily adapted for existing computer programs and finite element mesh has to be built only once. Furthermore, it has a simple representation of the latent heat release at the free interface.

It is quite straightforward to apply the enthalpy method in order to determine the values of enthalpy in the crystal-melt system. It is not trivial, however, to solve the Navier-Stokes equations in the changing geometry. The discretization of the enthalpy equation leads to a nonlinear matrix equation which is coupled with the computation of velocity through a convection term. The discretization

of the Navier-Stokes equations (made within the melt in Chapter 4.1) consists of the buoyancy and thermocapillary terms depending on temperature. If we uncouple the computation of enthalpy and velocity, temperature can be used in the discretized Navier-Stokes equations after enthalpy is known. The enthalpy values determine the position of the crystal-melt interface. Or to be more precise, they determine the positions of two interfaces between crystal and mushy region and mushy region and melt. The interfaces do not coincide with finite element boundaries but go through finite elements. From point of view of the melt flow computation this gives rise to problems, since we have to handle elements in finite element analysis which are partly in the melt and partly in other phase.

In order to overcome the difficulty discussed above, we modify the mathematical model (M4) constructed in Chapter 3.2 from the parts describing the melt flow and conclude a modified mathematical model: Find the velocity vector $\vec{u} = (u_r, u_z, u_\theta)$, the pressure p and the enthalpy H such that

(M4')

$$
\begin{cases}
\rho_m \dfrac{\partial u_r}{\partial t} - \dfrac{\partial \sigma_{zr}}{\partial z} - \dfrac{1}{r}\dfrac{\partial}{\partial r}(r\sigma_{rr}) + \dfrac{1}{r}\sigma_{\theta\theta} + \rho_m\left(u_r\dfrac{\partial u_r}{\partial r} + u_z\dfrac{\partial u_r}{\partial z} - \dfrac{u_\theta^2}{r}\right) = 0 \\
\rho_m \dfrac{\partial u_z}{\partial t} - \dfrac{\partial \sigma_{zz}}{\partial z} - \dfrac{1}{r}\dfrac{\partial}{\partial r}(r\sigma_{zr}) + \rho_m\left(u_r\dfrac{\partial u_z}{\partial r} + u_z\dfrac{\partial u_z}{\partial z}\right) = \\
\qquad = \rho_m g\beta(T - T_0) \\
\rho_m \dfrac{\partial u_\theta}{\partial t} - \dfrac{1}{r^2}\dfrac{\partial}{\partial r}(r^2\sigma_{r\theta}) - \dfrac{\partial \sigma_{\theta z}}{\partial z} + \rho_m\left(u_r\dfrac{\partial u_\theta}{\partial r} + u_z\dfrac{\partial u_\theta}{\partial z} + \dfrac{u_r u_\theta}{r}\right) = 0 \\
\dfrac{1}{r}\dfrac{\partial}{\partial r}(ru_r) + \dfrac{\partial u_z}{\partial z} = 0 \\
\dfrac{\partial}{\partial t}H + \vec{u}\cdot\nabla H - \dfrac{1}{r}\dfrac{\partial}{\partial r}\left(r\dfrac{\partial}{\partial r}\Phi(H)\right) - \dfrac{\partial}{\partial z}\left(\dfrac{\partial}{\partial z}\Phi(H)\right) = 0
\end{cases}
$$

in $\Omega \times (0, t_0)$, $\Omega = \Omega_m \cup \Omega_c$, with the initial and boundary conditions

$$
\begin{cases}
\vec{u}(r,z,0) = \vec{u}^0(r,z) \quad \text{in } \Omega \\
H(r,z,0) = H^0(r,z) \quad \text{in } \Omega \\
u_r = 0,\ \dfrac{\partial u_z}{\partial r} = 0,\ u_\theta = 0,\ \dfrac{\partial \Phi(H)}{\partial r} = 0 \quad \text{on } \Gamma_s \times (0,t_0) \\
u_r = 0,\ u_z = 0,\ u_\theta = \omega_m r,\ H = H_0 \quad \text{on } \Gamma_m \times (0,t_0) \\
\vec{u}\cdot\vec{n} = 0,\ \sigma_n = \dfrac{\gamma_0}{R} - p_a,\ \sigma_\tau = -\vartheta\gamma_0\dfrac{\partial T(H)}{\partial \tau},\ -\dfrac{\partial \Phi(H)}{\partial n} = \alpha(T(H) - T_{ext}) \\
\qquad \text{on } \Gamma_{mg} \times (0,t_0) \\
u_r = 0,\ u_z = 0,\ u_\theta = \omega_c r,\ -\dfrac{\partial \Phi(H)}{\partial n} = \alpha(T(H) - T_{ext}) \\
\qquad \text{on } \Gamma_{cg} \times (0,t_0),
\end{cases}
$$

where the components of the stress tensor are as in the equations (3.14a-f). The definitions of the functions H, T and $\Phi(H)$ are as in (3.23), (3.25) and (3.26), respectively.

The only difference between the mathematical models (M4) and (M4') is that in (M4') the Navier-Stokes equations are introduced, not only in the melt, but in both crystal and melt. Nevertheless, it is still required that the velocity components u_r and u_z are zero in the crystal. There are a number of techniques by which this kind of behavior of velocities in the vicinity of the phase change can be modeled. In this work we use a variable viscosity method (see Chapter 5.3), in which the viscosity is set to be high in the crystal and therefore the velocity components are forced to be equal to zero. The other methods, such as 'Switch-off techniques' and 'Darcy source technique' are discussed in [Voller87].

We do not present here the variational formulations of the Navier-Stokes equations in (M4'), since they differ only slightly from the ones made in Chapter 4.1.2 (the variational formulations (4.16)-(4.18)). Some remarks are still required.

Remark 5.2 In this work the melt-gas interface is assumed to be fixed. Thus one boundary condition at this interface can be eliminated. We neglect the boundary condition $\sigma_n = \frac{\gamma_0}{R} - p_a$ on Γ_{mg} as we did in the case of the pure melt flow. The shape of the melt-gas interface is based on the analytical representation of the shape of the meniscus presented by Hurle. This representation has been shown to compare well with the full iterative numerical solution of the Laplace-Young equation with appropriate parameters of germanium, [Hurle83]. In the derivation of the analytical representation it has been assumed that the melt-gas interface extends to infinity and there is no rotation or melt flow.

Remark 5.3 Since we add the Dirichlet boundary conditions to the crystal-gas interface, we can assume for the test functions that $v_r = v_z = v_\theta = 0$ on Γ_{cg}. Therefore the only difference in the variational formulations is the integration over the domain $\Omega = \Omega_m \cup \Omega_c$ instead of Ω_m. The finite element discretization of the Navier-Stokes equations leads to the same matrix equations for the velocity components as in (4.25).

In the following the variational formulation and the finite element discretization for the enthalpy equation in (M4') are derived (Chapters 5.1 and 5.2). The solution algorithms for the phase change problem and the coupled velocity-enthalpy formulation in the crystal-melt system are presented in Chapter 5.3. Numerical examples for the silicon crystal-silicon melt system complete the Chapter 5.

5.1 Variational Formulation of Enthalpy Equation

The variational formulation and the results of existence and uniqueness of the enthalpy equation (and Stefan problem generally) are considered in detail in [Elliot82] and [Verdi94]. Let the solution H of the enthalpy equation in (M4') be

smooth enough in $\Omega \times (0, t_0)$ and the test function space $H_r^1(\Omega)$ be as $H_r^1(\Omega) = \{v \in L_r^2(\Omega) | \frac{\partial v}{\partial r}, \frac{\partial v}{\partial z} \in L_r^2(\Omega)\}$, where $L_r^2(\Omega)$ is the space of square integrable functions weighted by r in Ω. Then by multiplying the enthalpy equation by a test function v, observing the weight r, integrating over the domain Ω and applying Green's theorem we have

$$\int_\Omega \frac{\partial}{\partial t} Hvr \, d\Omega + \int_\Omega (\vec{u} \cdot \nabla) Hvr \, d\Omega + \int_\Omega (\nabla \Phi(H) \cdot \nabla v) \, r \, d\Omega - \int_{\partial\Omega} \frac{\partial \Phi(H)}{\partial n} vr \, dS = 0.$$

Application of the boundary condition for the enthalpy results

$$\begin{aligned} &\int_\Omega \frac{\partial}{\partial t} Hvr \, d\Omega + \int_\Omega (\vec{u} \cdot \nabla) Hvr \, d\Omega + \int_\Omega (\nabla \Phi(H) \cdot \nabla v) \, r \, d\Omega + \\ &+ \int_{\Gamma_{mg} \cup \Gamma_{cg}} \alpha T(H) vr \, dS = \int_{\Gamma_{mg} \cup \Gamma_{cg}} \alpha T_{ext} vr \, dS. \end{aligned} \tag{5.1}$$

5.2 Petrov-Galerkin Finite Element Approximation

The Petrov-Galerkin finite element approximation for the enthalpy follows the approximations made in Chapter 4.2 for the velocity and the temperature. The enthalpy is approximated as a linear combination of basis functions

$$H = \sum_{j=1}^{n} H_j \varphi_j, \tag{5.2}$$

where $H_j \in \mathbb{R}$ is the value of the enthalpy depending on time t. The substitution of the linear combination (5.2) into the variational formulation (5.1) and the replacement of the test function v with the basis functions produce an algebraic system for H:

$$M \frac{\partial H}{\partial t} + CH + K\Phi(H) + BT(H) = F, \tag{5.3}$$

where the sub-matrices and the sub-vector are

$$\begin{aligned} M(i,j) &= \int_\Omega \hat{\varphi}_i \varphi_j r \, d\Omega, \\ C(i,j) &= \int_\Omega \hat{\varphi}_i \, (\vec{u} \cdot \nabla \varphi_j) \, r \, d\Omega, \\ K(i,j) &= \int_\Omega (\nabla \varphi_i \cdot \nabla \varphi_j) \, r \, d\Omega, \\ B(i,j) &= \int_{\Gamma_{mg} \cup \Gamma_{cg}} \alpha \varphi_i \varphi_j r \, dS, \\ F(i) &= \int_{\Gamma_{mg} \cup \Gamma_{cg}} \alpha T_{ext} \varphi_i r \, dS, \end{aligned} \tag{5.4}$$

$i, j = 1, ..., n$. As in Chapter 4.2 the mass matrix and the convection matrix C contain modified basis function $\hat{\varphi}_i$ originated from the streamline upwinding/Petrov-Galerkin technique.

The time discretization in equation (5.3) is made by the backward Euler method. We lump the mass matrix in order to avoid the oscillations which may otherwise occur in the enthalpy computation, [Dalhuijsen86].

5.3 Solution Algorithms

In this chapter we present two algorithms. In Algorithm 5.1 we concentrate on the solution of the enthalpy (and thus the solution of the free boundary) from the nonlinear matrix equation (5.3) by the SOR method whereas in Algorithm 5.2 we are interested in the solution of the whole system including the temperature distribution and the velocity field in the crystal and melt.

Let us make some preparations for the first algorithm. The backward Euler method produces a matrix equation

$$\frac{1}{\Delta t} M H^{i+1} + C H^{i+1} + K\Phi(H^{i+1}) + BT(H^{i+1}) = F^{i+1} + \frac{1}{\Delta t} M H^i, \tag{5.5}$$

where Δt is the length of the time step and i and $i+1$ represent consecutive time steps. At each time step we have to solve a problem

$$\hat{M} H + C H + K\Phi(H) + BT(H) = \hat{F}, \tag{5.6}$$

where $\hat{M} = \frac{1}{\Delta t} M$ and $\hat{F} = F^{i+1} + \frac{1}{\Delta t} M H^i$. In order to simplify notations we have disregarded the superscripts in the equation (5.6).

In Algorithm 5.1 we use the following notations: the superscripts indicate the SOR iteration level whereas the subscripts indicate the current position in a vector or in a matrix.

Algorithm 5.1

0. Initialization

Set *iter* := 1 and $k = 0$; Assumptions: the matrices $\hat{M}$, C, K, and B and the vector $\hat{F}$ are known, the enthalpy vector H^k has an initial value.

1. SOR-iteration for all i=1,...,n

1.1 Gauss-Seidel step

Calculate the right hand side of the equation

$$\hat{M}_{ii} H_i^{k+1} + C_{ii} H_i^{k+1} + K_{ii}\Phi(H_i^{k+1}) + B_{ii} T(H_i^{k+1}) = z_i^k,$$

where

$$z_i^k := \hat{F}_i - \sum_{j=1}^{i-1} \left[\hat{M}_{ij} H_j^{k+1} + C_{ij} H_j^{k+1} + K_{ij} \Phi(H_j^{k+1}) + B_{ij} T(H_j^{k+1}) \right] - \sum_{j=i+1}^{n} \left[\hat{M}_{ij} H_j^k + C_{ij} H_j^k + K_{ij} \Phi(H_j^k) + B_{ij} T(H_j^k) \right].$$

The definitions of the functions $T(H)$ and $\Phi(H)$ (equations (3.25) and (3.26)) are used in order to calculate the nodal values of $T(H_j^{()})$ and $\Phi(H_j^{()})$.

1.2 Phase change points

Calculate the phase change points between crystal and mushy region and mushy region and melt. From the definitions (3.25) and (3.26) it follows that

$$T(H_i^{k+1}) = T_f \text{ and } \Phi(H_i^{k+1}) = k_c T_f.$$

Then

$$\hat{M}_{ii} H_i^{k+1} + C_{ii} H_i^{k+1} + K_{ii} k_c T_f + B_{ii} T_f = z_i^k,$$

from which

$$H_i^{k+1} = \frac{z_i^k - K_{ii} k_c T_f - B_{ii} T_f}{\hat{M}_{ii} + C_{ii}} \in [\rho_c c_{p_c} T_f, \rho_c c_{p_c} T_f + \rho_c L].$$

Since H_i^{k+1} belongs to the mushy region it holds for z_i^k that

$$z_i^k \in [\rho_c c_{p_c} T_f (\hat{M}_{ii} + C_{ii}) + K_{ii} k_c T_f + B_{ii} T_f, \; (\rho_c c_{p_c} T_f + \rho_c L)(\hat{M}_{ii} + C_{ii}) + K_{ii} k_c T_f + B_{ii} T_f].$$

Define

$$val_{crystal/mushy} := \rho_c c_{p_c} T_f (\hat{M}_{ii} + C_{ii}) + K_{ii} k_c T_f + B_{ii} T_f,$$
$$val_{mushy/melt} := (\rho_c c_{p_c} T_f + \rho_c L)(\hat{M}_{ii} + C_{ii}) + K_{ii} k_c T_f + B_{ii} T_f.$$

1.3 SOR step

Point in crystal:

If z_i^k is less than $val_{crystal/mushy}$ then set

$$T(H_i^{k+1}) = \frac{1}{\rho_c c_{p_c}} H_i^{k+1} \text{ and } \Phi(H_i^{k+1}) = \frac{k_c}{\rho_c c_{p_c}} H_i^{k+1}.$$

Then

$$\hat{M}_{ii}H_i^{k+1} + C_{ii}H_i^{k+1} + K_{ii}\frac{k_c}{\rho_c c_{p_c}}H_i^{k+1} + B_{ii}\frac{1}{\rho_c c_{p_c}}H_i^{k+1} = z_i^k,$$

from which

$$H_i^{k+1} = \frac{z_i^k}{\hat{M}_{ii} + C_{ii} + K_{ii}\frac{k_c}{\rho_c c_{p_c}} + B_{ii}\frac{1}{\rho_c c_{p_c}}}.$$

If H_i^k is less than $val_{crystal/mushy}$ then take the SOR step

$$H_i^{k+1} = H_i^k + \omega(H_i^{k+1} - H_i^k).$$

Point in mushy region:

If z_i^k is greater or equal to $val_{crystal/mushy}$ and less or equal to $val_{mushy/melt}$ then set

$$T(H_i^{k+1}) = T_f \text{ and } \Phi(H_i^{k+1}) = k_c T_f.$$

Then

$$\hat{M}_{ii}H_i^{k+1} + C_{ii}H_i^{k+1} + K_{ii}k_c T_f + B_{ii}T_f = z_i^k,$$

from which

$$H_i^{k+1} = \frac{z_i^k - K_{ii}k_c T_f - B_{ii}T_f}{\hat{M}_{ii} + C_{ii}}.$$

Point in melt:

If z_i^k is greater than $val_{mushy/melt}$ then set

$$T(H_i^{k+1}) = \frac{H_i^{k+1} - \rho_c L - \rho_c c_{p_c} T_f}{\rho_m c_{p_m}} + T_f \text{ and}$$

$$\Phi(H_i^{k+1}) = \frac{k_m(H_i^{k+1} - \rho_c L - \rho_c c_{p_c} T_f)}{\rho_m c_{p_m}} + k_m T_f + (k_c - k_m)T_f.$$

Then

$$\hat{M}_{ii}H_i^{k+1} + C_{ii}H_i^{k+1} + K_{ii}\frac{k_m}{\rho_m c_{p_m}}H_i^{k+1} + B_{ii}\frac{1}{\rho_m c_{p_m}}H_i^{k+1} =$$

$$= z_i^k + K_{ii}\frac{k_m}{\rho_m c_{p_m}}(\rho_c L + \rho_c c_{p_c} T_f) - K_{ii}(k_m T_f + (k_c - k_m)T_f) +$$

$$+ B_{ii}\frac{1}{\rho_m c_{p_m}}(\rho_c L + \rho_c c_{p_c} T_f) - B_{ii}T_f$$

from which

$$H_i^{k+1} = \frac{z_i^k + K_{ii}\left(\frac{k_m}{\rho_m c_{p_m}}(\rho_c L + \rho_c c_{p_c} T_f) - k_c T_f\right)}{\hat{M}_{ii} + C_{ii} + K_{ii}\frac{k_m}{\rho_m c_{p_m}} + B_{ii}\frac{1}{\rho_m c_{p_m}}} + \\ + \frac{B_{ii}\left(\frac{1}{\rho_m c_{p_m}}(\rho_c L + \rho_c c_{p_c} T_f) - T_f\right)}{\hat{M}_{ii} + C_{ii} + K_{ii}\frac{k_m}{\rho_m c_{p_m}} + B_{ii}\frac{1}{\rho_m c_{p_m}}}.$$

If H_i^k is greater than $val_{mushy/melt}$ then take the SOR step

$$H_i^{k+1} = H_i^k + \omega(H_i^{k+1} - H_i^k).$$

2. Iteration control

If $iter \leq itermax$ and $\|H^{k+1} - H^k\| > \varepsilon$ then goto 1; else stop.

3. End of Algorithm 5.1

In Algorithm 5.1 $\omega \in [1, 2]$ represents the over relaxation parameter. The relaxation is applied only if the enthalpy values H_i^{k+1} and H_i^k indicate that the point i remains in the same phase. This condition prevents the point i to skip the phase change interval and thus the latent heat.

The enthalpy is a primary unknown in Algorithm 5.1. The temperature can be calculated afterwards by using the equation (3.25). The free boundaries between the solid and mushy region, and mushy region and melt can be determined as isotherms of the enthalpy values $\rho_c c_{p_c} T_f$ and $\rho_c c_{p_c} T_f + \rho_c L$. In reality the mushy region does not appear in the Czochralski crystal growth process but the crystal-melt interface is sharp. For this reason we use the average of the values $\rho_c c_{p_c} T_f$ and $\rho_c c_{p_c} T_f + \rho_c L$ in order to determine the sharp crystal-melt interface.

In the following we present Algorithm 5.2. We concentrate on the numerical solution of the crystal-melt system governed by the transient Navier-Stokes and enthalpy equations. Special attention is paid to the solution of the Navier-Stokes equations in the whole domain by the variable viscosity method. The algorithm is similar at all time steps so we present it only for ith time step.

Algorithm 5.2

0. Initialization

Assumption: the enthalpy vector H and the velocity vector u have initial values from the previous time step.

1. Calculation of enthalpy and temperature

1.1 Enthalpy

Assemble the matrices and the vector presented in (5.4) for the enthalpy. Calculate the enthalpy from the equation (5.5) by using the velocity vector u and Algorithm 5.1.

1.2 Temperature

When enthalpy is known, calculate temperature according to the equation (3.25).

2. Calculation of velocity

2.1 Variable viscosity method

Consider the element e, $e \in [1, ..., \text{number of elements}]$, in the crystal-melt system. Define the characteristic element enthalpy H_{char} such that

$$H_{char}(i) = \begin{cases} 1, \text{ if } H(i) > \rho_c c_{p_c} T_f + \rho_c L \\ 0, \text{ otherwise} \end{cases},$$

$i = 1, ...,$ number of nodes in element e. Let ΔH be defined as an average value of the characteristic enthalpies of the element e. Then the element viscosity is

$$\mu_e(H) = \mu^* + B(1 - \Delta H),$$

where μ^* is the true viscosity and B some large value.

2.2 Velocity calculation

Applying the element viscosity μ_e, assemble the matrices and the vectors presented in (4.27) for velocity. Calculate velocity from the equation (4.25) by using temperature calculated above.

3. Crystal-melt interface

Calculate the melting point isotherm.

4. End of Algorithm 5.2

Remark 5.4 In Algorithm 5.2 the Navier-Stokes equations are calculated in the whole crystal. It would be sufficient, however, to limit consideration to some first layers of elements above the crystal-melt interface.

Remark 5.5 The basic idea of the variable viscosity method is shown in 2.1 in Algorithm 5.2. If all nodes in the element belong to the melt, then the characteristic viscosity of the element equals to the real viscosity. Otherwise the value of the characteristic viscosity is set high.

5.4 Numerical Examples

In the previous chapter we simulated numerically the silicon melt flow in the crucible. The surrounding parts of the melt, especially crystal, were not taken into

account. In this chapter we extend our numerical consideration to the crystal-melt system. The presence of the crystal influences considerably the physical phenomena in the melt. The crystal has an effect on heat transfer in the melt via the crystal-melt interface at which the latent heat is released. Furthermore, the crystal as a fixed or rotating object gives rise to variations in the melt flow.

The problem statement is presented mathematically in the beginning of this chapter (model (M4')) and semantically in Figure 3.4. The velocity field and the temperature distribution in the crystal-melt system are solved by using Algorithm 5.2. Physical parameters and dimensions of the crystal and the melt are shown in Table 5.1.

Quantity	Symbol	Value
Density of crystal	ρ_c	2490.0 kg/m^3
Density of melt	ρ_m	2490.0 kg/m^3
Heat capacity of crystal	c_{p_c}	900.0 J/kgK
Heat capacity of melt	c_{p_m}	1000.0 J/kgK
Heat conductivity of crystal	k_c	22.0 W/mK
Heat conductivity of melt	k_m	64.0 W/mK
Viscosity of melt	μ	$7.5 \cdot 10^{-4}$ kg/ms
Surface tension coeff.	γ_0	0.72 N/m
Temperature coeff. of surface tension	ϑ	$1.388 \cdot 10^{-4}$ $1/K$
Heat expansion coefficient	β	$1.4 \cdot 10^{-4}$ $1/K$
Reference temperature	T_0	1685.0 K
Gravity	g	9.82 m/s^2
Rotation rate of crystal	ω_c	$-4.0 - 8.0$ rpm
Rotation rate of melt	ω_m	$0.0 - 8.0$ rpm
Melting temperature	T_f	1685.0 K
Latent heat	L	$1.8 \cdot 10^6$ J/kg
Pulling velocity of crystal	$\vec{u}$	0.0 m/s
Heat transfer coeff.	α	40.0 W/m^2K
External temperature	T_{ext}	1185.0 K
Crystal radius		6.35 cm
Crystal height		20.0 cm
Melt radius		20.0 cm
Melt height		12.0 cm

Table 5.1 Physical parameters and dimensions of crystal and melt

We use quadrilateral finite elements (60×48 in the melt and 19×20 in the crystal) and the finite element mesh used in the simulations is shown in Figure 5.1.

In all simulations the SOR iteration is terminated when the relative error $\|H^k - H^{k-1}\|/\|H^k\|$ is less than 10^{-3}. The same limit causes termination of the Navier-Stokes iteration. The penalty parameter in the Navier-Stokes equation is chosen

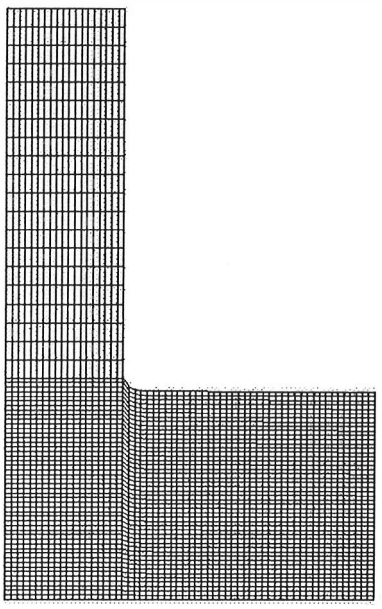

Figure 5.1 Finite element mesh in crystal-melt system

to be 10^{-7}. The time step is constant, $\Delta t = 0.1$ s. For the choice of the time step we refer to the discussion made in Chapter 4.4.3.

We begin the numerical examples with the simulation of the Grashof and Marangoni convections. The forced convections are neglected for a moment. The initial temperature is assumed to vary linearly in the z-direction between $T_f + 30$ and T_f in the melt and between T_f and $T_f - 160$ in the crystal. As in Chapter 4.4.3 we initialize the velocity field by computing the problem with the reduced Reynolds numbers ($\mu = 7.5 \cdot 10^{-2}$ for 0-5 seconds and $\mu = 7.5 \cdot 10^{-3}$ for 5-25 seconds). With the true Reynolds number the velocity field seems to find within 60 seconds a state where changes in the velocity field are very small (the difference between maximum velocities in consecutive time steps is $1.1 \cdot 10^{-5}$). In Figures 5.3a and 5.3b the temperature distributions and the velocity field of this state are shown. In the figures presenting the temperature fields (Figure 5.3a and the other corresponding figures below) we show the temperature distributions in the melt (grayscale) and in the crystal (contours between the temperatures T_f and $T_f - 160$) separately. In the figures depicting the velocity fields the free boundary between the crystal and melt is in addition shown.

The largest velocity values can be found near the melt-silica crucible wall. The maximum velocity is $|u| = 7.88$ cm/s. The Grashof and Marangoni convections together generate a main convection roll to the melt as was the case in the simu-

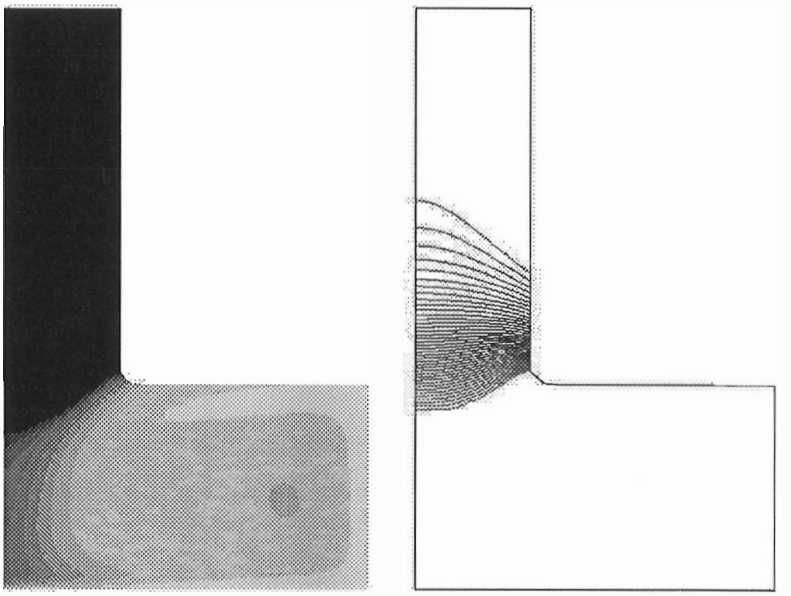

Figure 5.2a Temperature field induced by Grashof and Marangoni convections at $t = 85$ s

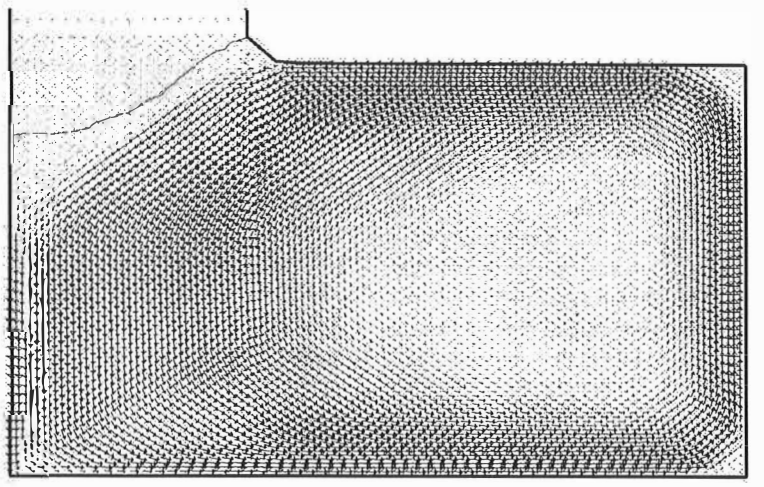

Figure 5.2b Velocity field induced by Grashof and Marangoni convections at $t = 85$ s

lation of the Grashof and Marangoni convections without the crystal.

Let us then take into account the rotation of the crystal. We begin the simulation with the initial guess achieved by the numerical simulation of the Grashof and Marangoni convections (at $t = 85$ s, Figures 5.2a and 5.2b). We simulate the crystal rotation in three parts each of which takes 15 seconds. During the first 15 seconds the rotation rate is 2 rpm, then we increase the rotation rate to 4 rpm and finally to 8 rpm. The numerical results are presented in Figures 5.3a-5.6b. We emphasize that the figures showing the melt flow are presented in the rz-plane.

The simulations indicate that the crystal rotation has a local effect on the melt flow field just under the crystal. Of course the time frame is very short and the situation can change after some time. Nevertheless, the main convection roll induced by the Grashof and Marangoni convections at least partially remains.

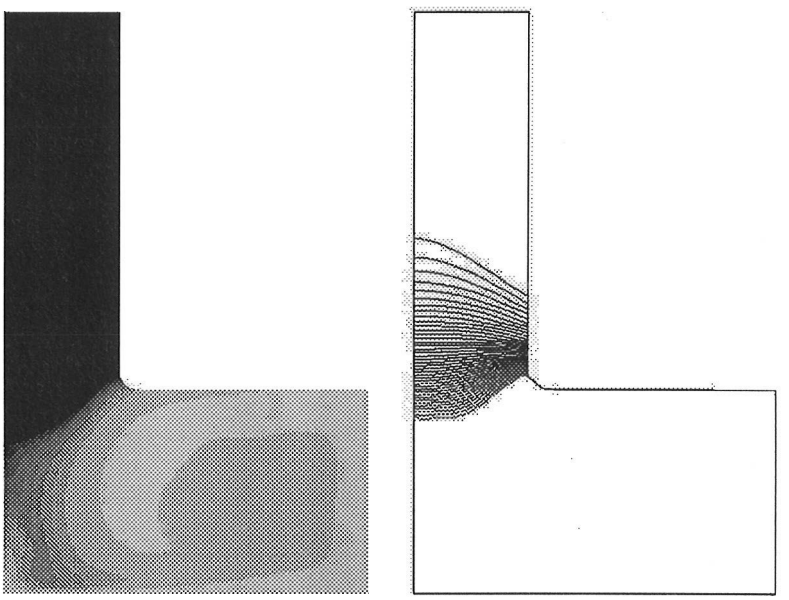

Figure 5.3a Temperature field induced by Grashof and Marangoni convections and rotation of crystal (2 rpm) at $t = 100$ s

Correspondingly, we simulate the rotation of the melt. The initial guess is again presented in Figures 5.2a and 5.2b (numerical simulation of the Grashof and Marangoni convections only). We proceed similarly as before: The rotation rate of the melt is increased gradually (first 15 seconds with 2 rpm, next 15 seconds with 4 rpm and finally 15 seconds with 8 rpm). The numerical results of the simulations are presented in Figures 5.7a-5.10b.

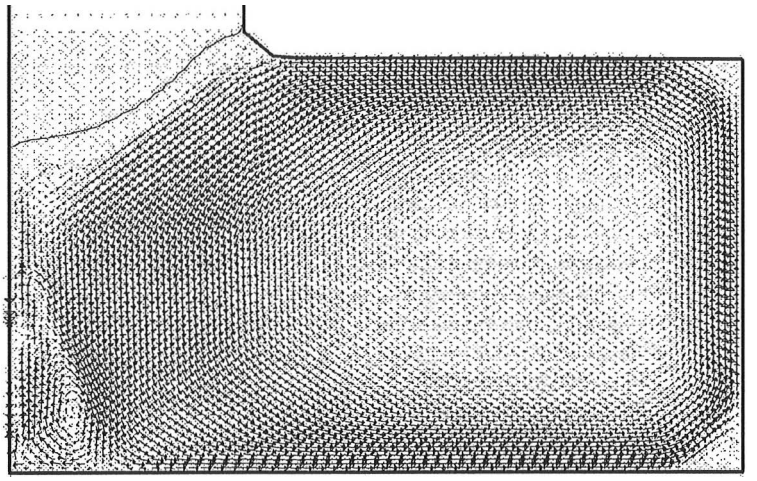

Figure 5.3b Velocity field induced by Grashof and Marangoni convections and rotation of crystal (2 rpm) at $t = 100$ s

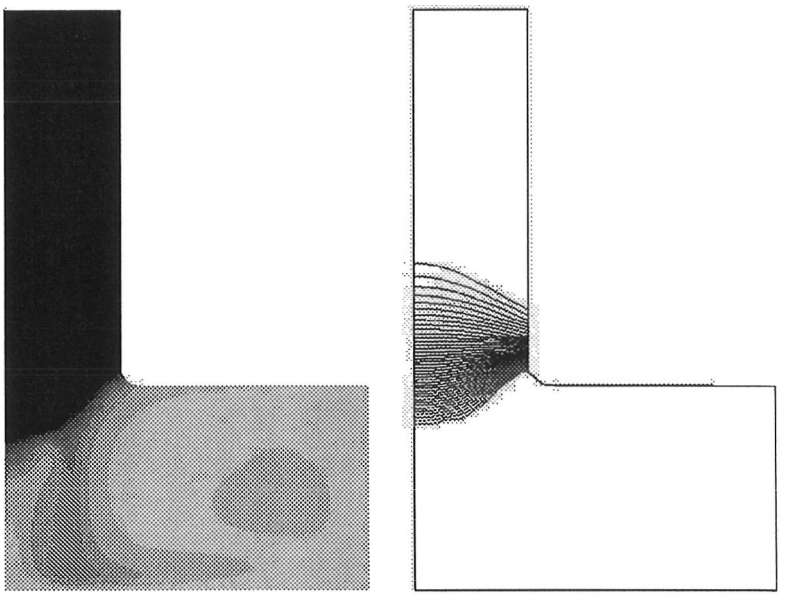

Figure 5.4a Temperature field induced by Grashof and Marangoni convections and rotation of crystal (4 rpm) at $t = 115$ s

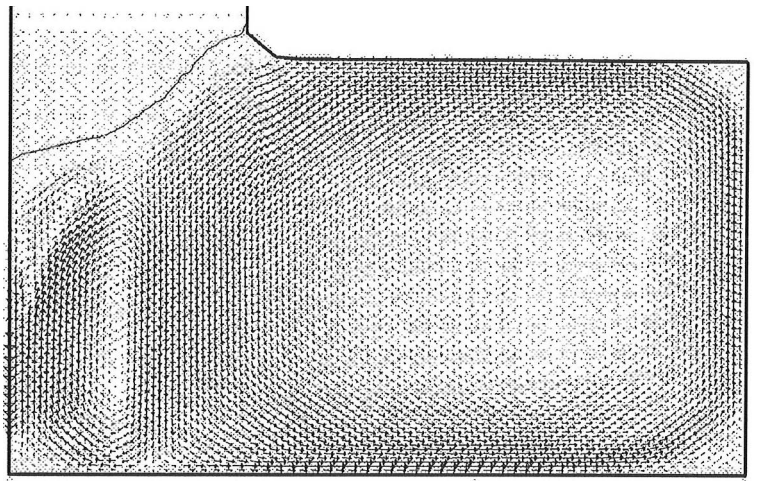

Figure 5.4b Velocity field induced by Grashof and Marangoni convections and rotation of crystal (4 rpm) at $t = 115$ s

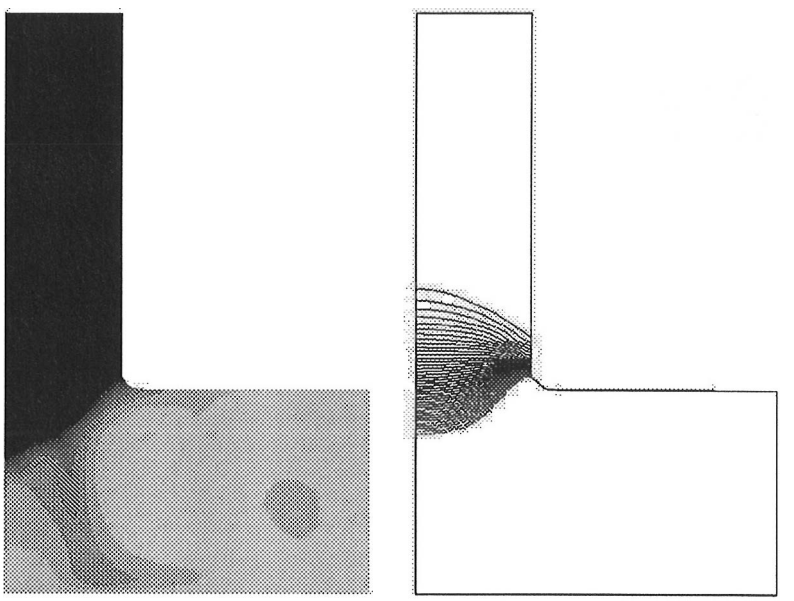

Figure 5.5a Temperature field induced by Grashof and Marangoni convections and rotation of crystal (8 rpm) at $t = 122.5$ s

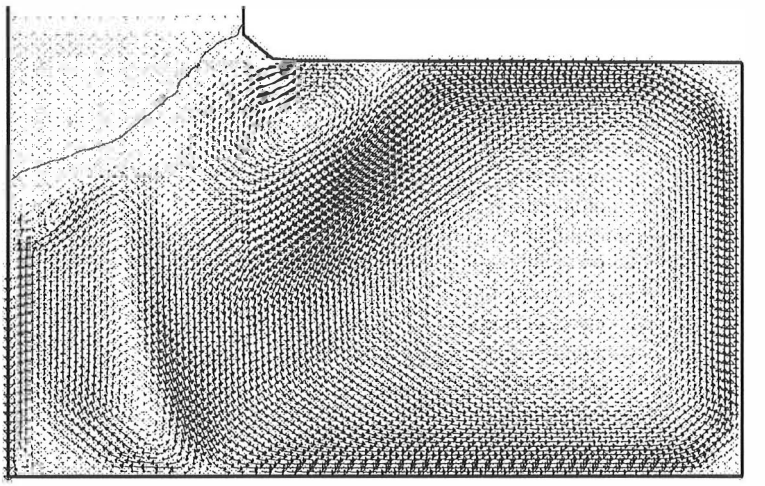

Figure 5.5b Velocity field induced by Grashof and Marangoni convections and rotation of crystal (8 rpm) at $t = 122.5$ s

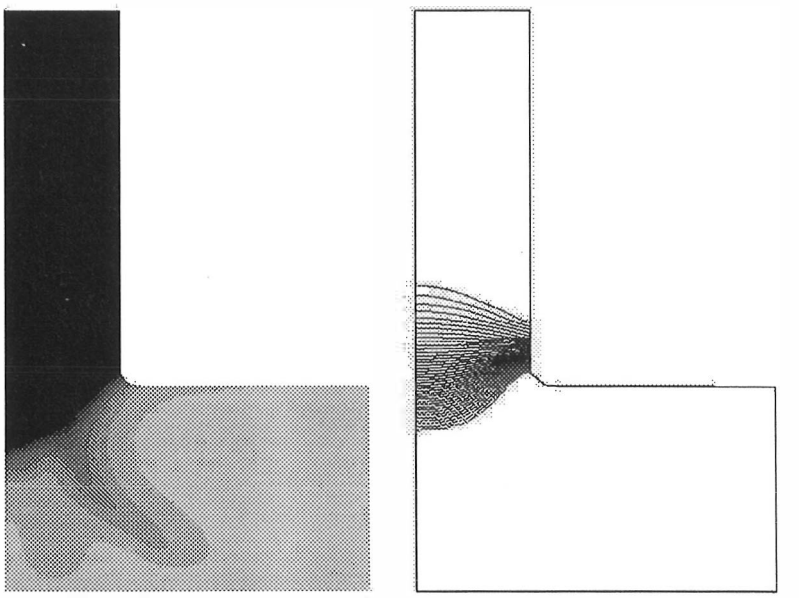

Figure 5.6a Temperature field induced by Grashof and Marangoni convections and rotation of crystal (8 rpm) at $t = 130$ s

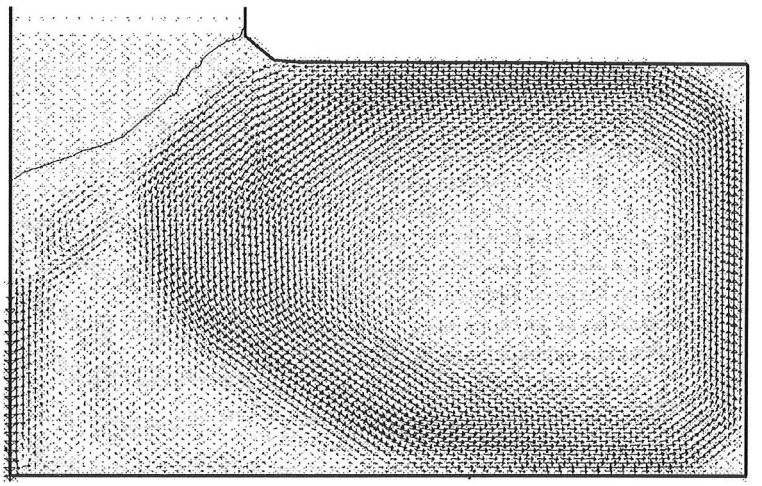

Figure 5.6b Velocity field induced by Grashof and Marangoni convections and rotation of crystal (8 rpm) at $t = 130$ *s*

We see that the main convection roll in the melt disappears. The number and position of smaller convection rolls vary in time. Although we did not start the flow simulation by taking advantage of the steady state temperature distribution in the crystal-melt system, it seems, that the transient effects are due to the rotation of the melt.

Next, we take into account all the convection mechanisms (Grashof and Marangoni convections, rotation of crystal and rotation of melt) We begin the simulation with the initial guess presented in Figures 5.10a and 5.10b (temperature and velocity fields induced by the Grashof and Marangoni convections and rotation of melt). We add the rotation of the crystal gradually into the system. We simulate the first 15 seconds with the crystal rotation rate of -2 rpm. After this we simulate another 15 seconds with the rotation rate of -4 rpm. The numerical results from these simulations are shown in Figures 5.11a-5.13c. The pressure fields are shown after each phase of the crystal rotation is completed. The pressure fields are again quite satisfactory, i.e., the checkerboard patterns do not appear.

Remark 5.6 As we mentioned in Chapter 5.3, we define the position of the crystal-melt interface as an average of the values $\rho_c c_{p_c} T_f$ and $\rho_c c_{p_c} T_f + \rho_c L$. In the mushy region the viscosity of the liquid grows rapidly from the value of silicon to a large value due to the use of the variable viscosity method, and the velocity field is forced to zero. Typically the width of the mushy region is from 2 to 4 elements depending on the element mesh.

Remark 5.7 In the numerical analysis presented in this chapter we assumed that the crystal radius is constant. We did not either control the position of the three-

phase point, i.e., it could move freely along the fixed crystal-gas and melt-gas interfaces. The position of the three-phase point can be controlled, such that it joins exactly to the intersection of the crystal-gas and melt-gas interfaces, by setting the appropriate values to the boundary conditions of the function $\Phi(H)$.

Remark 5.8 When using the penalty method together with bilinear velocity-constant pressure approximation, we have to evaluate an integral containing a term u_r/r (in the variational formulation of u_r, equation (4.16)) with one point Gaussian integration rule. This causes numerical approximation error and may lead to problems near the symmetry axis, see Figures 5.5b and 5.6b. We have compared our numerical results to those achieved by a commercial fluid dynamics package FIDAP. When modeling the coupled heat and Navier-Stokes equations in the axisymmetric geometry the same results were obtained with both numerical simulation tools, and problems near the symmetry axis occured. The same behavior with the integrated method was not encountered.

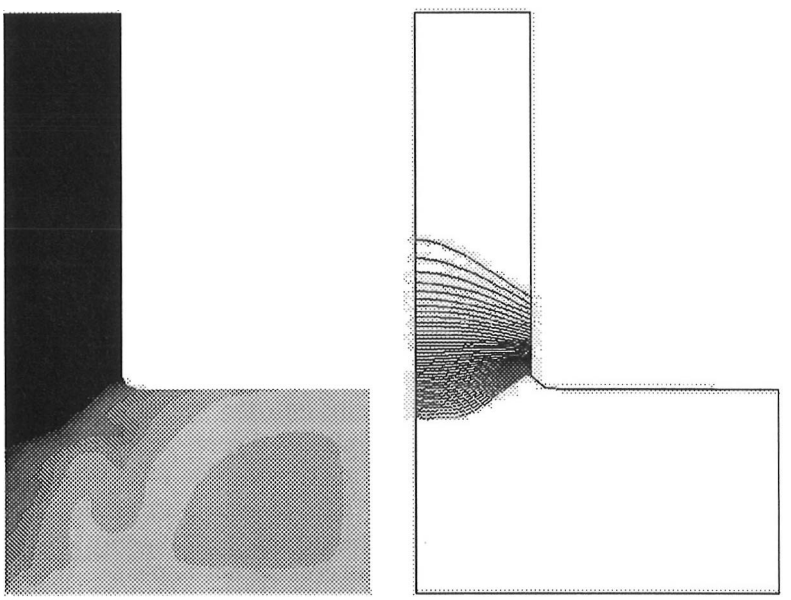

Figure 5.7a Temperature field induced by Grashof and Marangoni convections and rotation of melt (2 rpm) at $t = 100$ *s*

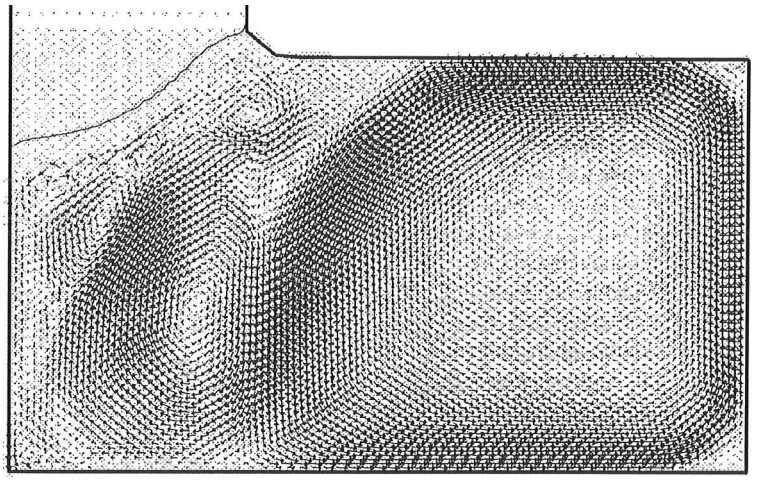

Figure 5.7b Velocity field induced by Grashof and Marangoni convections and rotation of melt (2 rpm) at $t = 100$ *s*

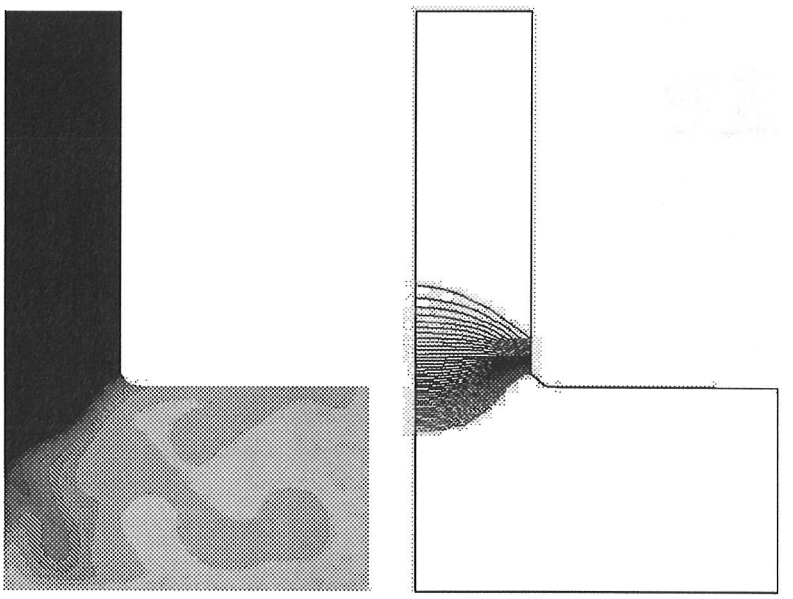

Figure 5.8a Temperature field induced by Grashof and Marangoni convections and rotation of melt (4 rp) at $t = 115$ *s*

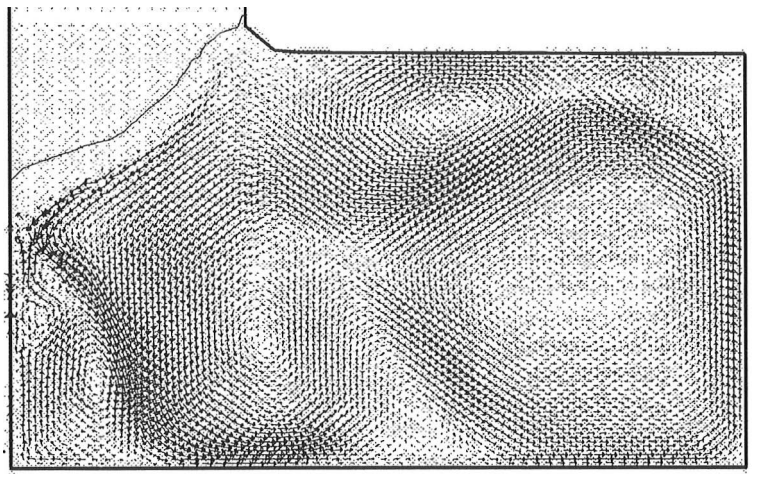

Figure 5.8b Velocity field induced by Grashof and Marangoni convections and rotation of melt (4 rpm) at $t = 115$ s

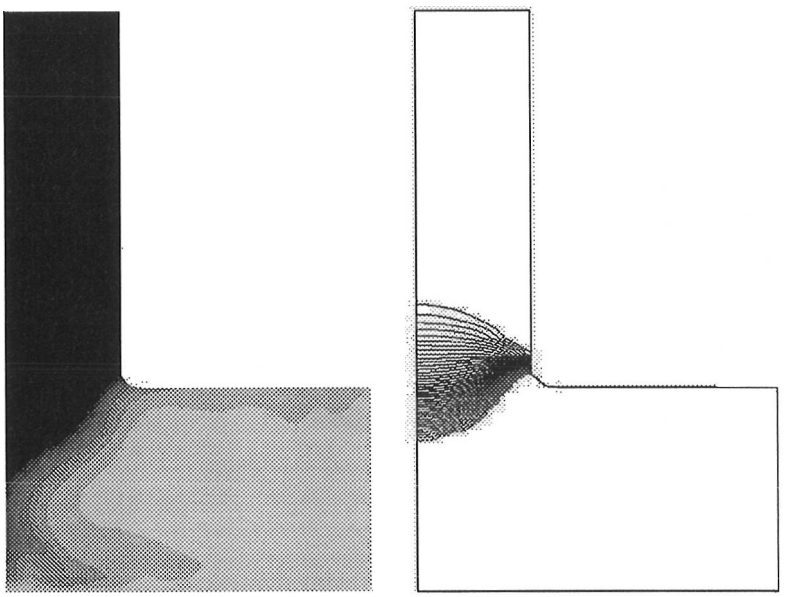

Figure 5.9a Temperature field induced by Grashof and Marangoni convections and rotation of melt (8 rpm) at $t = 122.5$ s

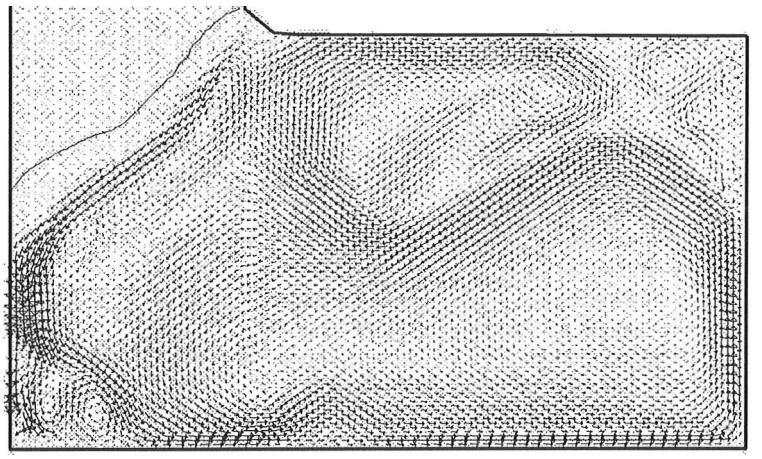

Figure 5.9b Velocity field induced by Grashof and Marangoni convections and rotation of melt (8 rpm) at $t = 122.5$ *s*

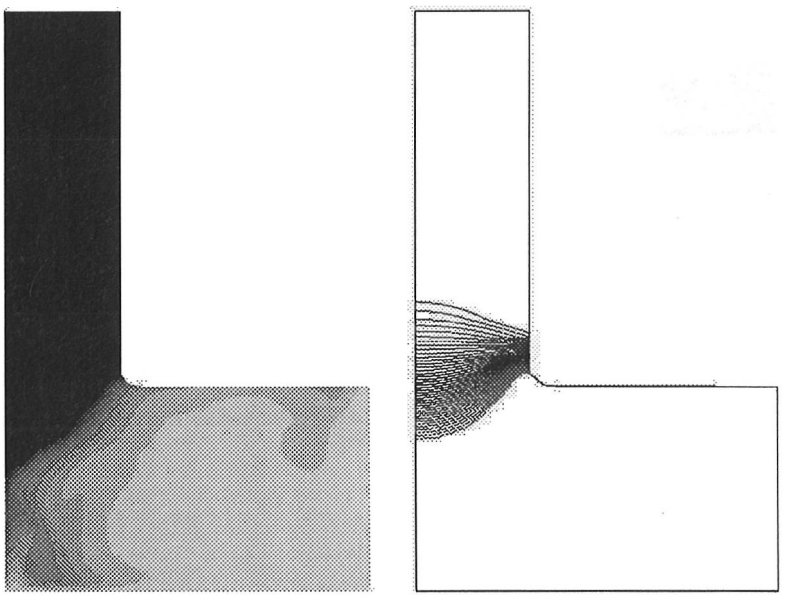

Figure 5.10a Temperature field induced by Grashof and Marangoni convections and rotation of melt (8 rpm) at $t = 130$ *s*

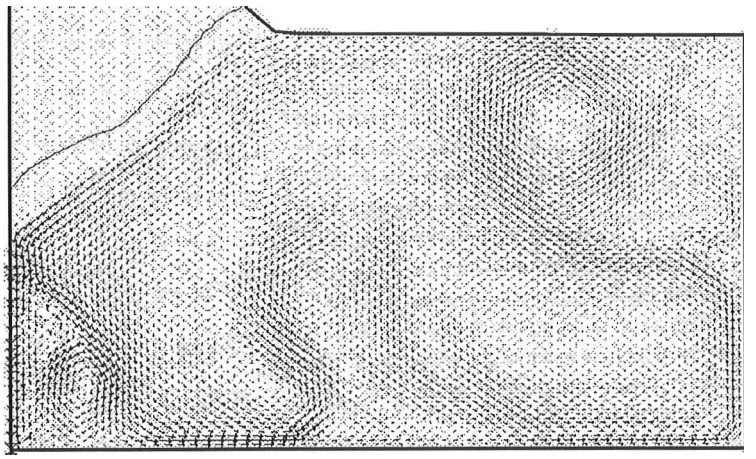

Figure 5.10b Velocity field induced by Grashof and Marangoni convections and rotation of melt (8 rpm) at $t = 130$ s

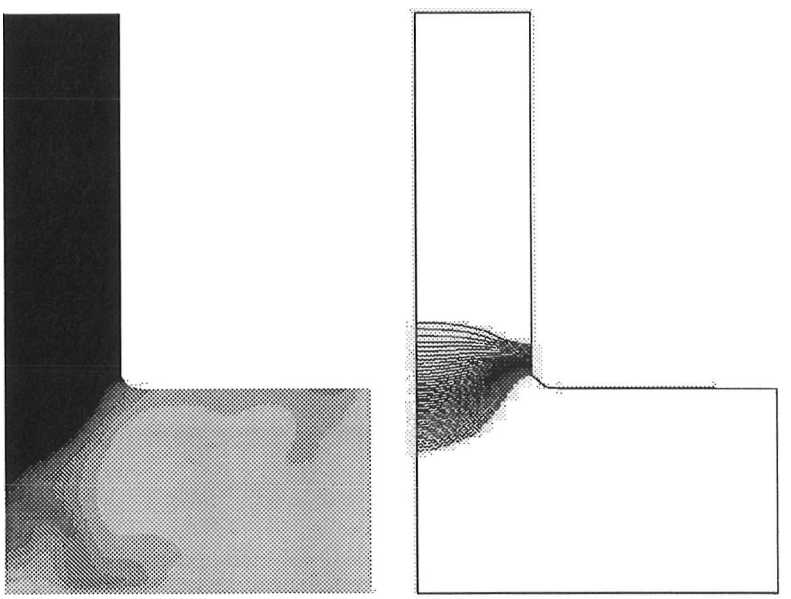

Figure 5.11a Temperature field induced by Grashof and Marangoni convections and rotation of crystal and melt (-2 and 8 rpm) at $t = 145$ s

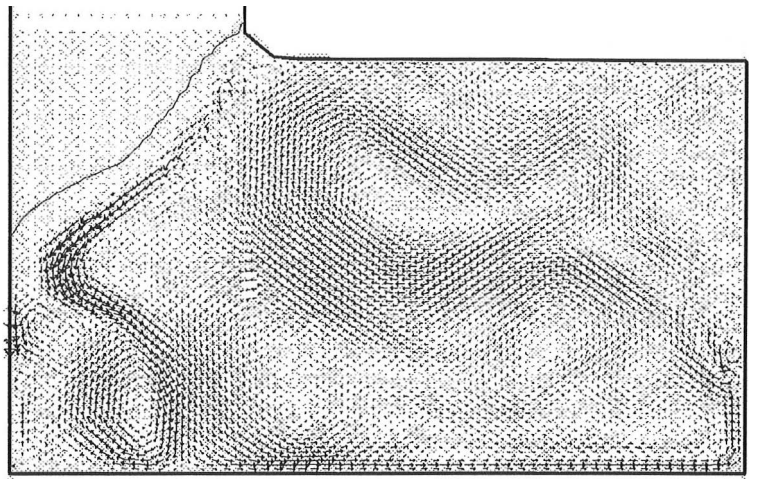

Figure 5.11b Velocity field induced by Grashof and Marangoni convections and rotation of crystal and melt (-2 and 8 rpm) at $t = 145$ *s*

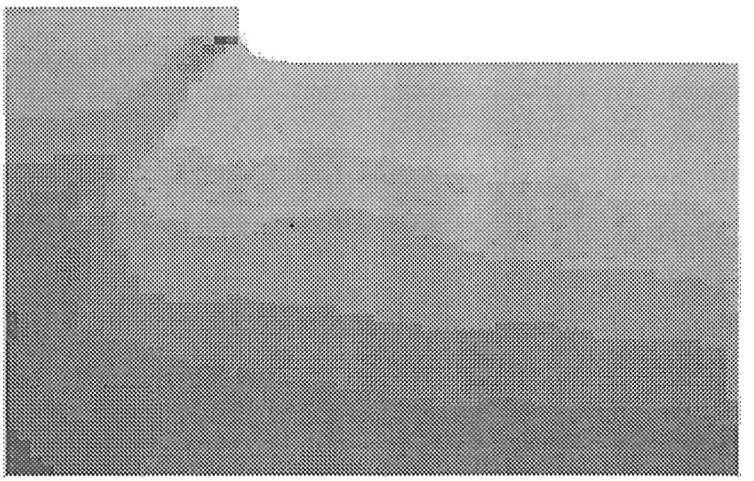

Figure 5.11c Pressure field induced by Grashof and Marangoni convections and rotation of crystal and melt (-2 and 8 rpm) at $t = 145$ *s*

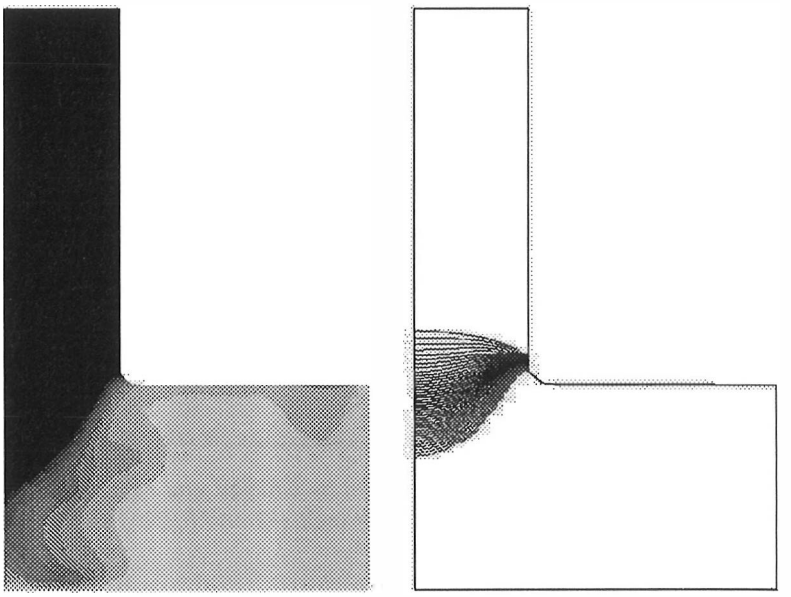

Figure 5.12a Temperature field induced by Grashof and Marangoni convections and rotation of crystal and melt (-4 and 8 rpm) at $t = 152.5$ *s*

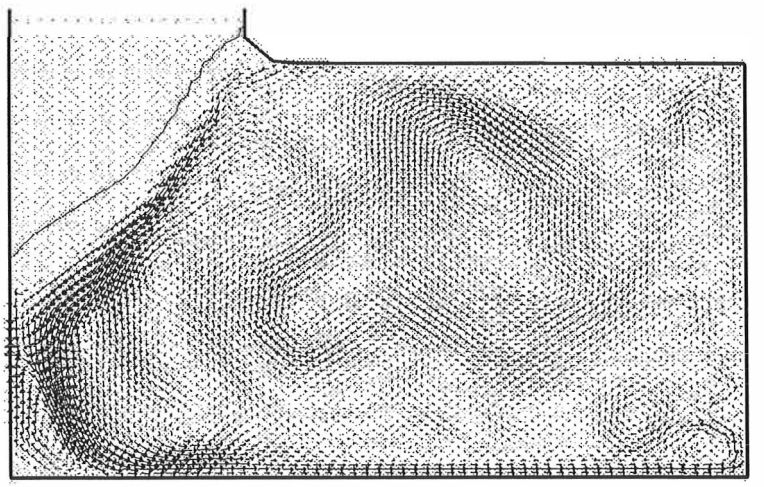

Figure 5.12b Velocity field induced by Grashof and Marangoni convections and rotation of crystal and melt (-4 and 8 rpm) at $t = 152.5$ *s*

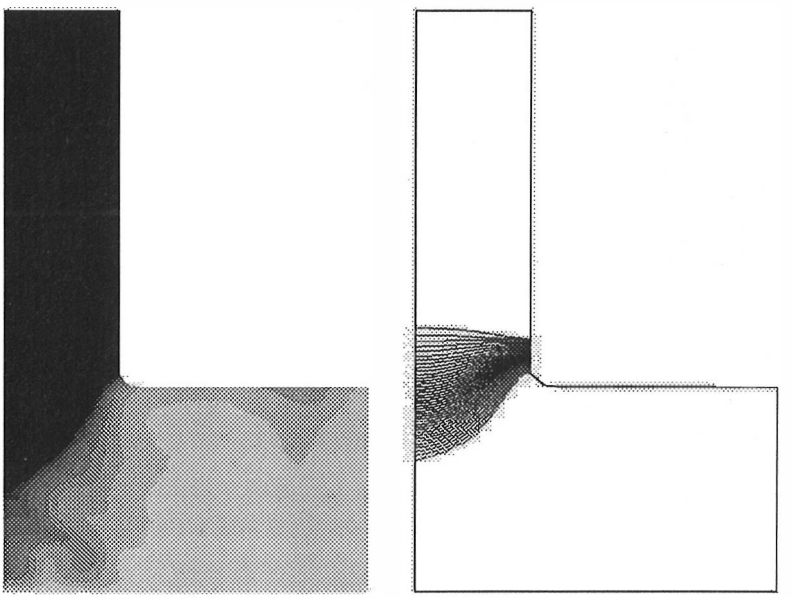

Figure 5.13a Temperature field induced by Grashof and Marangoni convections and rotation of crystal and melt (-4 and 8 rpm) at $t = 160$ *s*

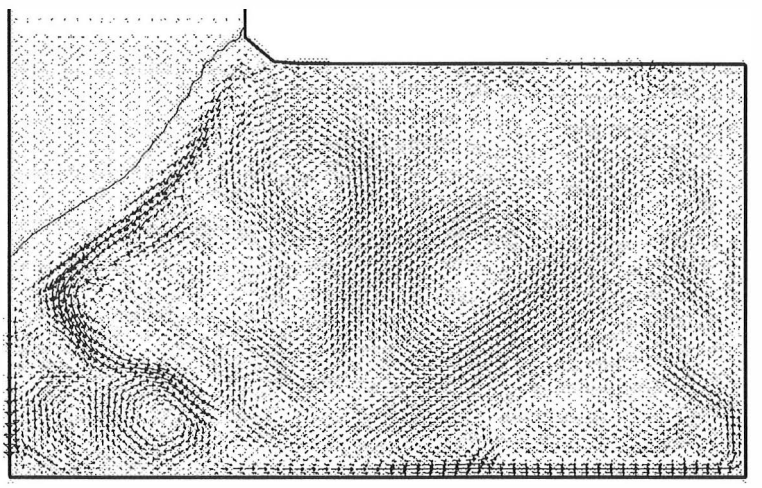

Figure 5.13b Velocity field induced by Grashof and Marangoni convections and rotation of crystal and melt (-4 and 8 rpm) at $t = 160$ *s*

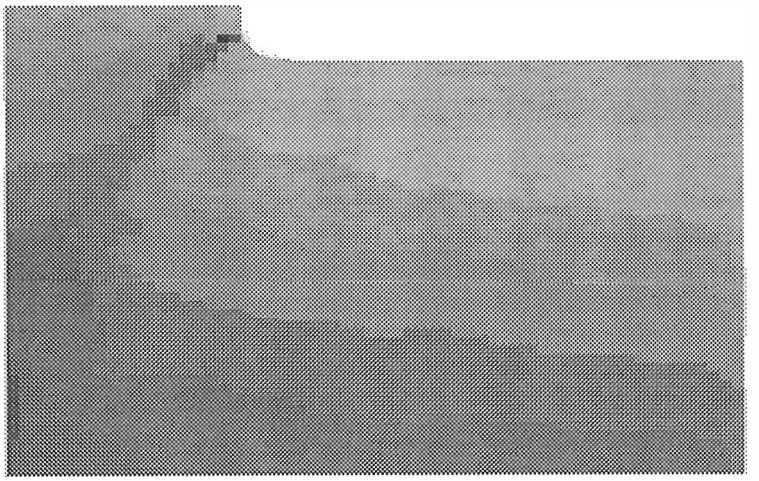

Figure 5.13c Pressure field induced by Grashof and Marangoni convections and rotation of crystal and melt (-4 and 8 rpm) at $t = 160$ *s*

6. Simulation of Czochralski Crystal Growth with Diffuse-Gray Radiation

The numerical simulations in the previous chapters were carried out either in the melt or in the crystal-melt geometry. Although the simulations characterized important physical phenomena existing in the melt and crystal they did not include thermal information from exterior. In this chapter we simulate numerically the Czochralski silicon crystal growth in the real geometry where radiation is taken into account. In the numerical simulations we take, however, advantage of the numerical tools derived for the crystal-melt system.

We begin with the mathematical model (M5) presented in Chapter 3.3. In the course of the numerical simulations we are going to use the variable viscosity method in the crystal and melt as in the previous chapter. For this reason the modified mathematical model of (M5) is introduced: Find the velocity vector $\vec{u} = (u_r, u_z, u_\theta)$ and the pressure p in $(\Omega_m \cup \Omega_c) \times (0, t_0)$, and the enthalpy $\tilde{H}$ in $\Omega = (\Omega_m \cup \Omega_c \cup \Omega_s \cup \Omega_g \cup \Omega_h \cup \Omega_a \cup \Omega_t) \times (0, t_0)$ such that (M5')

$$
\begin{cases}
\rho_m \dfrac{\partial u_r}{\partial t} - \dfrac{\partial \sigma_{zr}}{\partial z} - \dfrac{1}{r}\dfrac{\partial}{\partial r}(r\sigma_{rr}) + \dfrac{1}{r}\sigma_{\theta\theta} + \rho_m\left(u_r\dfrac{\partial u_r}{\partial r} + u_z\dfrac{\partial u_r}{\partial z} - \dfrac{u_\theta^2}{r}\right) = 0 \\
\rho_m \dfrac{\partial u_z}{\partial t} - \dfrac{\partial \sigma_{zz}}{\partial z} - \dfrac{1}{r}\dfrac{\partial}{\partial r}(r\sigma_{zr}) + \rho_m\left(u_r\dfrac{\partial u_z}{\partial r} + u_z\dfrac{\partial u_z}{\partial z}\right) = \\
\qquad = \rho_m g\beta(T - T_0) \\
\rho_m \dfrac{\partial u_\theta}{\partial t} - \dfrac{1}{r^2}\dfrac{\partial}{\partial r}(r^2\sigma_{r\theta}) - \dfrac{\partial \sigma_{\theta z}}{\partial z} + \rho_m\left(u_r\dfrac{\partial u_\theta}{\partial r} + u_z\dfrac{\partial u_\theta}{\partial z} + \dfrac{u_r u_\theta}{r}\right) = 0 \\
\dfrac{1}{r}\dfrac{\partial}{\partial r}(ru_r) + \dfrac{\partial u_z}{\partial z} = 0
\end{cases}
$$

in $(\Omega_m \cup \Omega_c) \times (0, t_0)$,

$$
\frac{\partial}{\partial t}\tilde{H} + \vec{u}\cdot\nabla\tilde{H} - \frac{1}{r}\frac{\partial}{\partial r}\left(r\frac{\partial}{\partial r}\hat{k}T(\tilde{H})\right) - \frac{\partial}{\partial z}\left(\frac{\partial}{\partial z}\hat{k}T(\tilde{H})\right) = \hat{f}
$$

in $\Omega \times (0, t_0)$ with the initial and boundary conditions

$$
\begin{cases}
\vec{u}(r, z, 0) = \vec{u}^0(r, z) & \text{in } \Omega_m \cup \Omega_c \\
\tilde{H}(r, z, 0) = \tilde{H}^0(r, z) & \text{in } \Omega
\end{cases}
$$

$$
\begin{cases}
u_r = 0, \ \dfrac{\partial u_z}{\partial r} = 0, \ u_\theta = 0, & \text{on } (\Gamma_s \cap (\Omega_m \cup \Omega_c)) \times (0, t_0) \\
\dfrac{\partial T(\tilde{H})}{\partial r} = 0 & \text{on } \Gamma_s \times (0, t_0) \\
u_r = 0, \ u_z = 0, \ u_\theta = \omega_m r & \text{on } \Gamma_m \times (0, t_0) \\
\vec{u} \cdot \vec{n} = 0, \ \sigma_n = \dfrac{\gamma_0}{R} - p_a, \ \sigma_\tau = -\vartheta \gamma_0 \dfrac{\partial T(\tilde{H})}{\partial \tau} & \text{on } \Gamma_{mg} \times (0, t_0) \\
u_r = 0, \ u_z = 0, \ u_\theta = \omega_c r & \text{on } \Gamma_{cg} \times (0, t_0) \\
-\hat{k} \dfrac{\partial T(\tilde{H})}{\partial n} = G(\hat{\sigma}(T(\tilde{H}))^4) & \text{on } (\Gamma_{mg} \cup \Gamma_{cg} \cup \Gamma_i) \times (0, t_0) \\
-\hat{k} \dfrac{\partial T(\tilde{H})}{\partial n} = \hat{\alpha}(T(\tilde{H}) - T_{ext}) & \text{on } \Gamma_o \times (0, t_0) \\
\tilde{H} = \tilde{H}_e & \text{on } \Gamma_e \times (0, t_0)
\end{cases}
$$

+ transmission conditions $\hat{k}_i \frac{\partial T_i(\tilde{H})}{\partial n} = \hat{k}_j \frac{\partial T_j(\tilde{H})}{\partial n}$, $i \neq j$, on the common boundaries of two different materials.

The only differences between the mathematical model (M5') and the model (M4') introduced for the crystal-melt system are the presence of the radiation boundary condition imposed on $\Gamma_{mg} \cup \Gamma_{cg} \cup \Gamma_i$ and the enthalpy equation determined in the whole domain Ω. The Navier-Stokes equations and velocity/stress boundary conditions stand as they are in the model (M4').

The variational formulation and the finite element discretization of the Navier-Stokes equations were derived in Chapters 4.1.2 and 4.2 and we refer from these parts therein (see also Remark 5.3). We emphasize that the shape of the melt-gas interface is based on the analytical representation of the shape of the meniscus presented by Hurle. Therefore we can neglect the boundary condition $\sigma_n = \frac{\gamma_0}{R} - p_a$ on Γ_{mg}.

The variational formulation and the finite element discretization for the enthalpy equation are derived in Chapters 6.1 and 6.2. On the internal boundary the boundary condition for enthalpy contains an infinite dimensional Gebhart factor G (see Chapter 3.3). In the finite element analysis a finite dimensional equivalent of the Gebhart factor is achieved by introducing a view factor

$$
F_{ij} = \frac{1}{|A_i|} \int_{A_i} \int_{A_j} \frac{\vec{n}_i \cdot (\vec{x}_j - \vec{x}_i) \vec{n}_j \cdot (\vec{x}_i - \vec{x}_j)}{\pi |\vec{x}_i - \vec{x}_j|^4} \Xi(\vec{x}_i, \vec{x}_j) \ dA_i dA_j, \tag{6.1}
$$

and replacing the integral operator K in the equation (3.35) with this factor. In (6.1) A_i and A_j represent the element surface areas, $\vec{x}_i \in A_i$, $\vec{x}_j \in A_j$ and $\vec{n}_i$ and $\vec{n}_j$ are the corresponding outward unit normals. $\Xi(\vec{x}_i, \vec{x}_j)$ is the visibility factor. The numerical computation of the view factors in axisymmetric geometry is discussed briefly in Chapter 6.3. In Chapter 6.4 the numerical examples for the entire Czochralski system are presented.

6.1 Variational formulation

In the following the variational formulation for the enthalpy equation in (M5') is derived.

Let a test function $v \in \{w \in L_r^2(\Omega) | \frac{\partial w}{\partial r}, \frac{\partial w}{\partial z} \in L_r^2(\Omega)\} \cap L_r^5(\Gamma_{mg} \cup \Gamma_{cg} \cup \Gamma_i)$, where $\Omega = \Omega_m \cup \Omega_c \cup \Omega_s \cup \Omega_g \cup \Omega_h \cup \Omega_a \cup \Omega_t$ and $L_r^p(D) = \{w | \int_D |w(r,z)|^p r \; dr dz < \infty\}$. If we multiply the enthalpy equation by the test function v, observe the weight r, integrate over the region Ω, use Green's theorem and apply the boundary conditions stated in (M5') we get

$$
\begin{aligned}
&\int_\Omega \frac{\partial}{\partial t}\tilde{H} v r \; d\Omega + \int_\Omega (\vec{u} \cdot \nabla \tilde{H}) v r \; d\Omega + \int_\Omega \hat{k} \left(\nabla T(\tilde{H}) \cdot \nabla v \right) r \; d\Omega + \\
&+ \int_{\Gamma_{mg} \cup \Gamma_{cg} \cup \Gamma_i} G(\hat{\sigma}(T(\tilde{H}))^4) v r \; dS + \int_{\Gamma_o} \hat{\alpha} T(\tilde{H}) v r \; dS = \\
&= \int_\Omega \hat{f} v r \; d\Omega + \int_{\Gamma_o} \hat{\alpha} T_{ext} v r \; dS.
\end{aligned} \tag{6.2}
$$

6.2 Petrov-Galerkin Finite Element Approximation

We approximate the enthalpy as a linear combination of the basis functions such that

$$
\tilde{H} = \sum_{j=1}^{n} \tilde{H}_j \varphi_j, \tag{6.3}
$$

where $\tilde{H}_j \in \mathbb{R}$ is the value of the enthalpy depending on time t. The substitution of the linear combination (6.3) into the variational formulation (6.2) and the replacement of the test function v with the basis functions produce an algebraic system for $\tilde{H}$:

$$
M^H \frac{\partial \tilde{H}}{\partial t} + C^H \tilde{H} + K^H T(\tilde{H}) + G^H T^4(\tilde{H}) + B T(\tilde{H}) = F_1^H + F_2^H, \tag{6.4}
$$

where the submatrices and vectors are

$$
\begin{aligned}
M^H(i,j) &= \int_{\Omega_m \cup \Omega_c} \hat{\varphi}_i \varphi_j r \, d\Omega, \\
C^H(i,j) &= \int_{\Omega_m \cup \Omega_c} \hat{\varphi}_i \, (\vec{u} \cdot \nabla \varphi_j) \, r \, d\Omega, \\
K^H(i,j) &= \int_{\Omega_m \cup \Omega_c} \hat{k} \, (\nabla \varphi_i \cdot \nabla \varphi_j) \, r \, d\Omega, \\
B^H(i,j) &= \int_{\Gamma_o} \hat{\alpha} \varphi_i \varphi_j r \, dS, \\
F_1^H(i) &= \int_{\Omega} \hat{f} \varphi_i r \, d\Omega, \\
F_2^H(i) &= \int_{\Gamma_o} \hat{\alpha} T_{ext} \varphi_i r \, dS
\end{aligned}
\tag{6.5}
$$

$i, j = 1, \ldots, n$. As in Chapters 4.2 and 5.2 the mass matrix and the convection matrix contain modified basis function $\hat{\varphi}_i$ originating from the streamline upwinding/Petrov-Galerkin technique. The matrix G^H is considered in more details in the following chapter.

6.3 View Factors

Computation of radiation inside of the Czochralski furnace requires a determination of the view factors between various surfaces in the system. The view factor F_{ij} represented in (6.1) is equal to the fraction of energy leaving a surface i which reaches a surface j. In axisymmetric geometry surfaces are cutted cones (in certain cases also cylinders or planes) which are generated by rotating two dimensional element boundaries around the symmetry axis. By taking into account the rotational symmetry we get

(6.6)

$$
\begin{aligned}
F_{ij} &= \frac{1}{|A_i|} \int_{A_i} \int_{A_j} \frac{\vec{n}_i \cdot (\vec{x}_j - \vec{x}_i) \vec{n}_j \cdot (\vec{x}_i - \vec{x}_j)}{\pi |\vec{x}_i - \vec{x}_j|^4} \quad \Xi(\vec{x}_i, \vec{x}_j) \; dA_i dA_j \\
&= \frac{2}{|A_i|} \int_{\Gamma_i} r_i \int_{A_j} \frac{\vec{n}_i(\theta_i) \cdot (\vec{x}_j - \vec{x}_i) \vec{n}_j \cdot (\vec{x}_i - \vec{x}_j)}{|\vec{x}_i - \vec{x}_j|^4} \quad \Xi(\vec{x}_i, \vec{x}_j) \; dA_j d\Gamma_i \\
&= \frac{2}{|A_i|} \int_{\Gamma_i} r_i \int_{\Gamma_j} r_j \int_0^{2\pi} \frac{\vec{n}_i(\theta_i) \cdot (\vec{x}_j - \vec{x}_i) \vec{n}_j(\theta_j) \cdot (\vec{x}_i - \vec{x}_j)}{|\vec{x}_i - \vec{x}_j|^4} \quad \Xi(\vec{x}_i, \vec{x}_j) \; d\theta_j d\Gamma_j d\Gamma_i.
\end{aligned}
$$

Here Γ_i is the cross section of A_i on the rz-plane. For simplicity we can assume that $\theta_i = 0$.

The computer program which computes the view factors was developed at the Center for Scientific Computing by Mr. J. Katajamäki. The implementation

includes the determination of the visibility factor in the axisymmetric Czochralski geometry and the numerical integration of the view factors. The integration is based on the Stokes theorem and the integrals are evaluated numerically by using the Gaussian integration points. For further details we refer to [Katajamäki93].

Let us assume that the surface $\Gamma_{mg} \cup \Gamma_{cg} \cup \Gamma_i$ is decomposed into N disjoint subsets Σ_i such that $\Gamma_{mg} \cup \Gamma_{cg} \cup \Gamma_i = \cup_{i=1}^{N} \Sigma_i$, and the view factors between these subsets are known.

By replacing the integral operator K with the view factor F in the definition of the Gebhart factor (equation (3.35)) , we get a finite dimensional equivalent of the radiation operator. Thus in the discrete case

$$G^d = (I - F)(I - (I - E)F)^{-1}E, \tag{6.7}$$

where E is a diagonal matrix containing the surface emissivities.

Let us then take a closer look at the surface integral containing the factor G in the variational formulation (6.2). It can be replaced with

$$\begin{aligned} &\int_{\Gamma_{mg} \cup \Gamma_{cg} \cup \Gamma_i} G(\hat{\sigma}(T(\tilde{H}))^4) vr \; dS = \sum_{i=1}^{N} \int_{\Sigma_i} G(\hat{\sigma}(T(\tilde{H}))^4) vr \; dS = \\ &\approx \sum_{i=1}^{N} \int_{\Sigma_i} vr \sum_{k=1}^{N} \int_{\Sigma_k} G^d_{ki} \hat{\sigma}(T(\tilde{H}))^4 \; dS \; dS \end{aligned} \tag{6.8}$$

$k = 1, ..., N$. We emphasize that the function $T(\tilde{H})$ represents the value of the temperature of the surface k.

We construct in the following the matrix G^H. The numerical integration produces

$$G^H(i,j) = \sum_{k=1}^{N} \sum_{g \in I} \omega_g v(N_i) r(N_i) G^d_{ki} \hat{\sigma} \overline{(T(\tilde{H})}(N_j))^4,$$

where I is the set of indices for the finite element nodes N_k, $k = 1, ..., M$ and $\overline{T(\tilde{H})}$ is the mean value of the nodal temperatures on Σ_k. That is, we apply trapezoidal rule and one point Gaussian integration rule for integrals taken over Σ_i and Σ_k, respectively.

6.4 Numerical Examples

In the following we put together the discretized equations governing heat transfer in the entire Czochralski furnace and melt flow, after which the solution methods of the discretized equations are discussed.

The finite element discretization of the Navier-Stokes and enthalpy equations in (M5') produces the matrix equations (see Chapters 4.2 and 6.3)

$$
\begin{aligned}
M^u \frac{\partial u_r}{\partial t} + A_{rr}u_r + A_{rz}u_z + A_{r\theta}u_\theta &= -G_r^u + D_r^u \\
M^u \frac{\partial u_z}{\partial t} + A_{zr}u_r + A_{zz}u_z &= F^u - G_z^u + D_z^u, \\
M^u \frac{\partial u_\theta}{\partial t} + A_{\theta r}u_r + A_{\theta z}u_z + A_{\theta\theta}u_\theta &= D_\theta^u, \\
M^H \frac{\partial \tilde{H}}{\partial t} + C^H \tilde{H} + K^H T(\tilde{H}) + G^H T^4(\tilde{H}) + BT(\tilde{H}) &= F_1^H + F_2^H.
\end{aligned}
$$

Here the matrices D_r^u, D_z^u and D_θ^u contain the Dirichlet data.

The matrix equations for the velocity components are applied in the crystal and melt whereas the matrix equation for the enthalpy is applied in the entire geometry. We emphasize that the velocity field is computed by using the variable viscosity method (Algorithm 5.2 in Chapter 5.3). The discretized Navier-Stokes equations are nonlinear and the nonlinearity caused by convection is treated by the Newton's method (Chapter 4.3). The pressure is eliminated from the Navier-Stokes equations by the penalty method. The velocity field depends on temperature. At each time step we uncouple the computation of velocity and enthalpy, and the temperature field is computed afterwards from the values of enthalpy. The enthalpy is solved by the SOR-method, and in the crystal and melt Algorithm 5.1 (presented in Chapter 5.3) is applied.

We discretize the Navier-Stokes equations by the backward Euler method in time. The time discretization of the enthalpy equation is handled semi-implicitly so that the radiation part is taken from the previous time step.

In the submatrices containing the convection terms the modified basis functions proposed by Brooks and Hughes are used. The linearization of the discretized Navier-Stokes equations and the decoupling from the temperature produce a linear matrix equation for the velocity which is solved by the Gaussian elimination. For the enthalpy the SOR iteration at each time step is terminated when the relative error is less than 10^{-3}. The limit 10^{-2} for the relative error of velocity causes the termination of the Navier-Stokes iteration. The penalty parameter in the Navier-Stokes equation is chosen to be 10^{-7}. At each time step the uncoupled problem is solved only once.

In the Czochralski silicon crystal growth every material is characterized by the different thermophysical properties which are listed in Table 6.1. In Table 6.2 the details of the Czochralski construction used in this chapter are explained.

Quantity	Value
Density of crystal	2490.0 kg/m^3
Density of melt	2490.0 kg/m^3
Density of silica crucible	2200.0 kg/m^3
Density of graphite	1600.0 kg/m^3
Density of felt	100.0 kg/m^3
Heat capacity of crystal	900.0 J/kgK
Heat capacity of melt	1000.0 J/kgK
Heat capacity of silica crucible	1300.0 J/kgK
Heat capacity of graphite	2100.0 J/kgK
Heat capacity of felt	1010.0 J/kgK
Heat conductivity of crystal	22.0 W/mK
Heat conductivity of melt	64.0 W/mK
Heat conductivity of silica crucible	6.0 W/mK
Heat conductivity of graphite	60.0 W/mK
Heat conductivity of felt	0.4 W/mK
Emissivity of crystal	0.7
Emissivity of melt	0.3
Emissivity of silica crucible	0.35
Emissivity of graphite	0.8
Emissivity of felt	1.0
Emissivity of low temperature enclosure	1.0
Heating power	70 kW/kg
External temperature of the Cz-furnace	500.0 K
Heat transfer coefficient	40.0 W/m^2K
Temperature of low temperature enclosure	900.0 K
Melting temperature	1685.0 K
Latent heat	1800.0 kJ/kg
Stefan-Boltzmann constant	$5.67 \cdot 10^{-8}$ W/m^2K^4
Viscosity of melt	0.00075 kg/ms
Surface tension coefficient	0.72 N/m
Temperature coefficient of surface tension	0.00013881/K
Heat expansion coefficient	0.00014 1/K
Reference temperature	1685.0 K
Gravity	9.82 m/s^2

Table 6.1 Material parameters in Czochralski silicon crystal growth

Component	Material	Height	Radius/Thickn.
Crystal	Silicon	20.0 cm	6.35 cm
Melt	Silicon	12.0 cm	20.0 cm
Crucible bottom	Silica	1.0 cm	21.0 cm
Crucible side	Silica	27.5 cm	1.0 cm
Susceptor bottom	Graphite	6.6 cm	23.0 cm
Susceptor side	Graphite	30.4 cm	2.0 cm
Heater	Graphite	54.8 cm	1.5 cm
Crucible shaft	Graphite	23.5 cm	3.6 cm
Thermal shields bottom	Graphite, felt	9.0 cm	27.5 cm
Thermal shields side	Graphite, felt	79.9 cm	2.0 cm

Table 6.2 Czochralski construction

The finite element mesh which is used throughout in this chapter is depicted in Figure 6.1. The mesh consists of 3632 quadrilateral elements and 3849 nodes. The number of surface elements required in the view factor computation is 315.

The temperature and velocity fields and the position of the crystal-melt interface are the quantities which we are most interested in. We visualize the numerical results of the computations in the following manner: The temperature distribution in the whole geometry is presented with 50 temperature contours between the minimum and maximum temperature values. In the melt region the temperature and velocity fields and the position of the crystal-melt interface are additionally shown. The temperature field consists of 10 contours between the melting point temperature T_f and $T_f + 30$. We show in addition the pressure fields in some cases.

Initially we assume that the temperature distribution in the crystal varies linearly in the z-direction from the melting temperature 1685 K at the crystal-melt interface to the temperature of the low temperature enclosure 900 K on the crystal top. In the melt and in the surroundig parts the initial temperature is set to 1715 K. The melt is initially at the motionless state.

We begin the computations with the simulation of heat transfer in the whole geometry and the melt flow induced by the Grashof convection. As in the previous chapters we compute an initial guess for the flow field by using the reduced Reynolds numbers. We proceed so that in the beginning of the simulation the Reynolds number is three orders of magnitude lower than the true one, then two orders of magnitude lower and so forth. The initial guess at $t = 30$ s for temperature and velocity fields are shown in Figures 6.2 (left) and 6.3a-b with the reduced Reynolds number which is one order of magnitude lower than the real one. By using the initial guess the simulation of the Grashof convection with the true Reynolds number is carried out for 25 seconds with a time step of 0.1 seconds. The numerical results are shown in Figure 6.2 (right) and Figures 6.4a and6.4b.

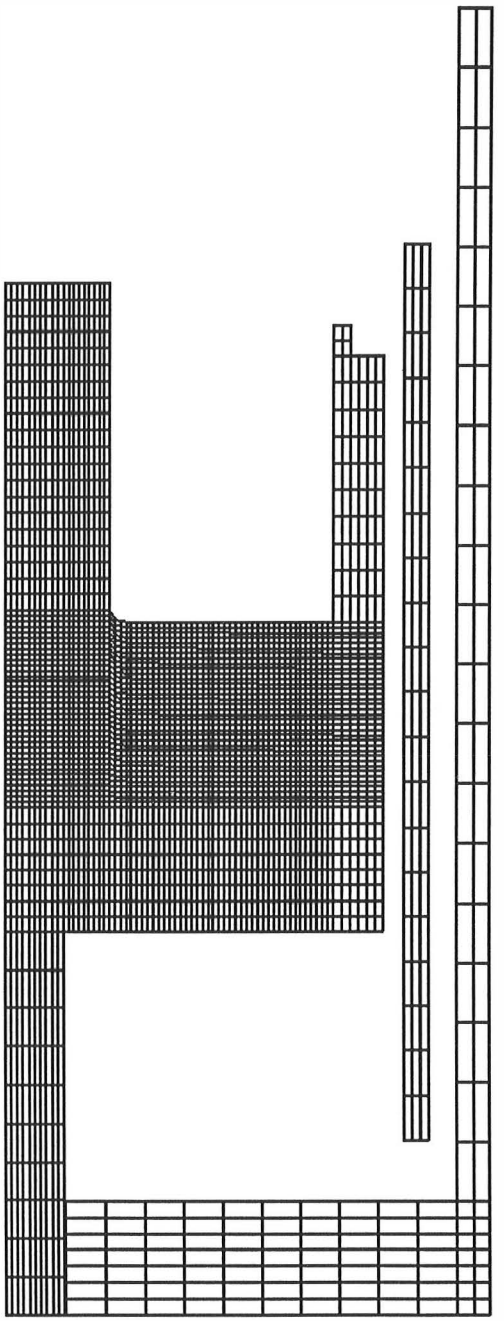

Figure 6.1 Finite element mesh in Czochralski crystal growth

The time frame (55 seconds) is naturally quite short from the crystal growth point of view. However, the effect of radiation in heat transfer can be seen in Figure 6.2. The heater, the silica crucible and the graphite susceptor see the low temperature enclosure and therefore the temperature variations increase in these regions. On the other hand the heater has a warming influence on the graphite susceptor, the crucible pedestal and the thermal shields. Since the finite element mesh is quite coarse in the lower part of the thermal shields, some oscillations appear in the temperature distribution. The oscillations, however, disappear when the finite element mesh is denser.

Typically 2-4 Navier-Stokes iterations were required in order to achieve the termination criterion. The SOR iteration converged to a solution typically by one iteration step. The computations were carried out at the Center for Scientific Computing on Convex C3840 and some computation time statistics are listed in Table 6.3.

Operation	Computation time
View factor calculation	107.40 CPUs
Assembling of matrices in the Navier-Stokes equations	4.32 CPUs
Assembling of of matrices in the enthalpy equation	1.01 CPUs
One SOR iteration	0.57 CPUs
One Navier-Stokes iteration	39.09 CPUs

Table 6.3 Computational time statistics in Czochralski crystal growth

Although we have so far simulated numerically the melt flow driven by the Grashof convection the discretized Navier-Stokes equations contain all three velocity components (later on we simulate rotations of the crystal and crucible). In the crystal and melt the number of finite element nodes is 2812 and thus we have 8436 degrees of freedom in the discretized Navier-Stokes equations. Correspondingly, the number of degrees of freedom in SOR iteration is 3849 (the number of nodes) which partly explains the difference in the computational times. In the computation of the velocity and enthalpy fields a band structure of the matrices is used. The CPU time used in the view factor computation is relatively low with regard to the number of surfaces which was 315.

In order to achieve convergence in the Navier-Stokes iteration a relatively short time step was required. In this simulation we used 0.1 s time step. With a time step of 0.2-0.5 seconds the Navier-Stokes iteration oscillated. Although the semi-implicit time discretization in the computation of the enthalpy was used, a convergent solution for the enthalpy with these time steps was found. We conclude that the solving of the flow field prevents the use of the larger time steps.

In the following we assume that the melt flow is driven by the Marangoni convection only. The initial guess for the temperature distribution and melt flow is

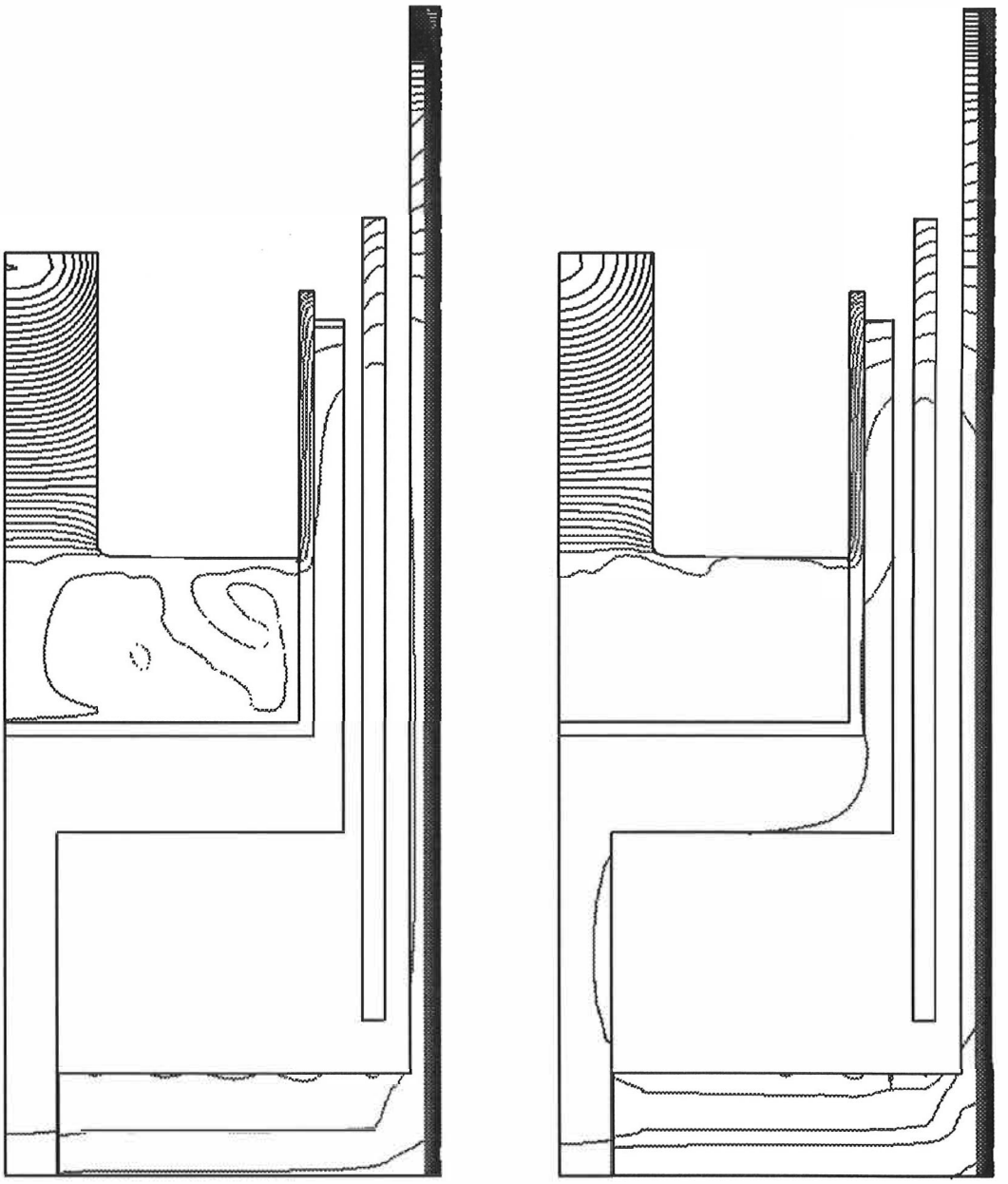

Figure 6.2 Temperature fields at $t = 30$ s (left, initial guess), $t = 55$ s (right), Grashof convection

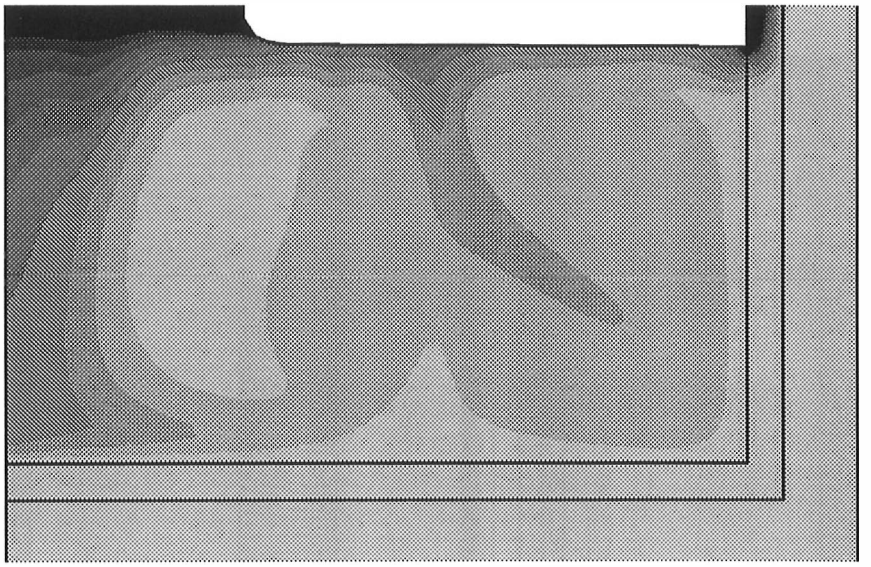

Figure 6.3a Temperature field in melt induced by Grashof convection at $t = 30$ s, reduced Reynolds number

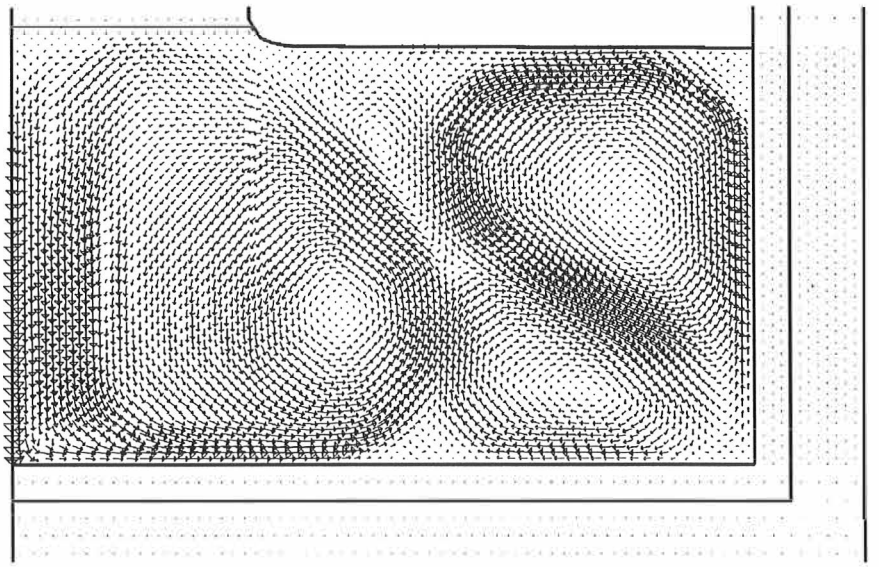

Figure 6.3b Velocity field in melt induced by Grashof convection at $t = 30$ s, reduced Reynolds number

Figure 6.4a Temperature field in melt induced by Grashof convection at $t = 55$ s

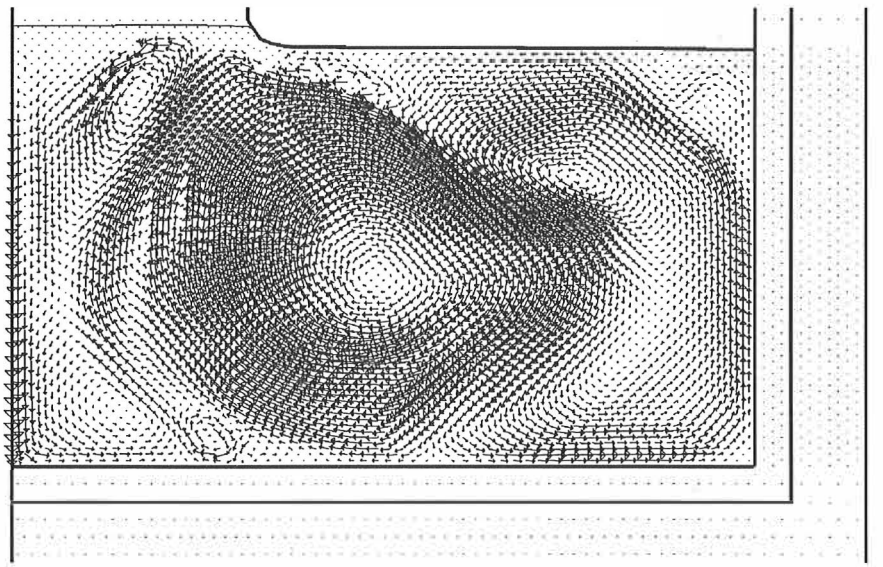

Figure 6.4b Velocity field in melt induced by Grashof convection at $t = 55$ s

the same as before: The temperature distribution in the crystal is linear in the z-direction between the melting temperature 1685 K at the crystal-melt interface and the temperature of the low temperature enclosure 900 K on the crystal top. In the melt and in the surroundig parts the initial temperature is set to 1715 K. The velocity field in the melt is initially zero.

We begin the simulation with the reduced Reynolds number (μ =0.075 kg/ms). The temperature distribution in the entire geometry and the melt flow field after 10 seconds are presented in Figure 6.5 (left) and Figures 6.6a-b. These numerical results represent an initial guess for the numerical simulation of the Marangoni convection with the true Reynolds number. The simulation is carried out in the time frame 10-130 s.

In Figure 6.5 (right) and Figures 6.7a-6.10b the temperature and velocity fields with an interval of 40 seconds are depicted. At the beginning of the simulation there is a cold spot between the crystal and silica crucible at the melt-gas interface. This causes two surface flows moving to the opposite directions towards each others (Figures 6.6a-b). The collision of the flows creates a flow front moving towards the melt bottom. This flow carries cold material from the melt-gas interface with it (Figures 6.7a-b). The maximum velocity $|u|$ is around 2 cm/s while the same value in the simulation of the Grashof convection was around 8 cm/s. This observation strengthens our impression of the dominating role of the Grashof convection in both heat and mass transfer mechanisms respect to the Marangoni convection.

The numerical results presented in Figures 6.8 (right) and 6.10a-b (global temperature distribution and melt flow induced by Marangoni convection) operate as an initial guess when simulating the system where the melt flow is governed by the Grashof and Marangoni convection and the rotations of the crucible and crystal. Figures 6.11-6.13c present the situation where the rotation rate of the crucible is 5 rpm (crystal rotation neglected) and Figures 6.14-6.16c the situation where the rotation rate of the crystal is -5 rpm (crucible rotation neglected). The time frame in both simulations is 130-140 seconds.

The colder spot which previously caused two surface flows at the melt-gas interface has now enlarged and forms a thin solid region at this interface, Figure 6.13b. This indicates that the surrounding parts viewed by the melt-gas interface do not have a correct thermal distribution in the sense that normally the melt does not contain solid parts.

At the beginning of the simulations the melt flow behaves relatively well. However, when the simulations have proceeded for a while, oscillations in the velocity fields begin to occur. In the case of the crucible rotation the pressure field in Figure 6.13c is still tolerable. When rotating the crystal the pressure field corrupts after 10 seconds simulation, Figure 6.16c, and a clear checkerboard pattern for pressure can be seen. We continued the simulations after 10 seconds for both rotations. We had great difficulties in maintaining convergence in the Navier-Stokes iterations and finally convergence was lost.

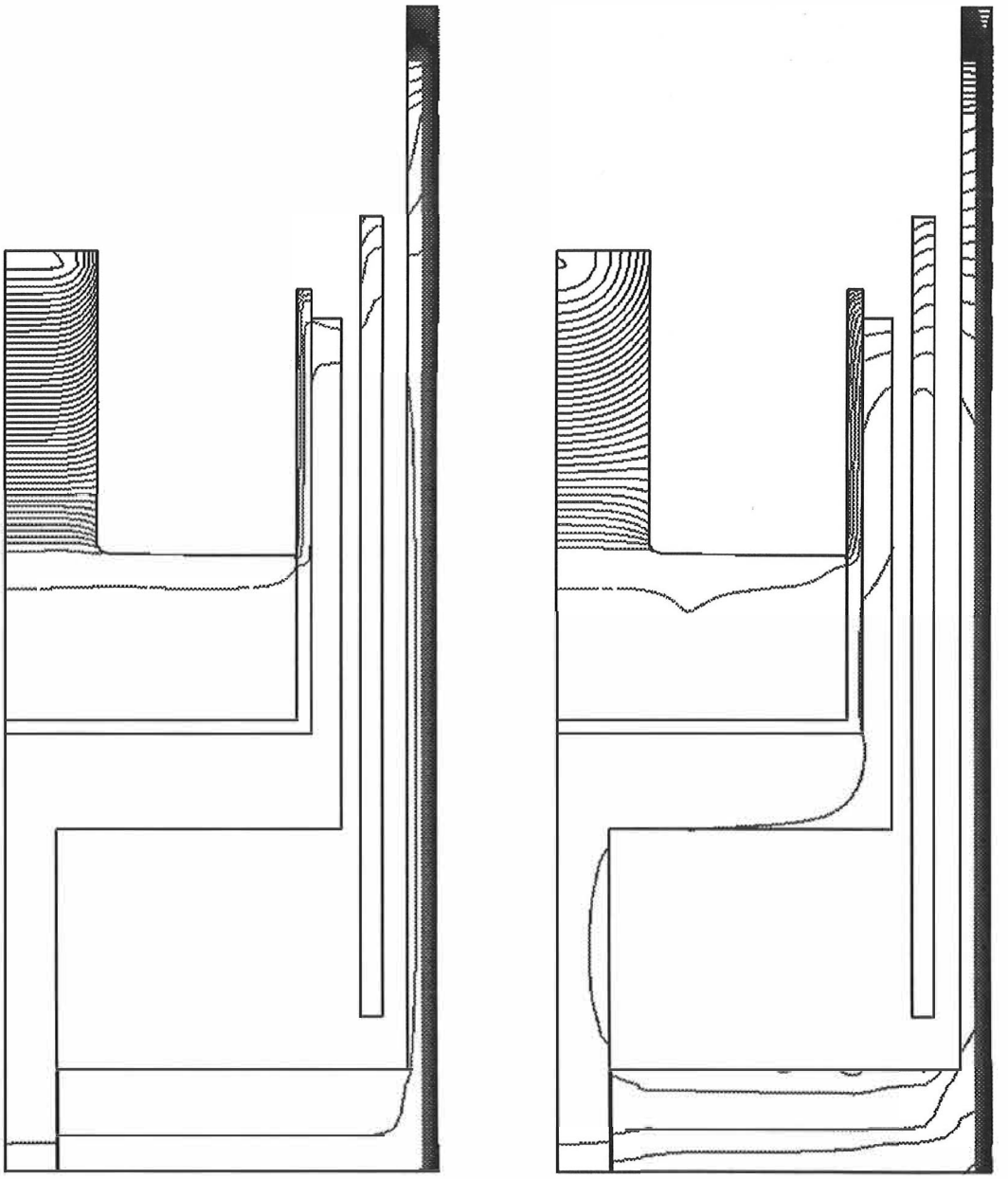

Figure 6.5 Temperature fields at $t = 10$ s (left, initial guess), $t = 50$ s (right), Marangoni convection

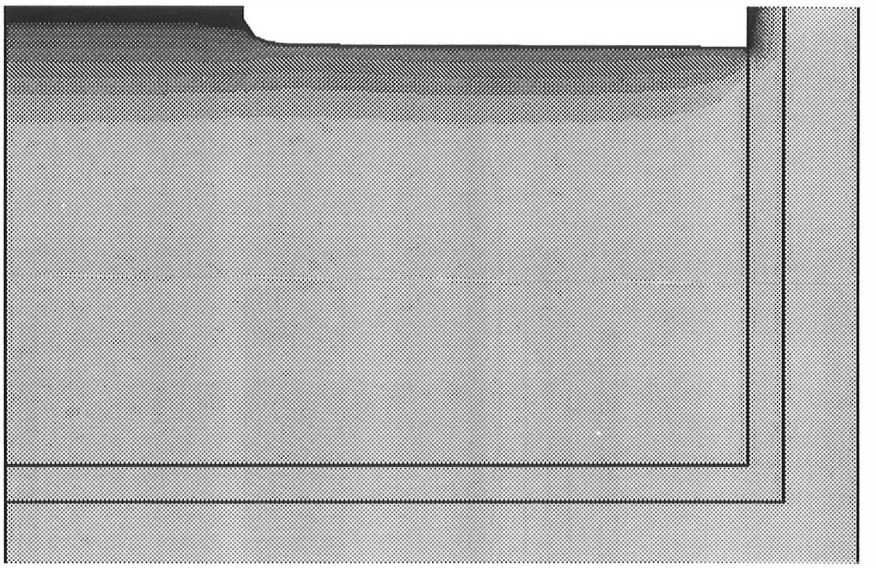

Figure 6.6a Temperature field in melt induced by Marangoni convection at $t = 10$ s, reduced Reynolds number

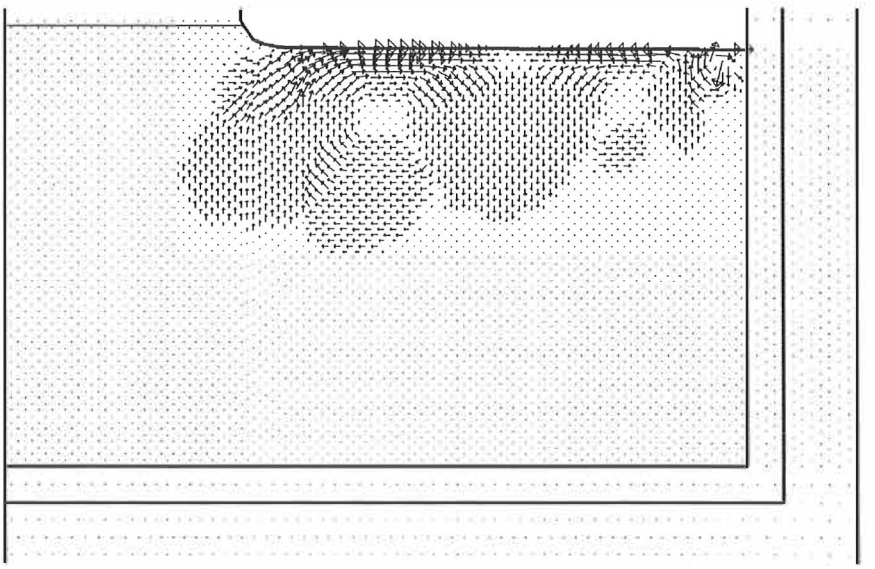

Figure 6.6b Velocity field in melt induced by Marangoni convection at $t = 10$ s, reduced Reynolds number

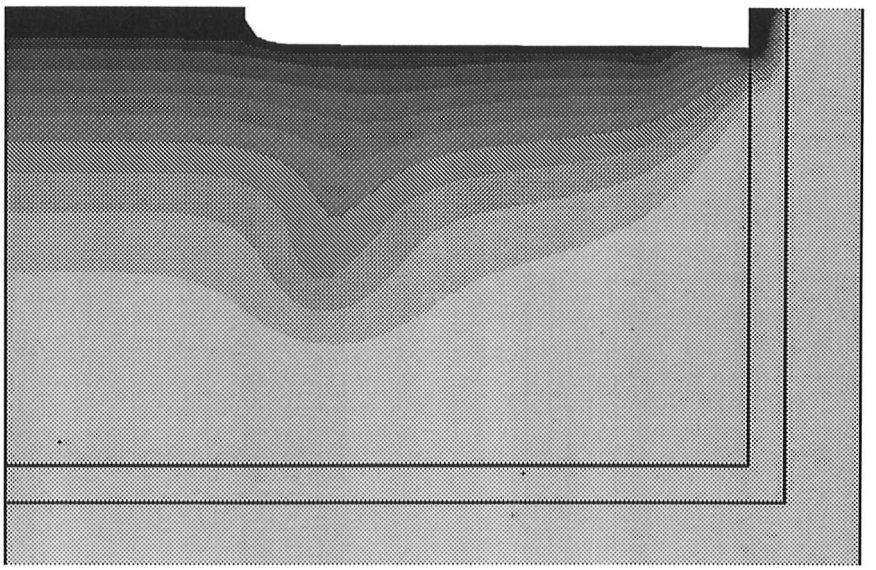

Figure 6.7a Temperature field in melt induced by Marangoni convection at $t = 50$ s

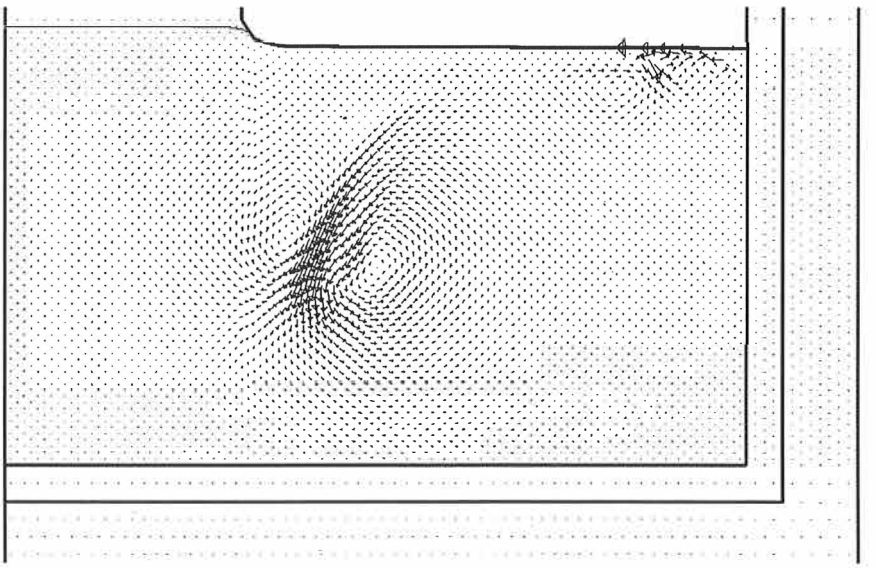

Figure 6.7b Velocity field in melt induced by Marangoni convection at $t = 50$ s

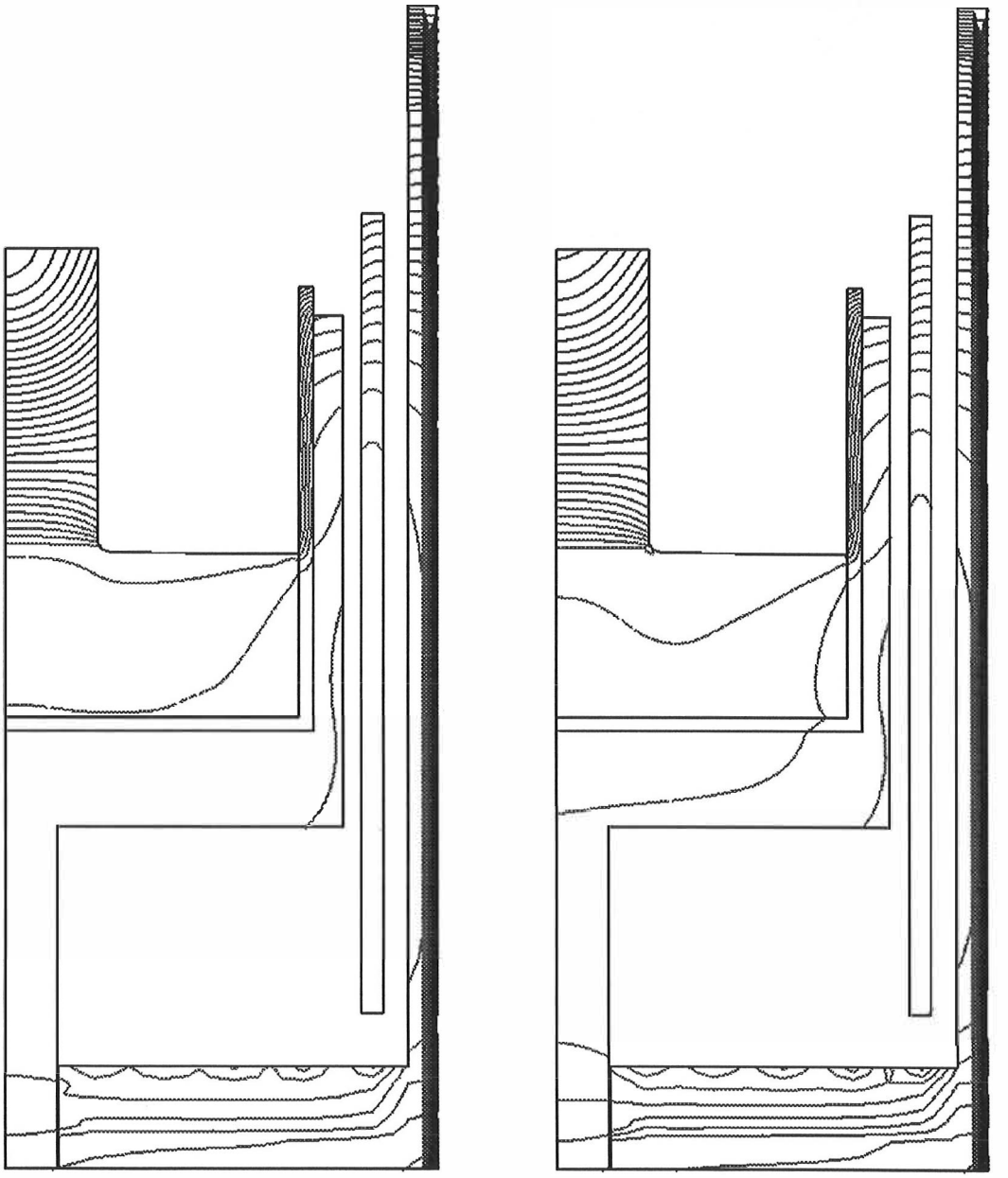

Figure 6.8 Temperature fields at $t = 90$ s (left), $t = 130$ s (right), Marangoni convection

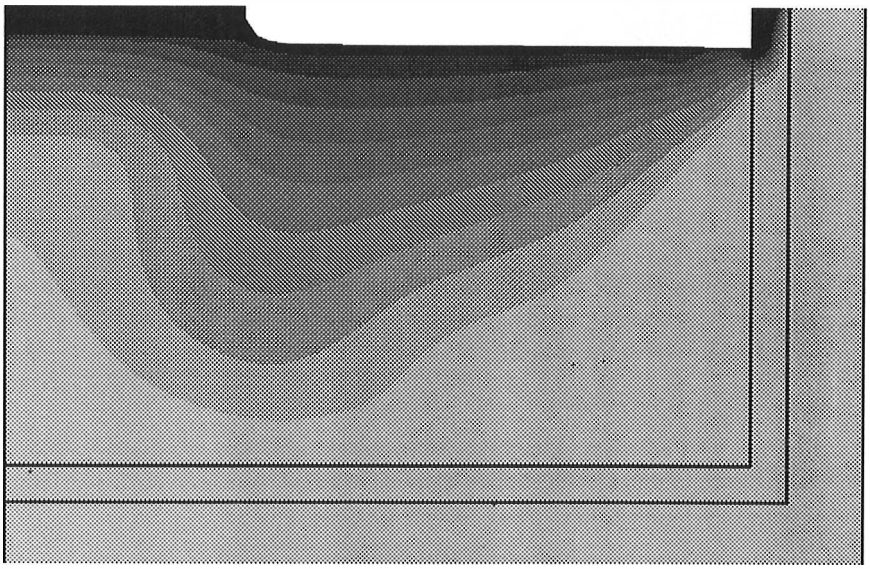

Figure 6.9a Temperature field in melt induced by Marangoni convection at $t = 90$ *s,*

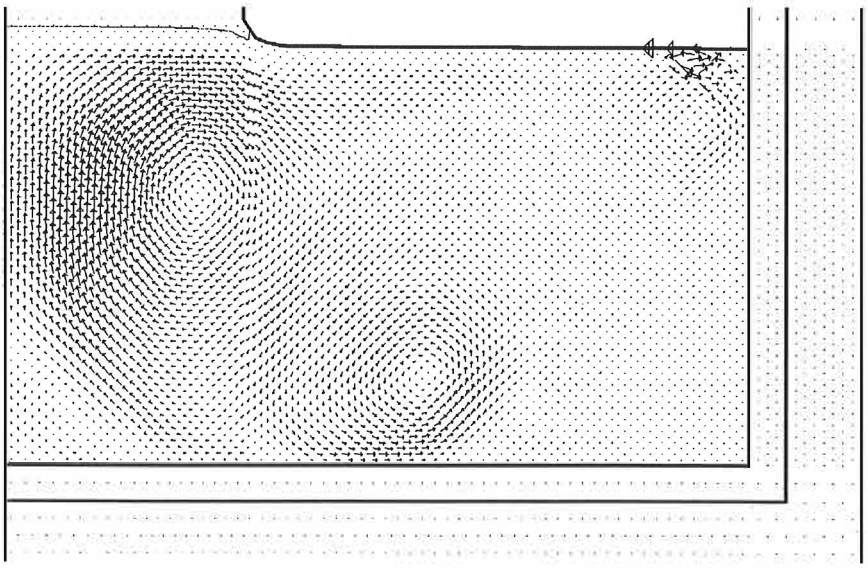

Figure 6.9b Velocity field in melt induced by Marangoni convection at $t = 90$ *s,*

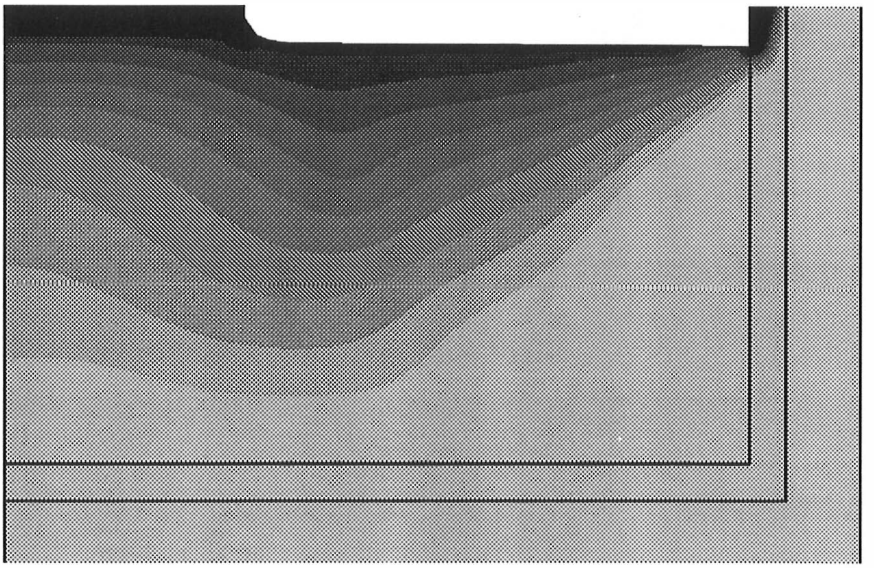

Figure 6.10a Temperature field in melt induced by Marangoni convection at $t = 130$ *s*

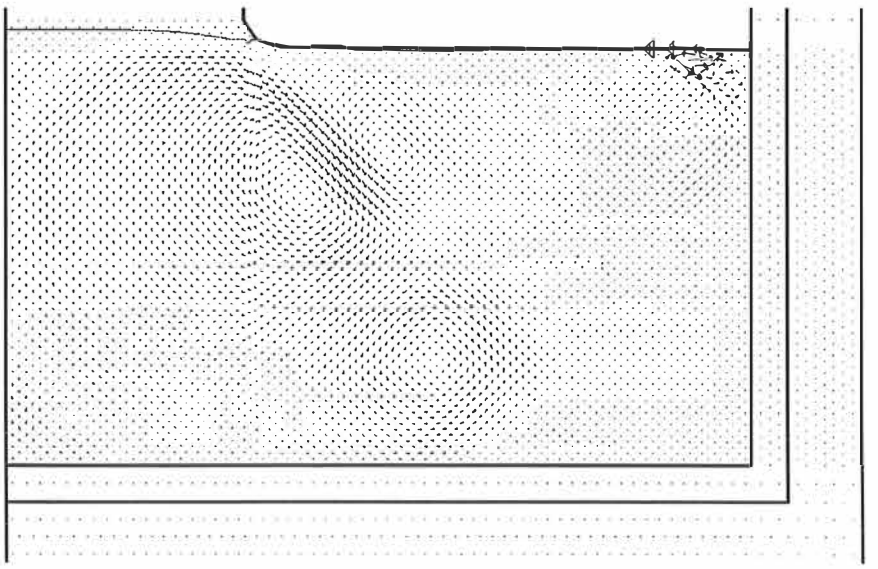

Figure 6.10b Velocity field in melt induced by Marangoni convection at $t = 130$ *s*

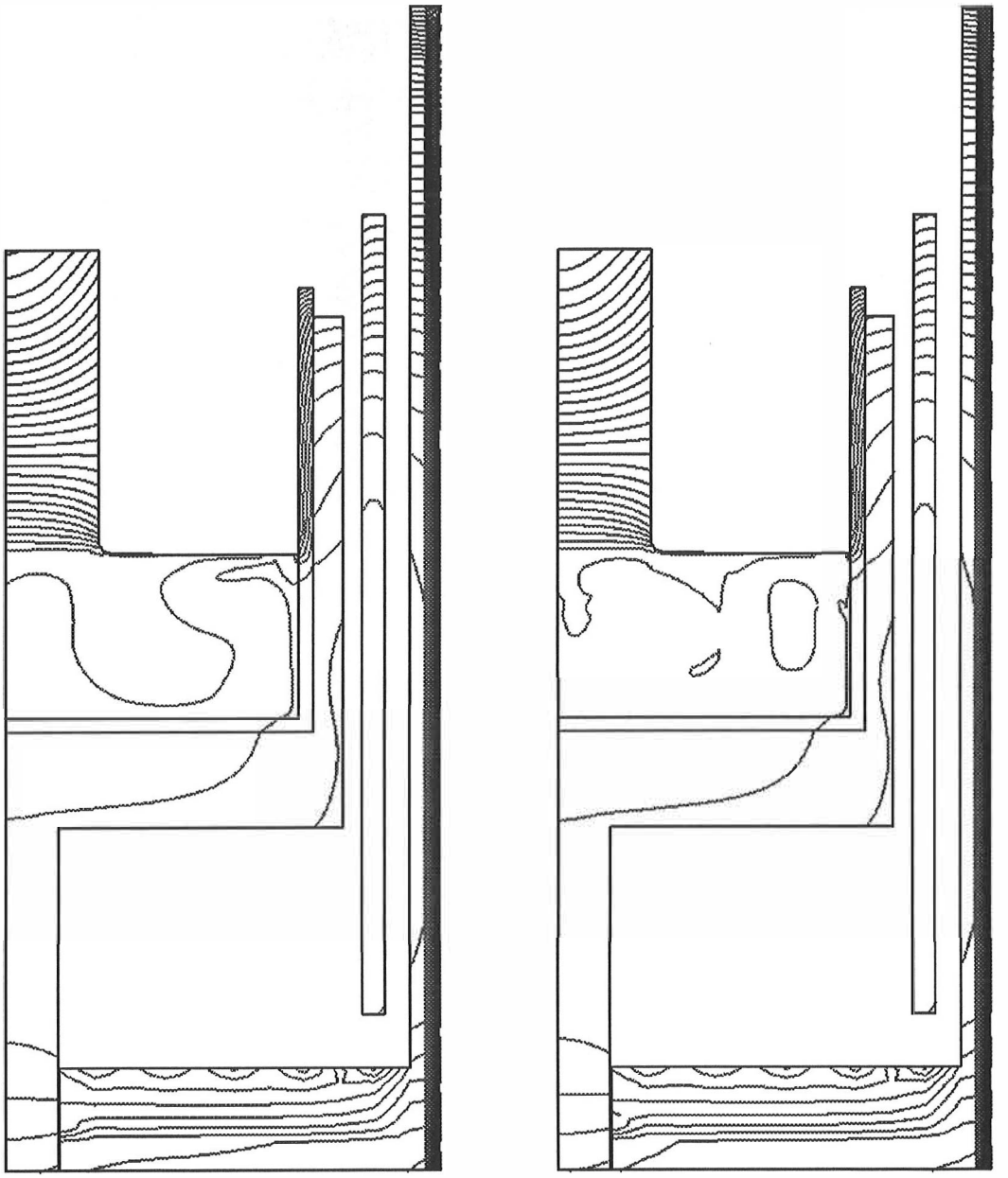

Figure 6.11 Temperature fields at $t = 135$ s (left), $t = 140$ s (right), Grashof and Marangoni convections, rotation of crucible (5 rpm)

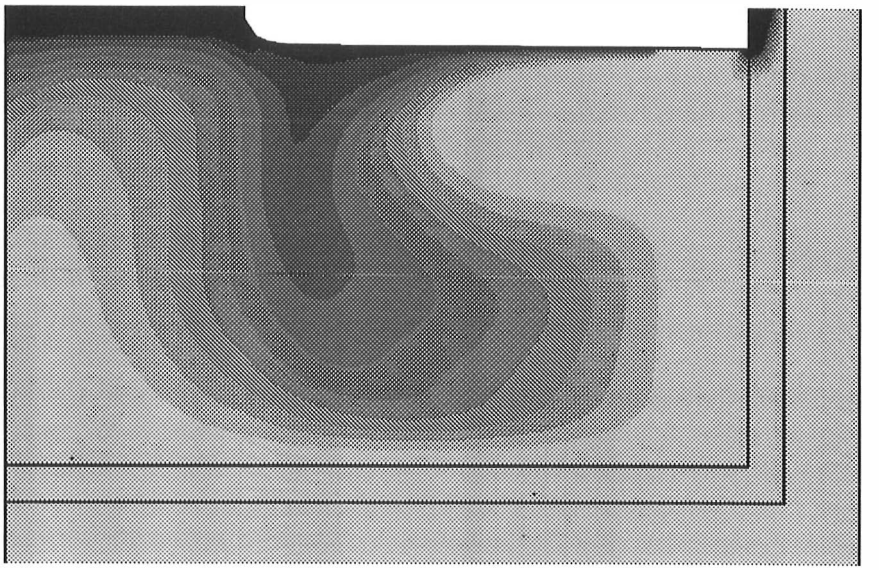

Figure 6.12a Temperature field in melt induced by Grashof and Marangoni convection and rotation of crucible (5 rpm) at $t = 135$ s

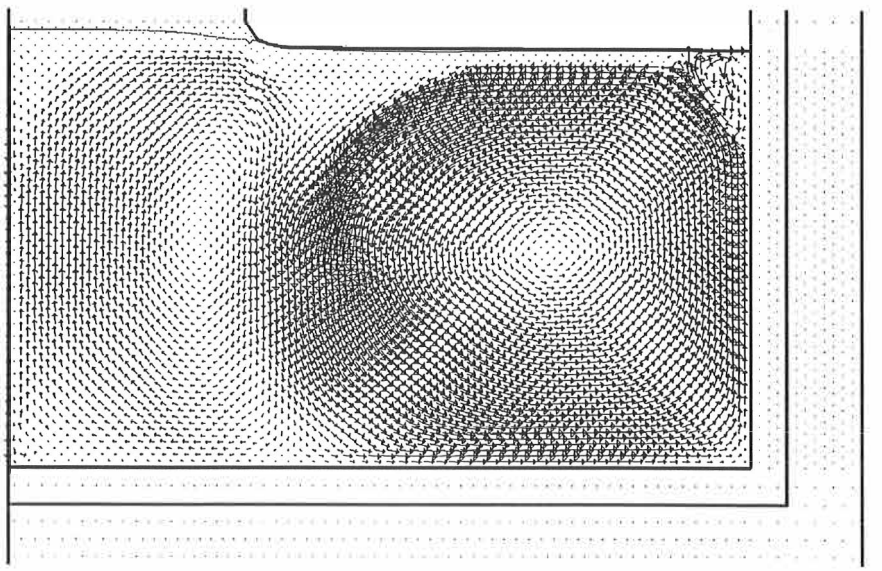

Figure 6.12b Velocity field in melt induced by Grashof and Marangoni convection and rotation of crucible (5 rpm) at $t = 135$ s

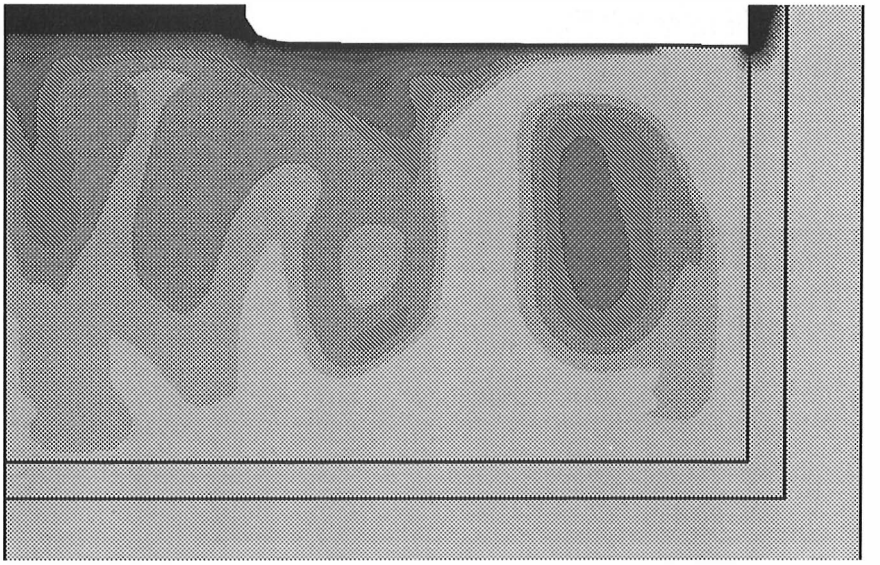

Figure 6.13a Temperature field in melt induced by Grashof and Marangoni convection and rotation of crucible (5 rpm) at $t = 140$ s

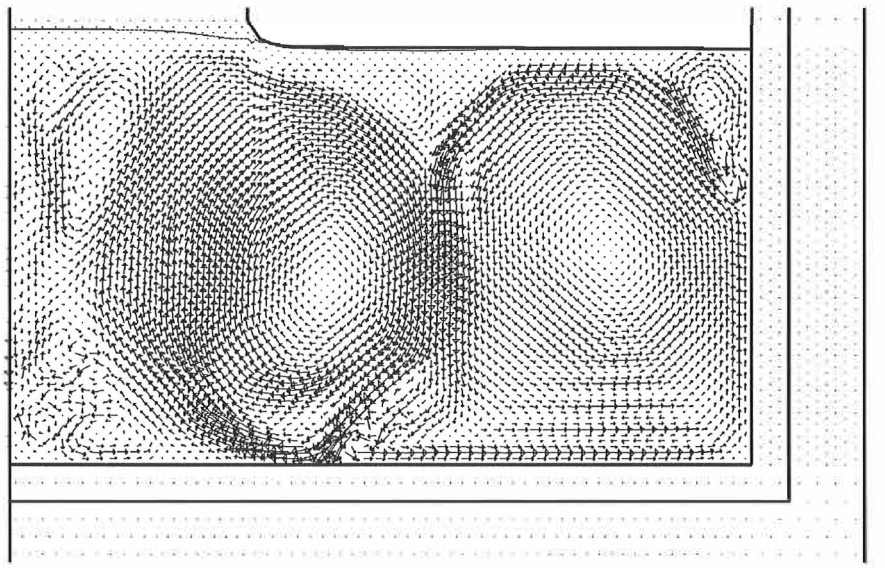

Figure 6.13b Velocity field in melt induced by Grashof and Marangoni convection and rotation of crucible (5 rpm) at $t = 140$ s

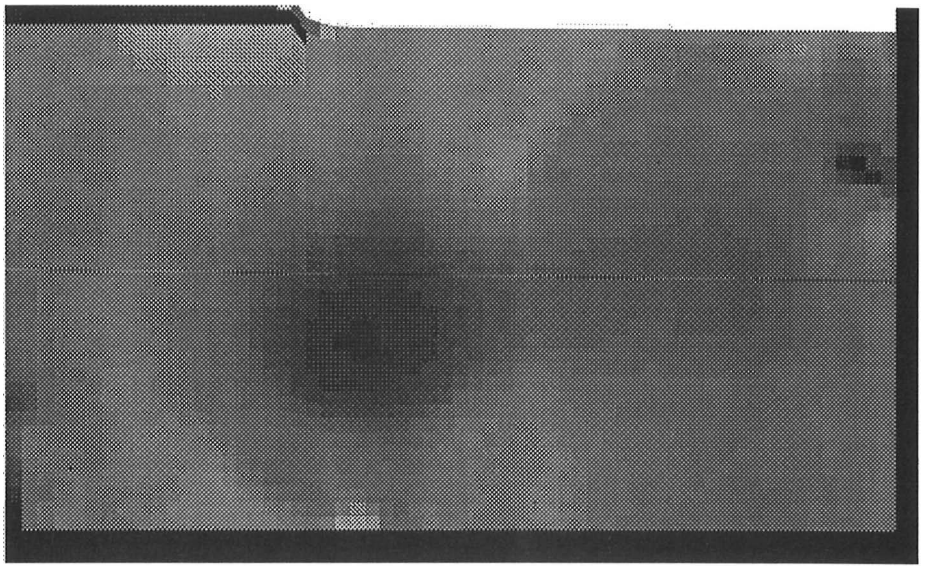

Figure 6.13c Pressure field in melt induced by Grashof and Marangoni convection and rotation of crucible (5 rpm) at $t = 140$ *s*

The reason for loss of convergence is not well understood. In general a proper velocity field can in principle be achieved even if the pressure field contains a checkerboard pattern. However, is is quite obvious, that in a long run a corrupted pressure field may lead to problems in velocity fields and loss of convergence of the Navier-Stokes iteration. On the other hand, the procedure of the numerical simulation of the melt flow, at least from our own experience point of view, is very sensitive. The finite element mesh generated to the melt region was coarser in this chapter than for instance in the previous chapter. The Navier-Stokes solvers in both chapters were in practice the same. Temperature environments to the melt were not so dramatically different, so too coarse mesh might have generated instabilities in velocity fields. We could have also applied a more considerate approach in taking into account the convection mechanisms. Now we started a full simulation with a solution of Marangoni convection as an initial guess. We could have started with the Grashof convection, first by adding the Marangoni convection to the system and then gradually the rotations as we did in the previous chapter. Increasing the Reynolds number by one order of magnitude at a time in the simulations of the Grashof convection was also perhaps too violent.

We have carried out some numerical simulations with material parameters deviating from the corresponding parameters of silicon. Then from the numerical simulation point of view the problem can be much simpler and convergent solutions without oscillations can be obtained. A denser finite element mesh could

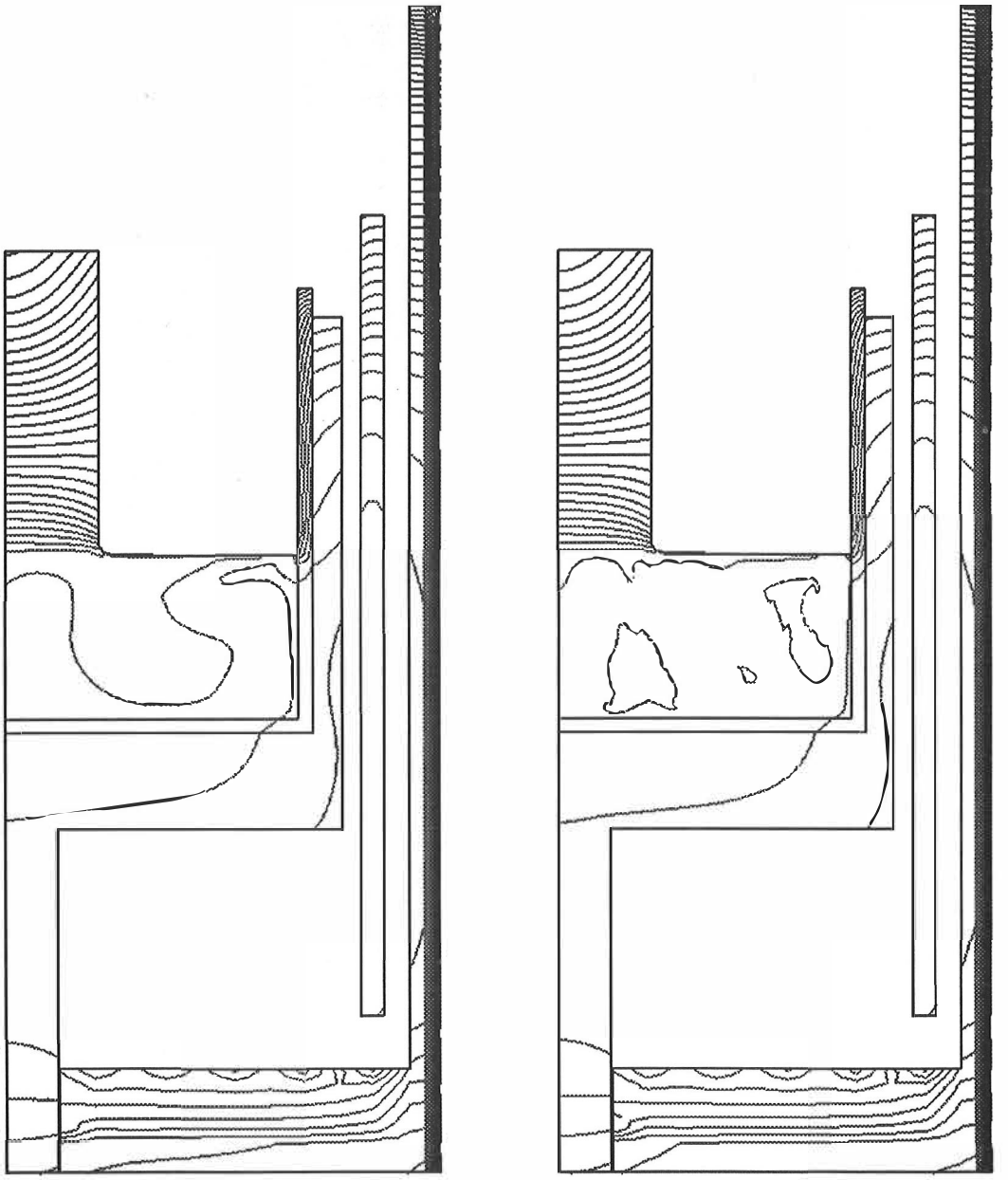

Figure 6.14 Temperature fields at $t = 135$ s (left), $t = 140$ s (right), Grashof and Marangoni convections, rotation of crystal (-5 rpm)

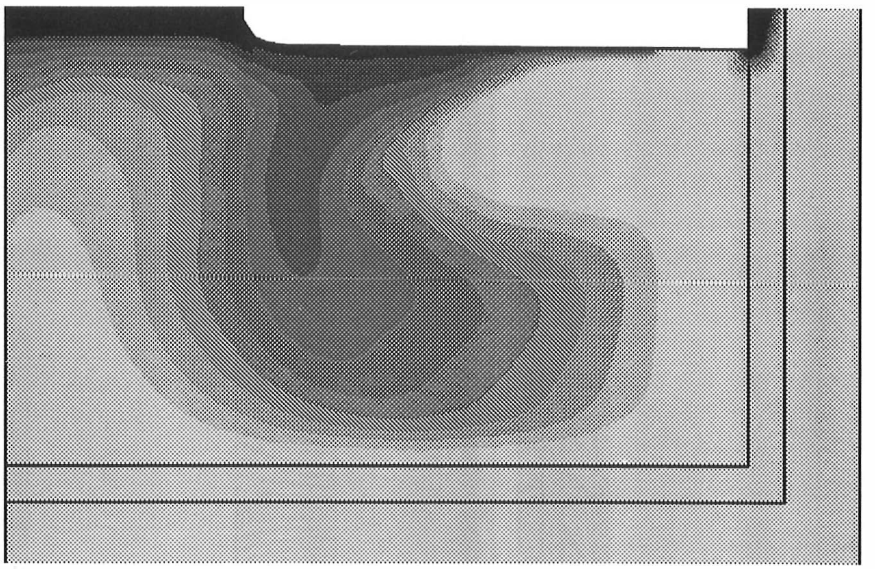

Figure 6.15a Temperature field in melt induced by Grashof and Marangoni convection and rotation of crystal (-5 rpm) at $t = 135$ s

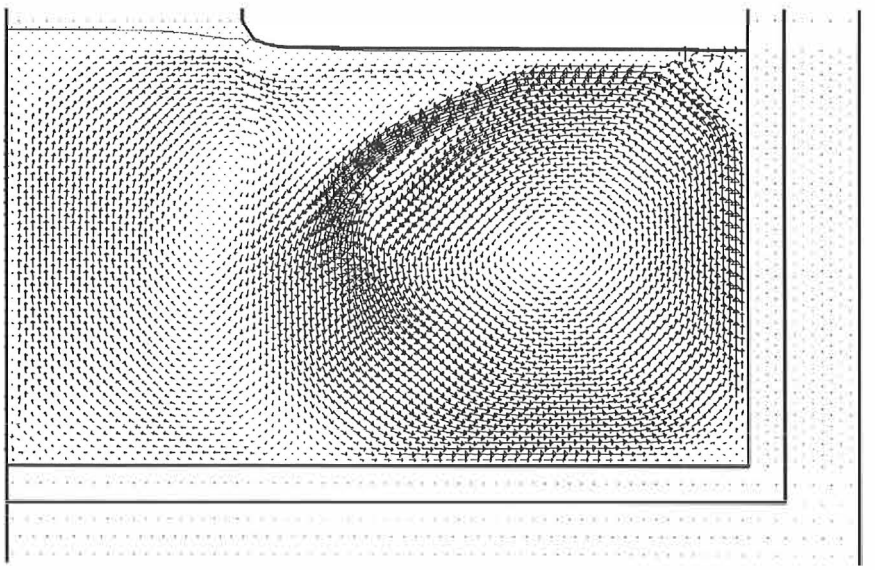

Figure 6.15b Velocity field in melt induced by Grashof and Marangoni convection and rotation of crystal (-5 rpm) at $t = 135$ s

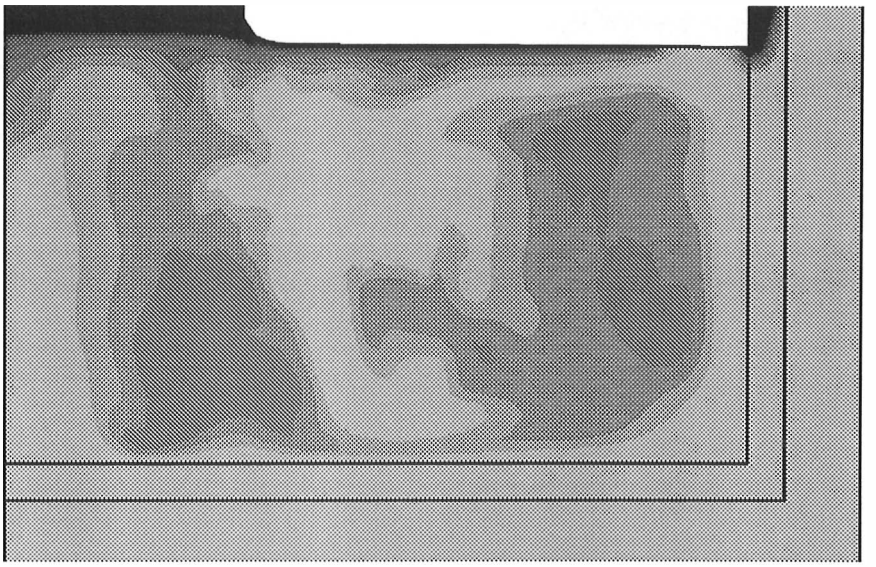

Figure 6.16a Temperature field in melt induced by Grashof and Marangoni convection and rotation of crystal (-5 rpm) at $t = 140$ s

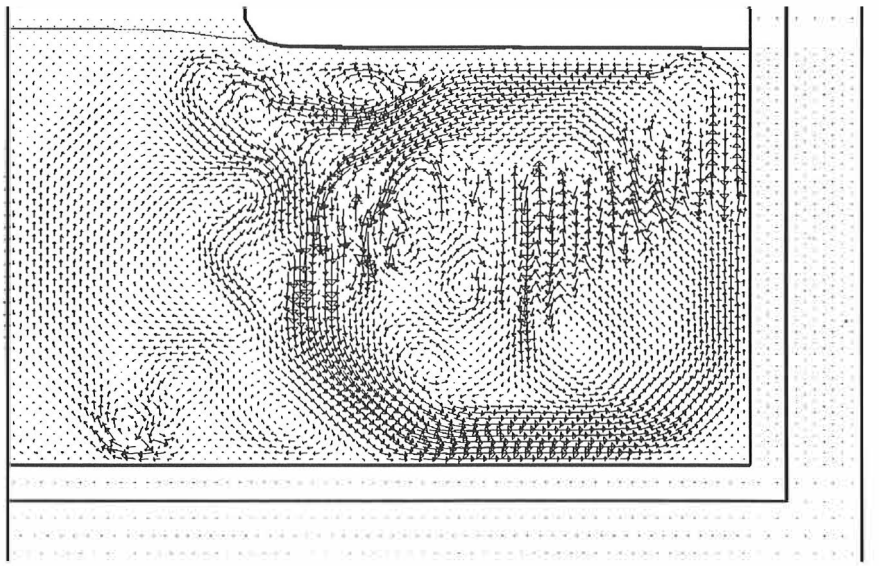

Figure 6.16b Velocity field in melt induced by Grashof and Marangoni convection and rotation of crystal (-5 rpm) at $t = 140$ s

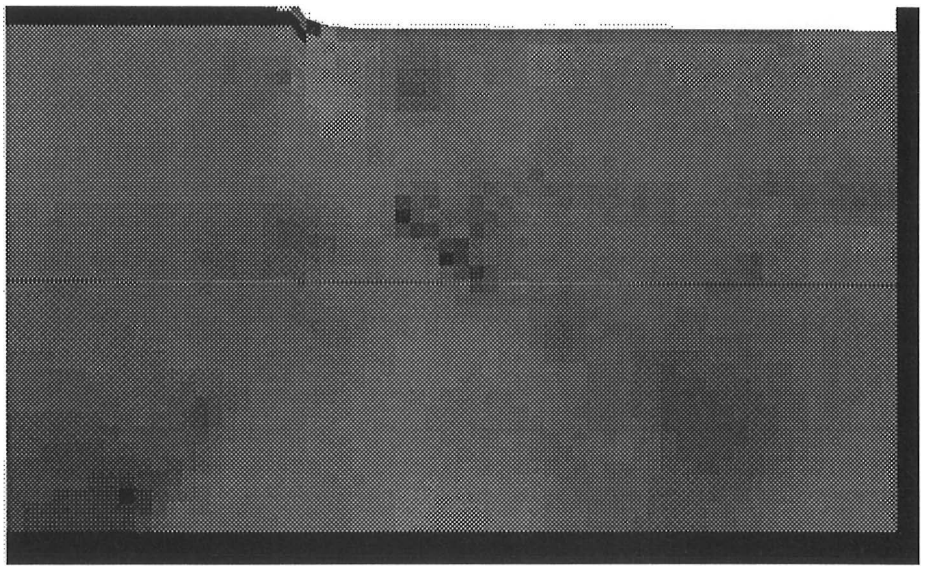

Figure 6.16c Pressure field in melt induced by Grashof and Marangoni convection and rotation of crystal (-5 rpm) at $t = 140$ *s*

improve the situation, but a thorough investigation in this subject is still lacking. In addition, a use of more robust finite element tools is desirable.

7. Conclusions

In this work we considered mathematical modeling and numerical simulation of the Czochralski crystal growth. Due to the complexity of the process we divided it into subproblems from the mathematical modeling and numerical simulation point of view. We studied separately the pure melt flow and the phase change problem between the crystal and melt. Taking advantage of the knowledge from these subproblems we constructed a mathematical model and numerical simulation tools for the entire Czochralski process so that radiation in heat transfer was also taken into account. The numerical simulation tools were based on the SUPG finite element method.

A study of the melt flow played an important role in this work. We illustrated the transient character of the melt flow with numerical examples. In the rotationally symmetric geometry we studied the melt flow caused by the Grashof and Marangoni convections and the rotation of the crucible. Later on, related to the phase change problem, the effect of the crystal rotation was taken into account.

In the pure melt flow and in the phase change problem convergent solutions of the melt flow were found. However, in the case of the entire Czochralski crystal growth we were able to simulate the melt flow only for some seconds for the rotations of the crystal or the crucible together with the Grashof and Marangoni convections, since convergence in the Navier-Stokes iteration was lost. The reason for loss of convergence might be a corrupted pressure pattern (checkerboard pattern), a poor initial guess for velocity field or too coarse finite element mesh. The simulations were carried out in the large-scale Czochralski geometry with the material parameters of silicon.

Compared to articles found in the literature we applied a new method for the phase change problem in the Czochralski crystal growth context. We introduced the enthalpy, the definition of which contained the phase front conditions. The use of the enthalpy method allows one to operate in fixed finite element meshes which are generated only once, at the beginning of simulations. Since our meshes remain unchanged we have to compute the view factors required in the radiation modeling only once.

In the crystal-melt system we had to compute the Navier-Stokes equations in the varying geometry due to the presence of the phase change interface. We applied the variable viscosity method in the crystal-melt system so that the viscosity in the crystal was set to a large value.

In the crystal-melt system we applied the standard definition of enthalpy which offered a way to treat the free boundary problem between the crystal and melt. This definition, however, was not suitable for the entire Czochralski crystal growth geometry due to the enthalpy discontinuity at the interfaces between two different

materials. Therefore we modified the definition of enthalpy such that we guaranteed the continuity at these interfaces.

The formulation of the diffuse-gray radiation differed from previously published crystal growth articles and standard textbooks on which radiative heat transfer is considered. We introduced a non-local boundary condition on the radiating part of the surface in the Czochralski system instead of treating a radiative surface as a finite union of simple surface elements.

The main objective in this work was to build a mathematical model in the entire Czochralski crystal growth geometry describing the melt flow and heat transfer by radiation, conduction and convection and solve the model numerically. The numerical simulations were carried out in large scale crystal growth environment and we proved that we have capable numerical simulation tools up to a certain limit.

A bottle neck in this research was the simulation of the silicon melt flow. In the finite element analysis we applied the penalty method together with bilinear velocity-constant pressure approach in order to solve the Navier-Stokes equations. With this approach we did not succeed to find a convergent solution with the real Reynolds number. We shall endeavor towards this aim and our future work will include a study of more sophisticated tools of finite elements.

We have also to deliberate how important it is to hunt the true Reynolds number. Would it be sufficient to restrict to reduced Reynolds numbers and qualitative temperature and velocity fields? How well would qualitative temperature and velocity fields correspond the real situation? To answer these questions, and to verify the reliability of the developed numerical simulation tools, comparisons between numerical results and experiments are undoubtedly required.

8. References

" [Anselmo93]" A. Anselmo, V. Prasad, J. Koziol and K.P. Gupta, *Numerical and Experimental Study of a Solid Pellet Feed Continuous Czochralski Growth Process for Silicon Single Crystals*, Journal of Crystal Growth 131 (1993), pp. 247-264.

" [Argyris92]" J. Argyris, A. Laxander, J. Szimmat, *Petrov-Galerkin Finite Element Approach to Coupled Heat and Fluid Flow*, Computer Methods in Applied Mechanics and Engineering 94 (1992), pp. 181-200.

" [Atherton87]" L.J. Atherton, J.J. Derby, R.A. Brown, *Radiative Heat Exchange in Czochralski Crystal Growth*, Journal of Crystal Growth 84 (1987), pp. 57-78.

" [Brooks82]" A.N. Brooks, T.J.R. Hughes, *Streamline Upwind/Petrov-Galerkin Formulations for Convection Dominated Flows with Particular Emphasis on the Incompressible Navier-Stokes Equations*, Computer Methods in Applied Mechanics and Engineering 32 (1982) pp. 199-259.

" [Cecchi95]" M.M. Cecchi, K. Morgan, J. Periaux, B.A. Schrefler, O.C. Zienkiewicz (eds.), *Proceedings of the Ninth International Conference on Finite Elements in Fluids, New Trends and Applications (Parts I-II)*, Venezia, Italy, 1995.

" [Cuvelier86]" C. Cuvelier, J.M. Driessen, *Thermocapillary Free Boundaries in Crystal Growth*, J. Fluid Mech. (1986), vol. 169, pp. 1-26.

" [Cuvelier86b]" C. Cuvelier, A. Segal, A.A. van Steenhoven, *Finite Element Methods and Navier-Stokes Equations*, D. Reidel Publishing Company, 1986.

" [Cuvelier87]" C. Cuvelier, *Some Numerical Methods for the Computation of Capillary Free Boundaries Governed by the Navier-Stokes Equations*, Reports of the Faculty of Technical Mathematics and Informatics, No. 87-69 (1987), Delft University of Technology.

" [Dalhuijsen86]" A.J. Dalhuijsen, A. Segal, *Comparison of Finite Element Techniques for Solidification Problems*, International Journal for Numerical Methods in Engineering, Vol. 23, pp. 1807-1829 (1986).

" [Derby87]" J.J. Derby, L.J. Atherton, P.D. Thomas, R.A. Brown, *Finite-Element Methods for Analysis of the Dynamics and Control of Czochralski Crystal Growth*, Journal of Scientific Computing, Vol. 2, No. 4, 1987.

" [Elliot82]" C.M. Elliot, J.R. Ockendon, *Weak and Variational Methods for Moving Boundary Problems*, Research Notes in Mathematics, Res. Notes Math., Pitman, 1982.

" [Franca92a]" L.P. Franca, S.L. Frey, T.J.R. Hughes, *Stabilized Finite Element Methods: I. Application to the Advective-Diffusive Model*, Computer Methods in Applied Mechanics and Engineering 95 (1992), pp. 253-276.

" [Franca92b]" L.P. Franca, S.L. Frey, *Stabilized Finite Element Methods: II. The Incompressible Navier-Stokes Equations*, Computer Methods in Applied Mechanics and Engineering 99 (1992), pp. 209-233.

" [Franca93]" L.P. Franca, T.J.R. Hughes, R. Stenberg, *Stabilized Finite Element Methods*, Incompressible Computational Fluid Dynamics, Trends and Advances, Edited by M.D. Gunzburger and R.A. Nicolaides, Cambridge University Press 1993.

" [Girault86]" V. Girault, P.A. Raviart, *Finite Element Methods for Navier-Stokes Equations. Theory and Algorithms*, Springer Series in Computational Mathematics 5, Springer-Verlag, Berlin (1986).

" [Gunzburger93]" M.D. Gunzburger, R.A. Nicolaides (eds.), *Incompressible Computational Fluid Dynamics*, Cambridge University Press 1993.

" [Hilpert91]" M. Hilpert, *Numerical Simulation of Czochralski Crystal Growth*, Report No. 263, Institut Für Mathematik, Universität Augsburg, 1991.

" [Hurle83]" D.T.J. Hurle, *Analytical Representation of the Shape of the Meniscus in Czochralski Growth*, Journal of Crystal Growth 63 (1983), pp. 13-17.

" [Hurle87]" D.T.J. Hurle, G. Müller, R. Nitsche, *Crystal Growth from the Melt*, Fluid Sciences and Material Science in Space, H.U. Walter (editor), pp. 313-354, Springer-Verlag, 1987.

" [Incropera85]" F.P. Incropera, D.P. De Witt, *Fundamentals of Heat and Mass Transfer*, Second Edition, John Wiley and Sons, 1985.

" [Johnson84]" C. Johnson, U. Nävert, J. Pitkäranta, *Finite Element Method for Linear Hyberbolic Problems*, Computer Methods in Applied Mechanics and Engineering 45 (1984), pp. 285-312.

" [Järvinen92]" J.Järvinen, *Mathematical Modelling and Numerical Simulation of Czochralski Crystal Growth*, Phil.Lic. Thesis, Department of Mathematics, University of Jyväskylä, CSC Research Reports R06/92.

" [Kakimoto91]" K. Kakimoto, P. Nicodème, M. Lecomte, F. Dubret, M.J. Crochet, *Numerical Simulation of Molten Silicon Flow; Comparison with Experiment*, Journal of Crystal Growth 114 (1991), pp. 715-725.

" [Katajamäki93]" J. Katajamäki, *Microcomputer Implementation of a Silicon Crystal Growth Simulation Program (in Finnish)*, M.Sc. Thesis, Technical University of Helsinki, Department of Technical Physics, 1993.

" [Kinney93a]" T.A. Kinney, D.E. Bornside, R.A. Brown, *Quantitative Assessment of an Integrated Hydrodynamic Thermal-capillary Model for Large-diameter Czochralski Growth of Silicon: Comparison of Predicted Temperature Field with Experiment*, Journal of Crystal Growth 126 (1993), pp. 413-434.

" [Kinney93b]" T.A. Kinney, R.A. Brown, *Application of Turbulence Modeling to the Integrated Hydrodynamic Thermal-Capillary Model of Czochralski Crystal Growth of Silicon*, Journal of Crystal Growth 132 (1993), pp. 551-574.

" [Křižek90]" M. Křižek, P. Neittaanmäki, *Finite Element Approximation of Variational Problems and Applications*, John Wiley & Sons, New York, 1990.

" [Laitinen89]" E.J. Laitinen, *On the Simulation and Control of the Continuous Casting Problem*, PhD Thesis,Department of Mathematics, University of Jyväskylä, Report 43, 1989.

" [Landau]" L.D. Landau, E.M. Lifschitz, *Lehrbuch der Theoretischen Physik VI*, Akademie Verlag Gmbh, Berlin 1991.

" [Long-An86]" Y. Long-An, *Finite Element Approximation to Axial Symmetric Stokes Flow*, Journal of Computational Mathematics, Vol. 4, No 1, January 1986.

" [Mihelčić84]" M. Mihelčić, K. Wingerath and C. Pirron, *Three-dimensional Simulations of the Czochralski Bulk Flow*, Journal of Crystal Growth 69 (1984), pp. 473-488.

" [Müller93]" G. Müller, *Numerical Simulation of Crystal Growth Process*, Symposium Technisch-Wissenschaftliches Hochleistungsrechnen, München, Juli, 1993.

" [Männikkö94] T. Männikkö, P. Neittaanmäki, D. Tiba, *A Rapid Method for the Identification of the Free Boundary in Two-Phase Stefan Problems*, IMA Journal of Numerical Analysis, Vol. 14, 1994, pp. 411-420.

" [Pironneau82]" O. Pironneau, *On the Transport-Diffusion Algorithm and Its Applications to the Navier-Stokes Equations*, Numer. Math. 38 (1982), pp. 309-332.

" [Pironneau89]" O. Pironneau, *Finite Element Methods for Fluids*, John Wiley & Sons, Masson, Paris 1989.

" [Rama85]" P.A. Ramachandran, M.P. Duduković, *Simulation od Temperature Distribution in Crystals Grown by Czochralski Method*, Journal of Crystal Growth 71 (1985), pp. 399-408.

" [Sackinger89]" P.A. Sackinger, R.A. Brown, *A Finite Element Method for Analysis of Fluid Flow, Heat Transfer and Free Interfaces in Czochralski Growth*, International Journal for Numerical Methods in Fluids, Vol. 9, pp. 453-492 (1989).

" [Seifert96]" W. Seifert, *Numerische Simulation von Kristallzuchtverfahren*, Ph.D. Thesis, to be published in 1996, Fakultät für Mathematik der Technischen Universität München.

" [Sparrow78]" E.M. Sparrow, R.D. Cess, *Radiation Heat Transfer*, Hemisphere Publishing Company, 1978.

" [Temam84]" R. Temam, *Navier-Stokes Equations*, Elsevier Science Publisher B.V., 1984.

faces, Preprint 172, University of Jyväskylä, Department of Mathematics, Septemper 1994.

" [Tiihonen96]" T. Tiihonen, *Stefan Problem with Non-local Radiation Condition*, to be published.

" [Verdi94]" C. Verdi, *Numerical Aspects of Parabolic Free Boundary and Hysteresis Problems*, Numerical Methods for Free Boundary Problems (CIME), Editor A. Visintin, Springer 1994.

" [Voller87]" V.R. Voller, *An Enthalpy Method for Convection/Diffusion Phase Change*, International Journal for Numerical Methods in Engineering, Vol. 24, pp. 271-284 (1987).

" [Watanabe93]" M. Watanabe, M. Eguchi, K. Kakimoto, T. Hibiya, *Double-beam X-ray Radiography System for Three-dimensional Flow Visualization of Molten Silicon Convection*, Journal of Crystal Growth 133 (1993), pp. 23-28.

" [White82]" R.E. White, *An Enthalpy Formulation of the Stefan Problem*, SIAM J. Numer. Anal. Vol.19, No. 6, December 1982.

" [Yi94]" K-W. Yi, K. Kakimoto, M. Eguchi, M. Watanabe, T. Shyo, T. Hibiya, *Spoke Patterns on Molten Silicon in Czochralski System*, Journal of Crystal Growth 144 (1994), pp. 20-28.

" [Yi95]" K-W. Yi, V.B. Booker, M. Eguchi, T. Shyo, K. Kakimoto, *Structure of Temperature and Velocity Fields in the Si Melt of a Czochralski Crystal Growth System*, Journal of Crystal Growth 156 (1995), pp. 383-392.

" [Zienkiewicz89]" O.C. Zienkiewicz, R.L. Taylor, *The Finite Element Method*, Fourth Edition, Vol. 1, 1989, McGraw-Hill Book Company (UK) Limited.

" [Zulehner82]" W. Zulehner, D. Huber, *Czochralski-Grown Silicon*, Crystals, vol. 8, pp. 1-144, Springer-Verlag, 1982.